FINITE ELEMENT ANALYSIS OF COMPOSITE SHEET PILES SUBJECTED TO UNIFORM LOAD AND HARSH ENVIRONMENTS

By

Darchis Fabien

October 2005

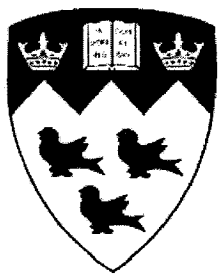

Department of Civil Engineering and Applied Mechanics
McGill University
Montreal, Canada

A thesis submitted to the Faculty of Graduate and Postdoctoral Studies in partial fulfillment of the requirements for the degree of Master of Engineering

Your file Votre référence
ISBN: 978-0-494-24951-2
Our file Notre référence
ISBN: 978-0-494-24951-2

Abstract

Glass Fibre Reinforced Plastic (GFRP) composite structures are increasingly used in waterfront and marine environments due to their corrosion resistance. While the GFRP materials have demonstrated excellent tensile capacities, they also present quite low elastic moduli compared to steel. Consequently, local buckling and excessive deflection are always performance-limiting factors in design of thin-walled composite structures that use low-tech FRP.

The research reported herein is focused on the buckling and deformation analysis of a pultruded sheet pile wall subjected to uniformly distributed load and harsh environmental exposures. Prior to structural analysis, material properties of the composite sheet pile were determined by coupon tests. A finite element ABAQUS model was introduced and validated by comparison with full-scale experimental test data. The prebuckling, buckling and postbuckling behaviour were evaluated and the failure mode identified. In order to enhance the load bearing capacity and reduce the deflection of the sheet pile panel, new profiles were proposed: the purpose was to increase the local buckling load and enhance the stiffness. Adding stiffeners at the junctions between the different section plates appeared to be efficient.

In order to study the durability of the FRP sheet piles under different service conditions, the effects of five environmental exposures on the structural performances were studied: they were freezing, freezing/thawing, wet environment, wet and freezing and wet and freezing/thawing conditions. The elastic moduli were found to be unaffected whereas reductions in the strength were observed. As a result, there was no noticeable change in the buckling load and deflection but significant decrease in ultimate failure load. Maximum loss in load capacity due to moisture uptake and freeze/thaw cycles was found to be about 23%.

Résumé

Les matériaux en GFRP sont de plus en plus utilisés pour des applications en bord de mer grâce à leur résistance à la corrosion. Malgré des capacités de chargement en tension extrêmement élevées, ces composites possèdent des modules élastiques assez faibles si l'on compare à l'acier. Par conséquent, souvent constitués de fines parois, ces composants structuraux flambent très facilement et se déforment de façon importante.

Ce travail comprend l'étude du flambage et de la déformation d'un système de palplanches soumis à une pression uniformément distribuée et exposé à des environnements sévères. Avant tout calcul, les constantes de matériaux ont été calculées à l'aide de tests de coupons. Un modèle Abaqus aux éléments finis a été développé et validé par comparaison systématique avec les données expérimentales. Ce modèle a permis de calculer les comportements de pré flambage, de flambage et de post flambage et la charge de rupture a été déterminée avec succès. Afin d'améliorer la capacité de chargement et de réduire la flèche de la palplanche, des profiles améliorés ont été présentés, le but étant d'augmenter le chargement de flambage et de réduire la déformation non linéaire de la section menant à une déflection importante. L'introduction de renforts rigidifiants aux jonctions entre les plaques de la section a été prouvée très efficace.

Afin de calculer la longévité de la palplanche, les effets de cinq environnements sur le comportement des palplanches ont été étudiés: environnement sec ou saturé en eau, associés avec température ambiante, température de -20°C ou enfin cycle de gel et dégel. Les modules élastiques ont été inchangés et les capacités de chargement largement réduites. En conséquence, il n'y a eu aucun changement des chargements en flambage et des déflections de la palplanche mais une diminution importante de la capacité de chargement. Dans le cas de l'environnement humide subissant des périodes de gel et dégel, la réduction de la capacité maximale initiale a été chiffrée à 23%.

Acknowledgements

I wish to express sincere appreciation to my research advisor Professor Yixin Shao of the Department of Civil Engineering and Applied Mechanics, McGill University, for his support and assistance throughout the project.

The financial support of IBP Corporation was greatly appreciated.

I owe special thanks to my family back home and Marion Dhellemmes, without whose supports the successful completion of this work would not have been possible.

Table of Contents

List of symbols

11	Longitudinal direction of the panel
22	Transverse direction of the panel
E_{11}	Longitudinal tensile modulus of a composite plate
E_{22}	Transverse tensile modulus of a composite plate
G_{12}	In-plane shear modulus of a composite plate
G_{13}	Shear modulus defining transverse shear behaviour in shells
G_{23}	Shear modulus defining transverse shear behaviour in shells
ν_{12}	In-plane major Poisson's ratio of a composite plate
ν_{21}	In-plane minor Poisson's ratio of a composite plate
T_{11}	Tensile ultimate strength in longitudinal direction of a composite plate
T_{22}	Tensile ultimate strength in transverse direction of a composite plate
C_{11}	Compressive ultimate strength in longitudinal direction of a composite plate
C_{22}	Compressive ultimate strength in transverse direction of a composite plate
S	Shear ultimate strength of a composite plate
σ_{11}	Normal stress in the longitudinal direction
σ_{22}	Normal stress in the transverse direction
σ_{12}	Shear stress

List of Figures

Chapter 1 - Introduction

Chapter 2 – Literature review

Chapter 3 – Mechanical properties of pultruded FRP sheet pile composites

Chapter 4 – Numerical model

List of Tables

Chapter 9 – Modification of sheet pile profile design

Chapter 1: Introduction

1.1 Sheet pile walls in waterfront environment.

To protect coastal land from erosion, sheet pilings are commonly used to achieve the serviceability requirements at waterfront as retaining structures. Composed of long vertical interlocking panels as seen on Figure 1.1, the sheet pile walls are designed to resist the earth pressure, the hydraulic pressure, the surface charge and the harsh environmental loads, such as exposure to freeze-thaw cycles, water penetration, and chlorides attacks.

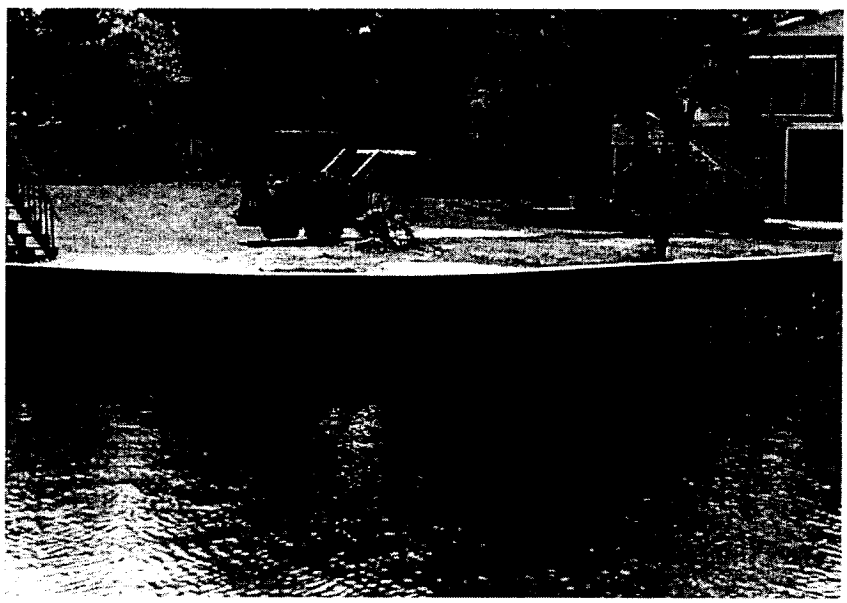

Figure 1.1 Composite sheet pile wall (Source: IBP Corporation, 2000)

Throughout civil work history, sheet pile walls have been constructed out of several materials. Wood quickly shows its durability limits in water because of rotting and of destructive marine micro organisms (molluscan or crustacean bores). Reinforced concrete is not a better solution, for durability of concrete in water is influenced by chloride and sulphate attack, corrosion of steel bars, and freeze and thaw cycles. Steel sheet piles would perfectly suit to the mechanical loads, but would not last long in the very corrosive environment. Many solutions exist to increase the durability life of those traditional

materials: pressure treatment or paint for wood, zinc coating for steel. However, they were all proven to be potentially harmful for the environment. In the US, deterioration of material in marine zones costs $1 billion dollars annually for repair and renovation. The need for a new material adapted to these harsh conditions is demonstrated.

As a solution to the problems mentioned above, the current tendency is to use fibre-reinforced polymer (FRP) composite materials, which have shown advantages of having high strength to weigh ratio (especially in the fibre direction) and being resistant to corrosion and non-toxic to the environment. In other words, this material has the potential to save millions of dollars. The use of FRP is increasing in the construction industry for applications of bridge decks and girders, residential decks and sheet piles.

1.2 Composite sheet piles from IBP Corporation

The composite sheet pile panels studied in this research project were designed and pultruded by IBP Corporation (Niksu, Alberta). The panel is formed as an open section as shown in Figure 1.2, typically 12.6 cm deep and 41.7 cm wide. Two inclined webs join the flanges of the section. The thickness of the plates varies from 4.7mm to 3.2mm. The different panels are joined by a ball in socket connection leaving a free longitudinal rotation.

The variety of the available types of fibres provides numerous design possibilities. Fibres come in several forms among which are roving and mats. Roving is a one dimensional reinforcement composed of glass fibres all aligned in the longitudinal direction. Mats are two-dimension reinforcements formed of randomly orientated or chopped glass fibre filaments. Mats provide most of the shear strength of a composite plate.

The combinations of mats and roving can serve purposes. The flanges of the section studied herein are mainly composed of roving orientated in the longitudinal direction in order to maximize the flexural rigidity of the section. Two small layers of transverse fibers strengthen the shape in the other direction. A chopped strand mat (CSM) is used as

a surrounding surface layer. In order to enhance the shear rigidity of the panel, a continuous filament mat (CFM) is added in the web. The same CFM layer constitutes the inside of the eye connection to reduce the transverse opening of the eye connection. The details of the layer structure of the composite sheet pile are given by Giroux (2000).

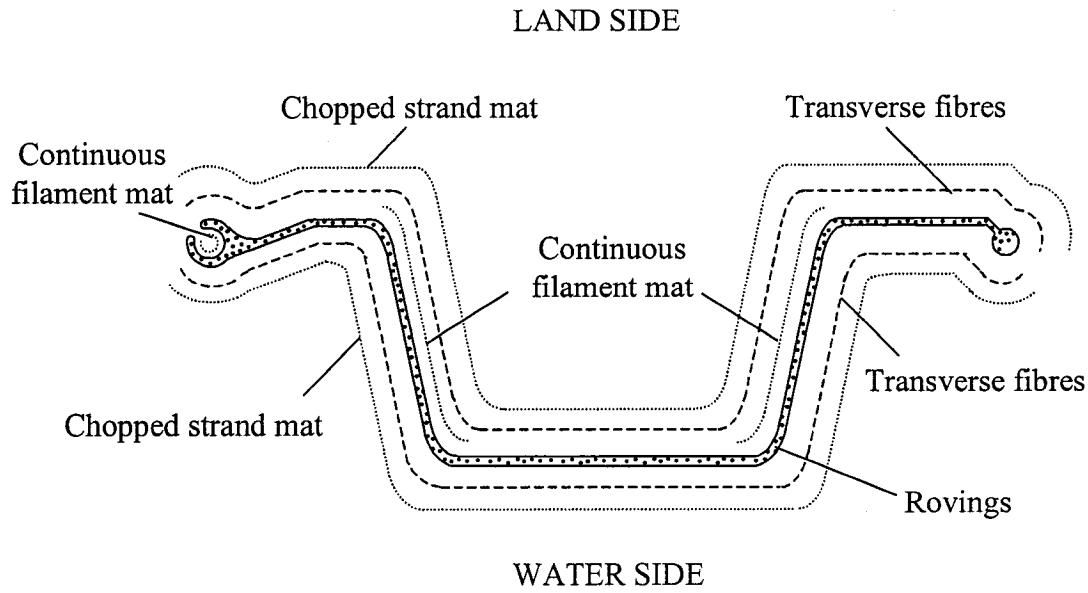

Figure 1.2 Exploded view of the composite sheet pile panel profile

In Figure 1.2, the section is oriented with a "land side" and a "water side". The interlocking connection is placed on the compressive flange (Land side). However, in the field, same sheet piles can be installed with interlocking connection on tension side. The two orientations are shown in Figure 1.3, with one referred to standard position and the other to reverse position.

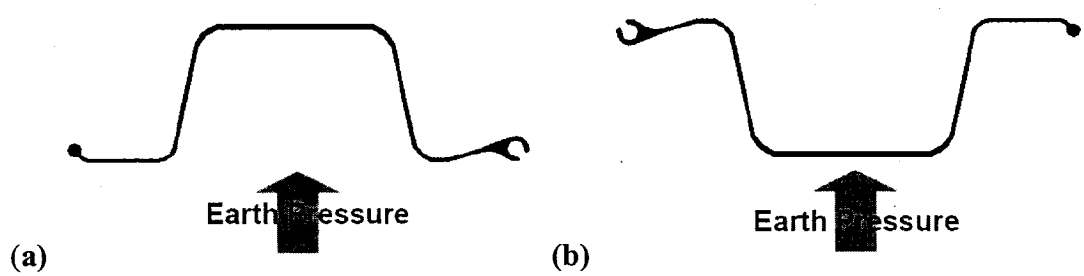

Figure 1.3 Load configurations – (a): standard position, (b): reverse position

1.3 The challenge of using composites in civil structures.

Before the construction industry will accept this new material for general application, the load-carrying capacity and long term performance of FRP composite products in civil engineering structures must be demonstrated.

Material tests show that pultruded fibre-reinforced polymer composite materials have high strength characteristics but very low elastic modulus, usually between 25GPa and 40GPa in the longitudinal direction. For this reason, FRP thin-walled structure design usually leads to either local buckling or excessive deflection.

To estimate the deflection of FRP composite structural shapes, Timoshenko's deflection equation is often used in preliminary design. The flexural and shear rigidities of the shapes can be determined experimentally using multi-span test method (Giroux, 2000). However, problems arise when geometric non-linear deformation occurs; because of the weak material property in transverse direction of FRP structural shapes, such non-linear deformation can become critical. Currently, no simple theory exists to provide an explicit design equation for deflection control. When non-linear deflection due to stiffness change is expected, finite element analysis seems to be the efficient tool for failure and deformation prediction.

To estimate the load bearing capacity of thin-walled structures, analytical tools are needed. Currently, buckling of a section is reduced to a simpler problem: buckling is simulated by a single compressive plate with assumed boundary conditions. This approach requires knowledge of the restraints of that compressive plate with its surrounding plates and of the equation governing the relation between axial stresses in compressive plates and external loads on the structure. Two problems arise from this current approach. First, it is difficult to simulate with accuracy the boundary conditions for connected flanges and webs in a complete structural shape. Second, the analytical calculation does not take into account non-linear geometric deformation of the section which is often not negligible in composite structures, and which results in an inaccurate

calculation of the axial stress in the section. Consequently, in many cases, this analytical approach provides non satisfactory buckling prediction results. A finite element analysis approach appears promising in performance analysis. It is indeed possible with FEA tools to calculate directly buckling loads without having to consider boundary conditions between the different plates, and it permits to take into account geometric non-linear deformation.

FEA tools are also promising for investigating the long term performance of FRP composite products. Durability performance of sheet piles can be simulated using reduced material properties to assess the effect of environmental exposure. It is difficult to perform full-scale panel tests to examine the direct effects of freezing, freezing/thawing and water saturation on a pultruded sheet pile. Numerical simulation provided a means to complete the analysis and estimate the reduction in capacity due to exposure.

1.4 Research objectives

This research was directed towards the study of the load-carrying capacity and long-term performance of a pultruded sheet pile panel using the finite element code ABAQUS/STANDARD. Three main objectives were targeted:

(1) To evaluate the structural behaviour of the sheet pile panel, including the pre-buckling, buckling initiation and post-buckling performances in both standard and reverse installations.

(2) To assess the effects of the environmental exposures on the load-carrying capacity and deflection of the sheet pile. The environmental exposures comprise of continuous freezing, freezing/thawing cycles and moisture uptake.

(3) To propose design modifications to increase the load bearing capacity and serviceability performance of the panel.

An AutoCAD drawing of the section provided by the manufacturer was used as geometric input of the original design. Material tests were conducted to determine the strength and

the modulus of each member of the section in transverse, longitudinal and 45° directions. The results are presented in Chapter 3.

In order to be able to evaluate the effect of environmental conditions on the sheet pile profile, degradation tests of coupons were also performed (Section 3.2). Contrary to the previous work on the durability of the composite sheet pile (Kouadio, 2002), only ambient temperature was used for water absorption tests. The accelerated saturation at high temperature seemed to introduce additional damage to the matrix which might not exist when the sheet piles serve in the field. Effects of continuous freezing and freeze-thaw cycling on the saturated samples were studied. Since composite sheet pile panel failed due to buckling, transverse properties were seen equally important to that in longitudinal direction. Consequently, the durability tests were done to assess the effect of environmental exposure on mechanical properties in longitudinal and transverse directions.

A complete FEM model was developed (Chapter 4) to simulate the two installation configurations with the finite element program (Chapter 6 and 7). In a first step, the numerical pre-buckling data were compared to the experimental results from previous full scale tests in order to validate the numerical model and the numerical algorithm used. Post-buckling calculations, involving the introduction of geometric imperfections in the panel and introduction of dynamic loading rates, were performed to investigate the post-buckling failure mechanisms of the standard position and reverse position panels.

By introducing the reduced mechanical properties in the numerical input file, environmental expose effects on the buckling and failure loads of pultruded sheet piles were examined. The results are presented in Chapter 8. Finally, modifications of the sheet pile design were proposed to enhance the buckling resistance and deflection resistance (Chapter 9).

Chapter 2: Literature Review

2.1 FRP materials and structural shapes

2.1.1 Material properties of FRP composite

Because of the increasing interest in fibre reinforced polymer composites, research on mechanical properties of FRP material is extensive. A complete set of standards was developed in the annual books of ASTM Standards in order to respond to the high demand for determining and comparing composite properties. The following literature review will be restricted to low-cost composite for use in infrastructure application.

Stress-strain curves of thick FRP composite (6.35mm and 12.7mm) constituted of a combination of unidirectional E-glass roving and CFM layers in a vinylester matrix were investigated by Haj-Ali and Kili (2002). Six different off-axis coupon tests (0, 15, 30, 45, 60 and 90°) were accomplished in tension and compression to obtain the linear and non-linear responses of the FRP coupons. It was reported that the nonlinear behaviour was relatively negligible for the 0° and 15° coupons, and more significant for the four other angles in both tension and compression. The two authors developed a 3D micromechanic model with success to predict off-axis linear and non-linear responses: in this model, the E-glass fibre remained elastic and the non linear behaviour was attributed to the matrix.

However, in the majority of research works, it is common to use the assumption that the composite remains elastic up to failure. Most of the work on structural behaviour of beam sections involved coupon testing prior to any stiffness calculations of the profiles in order to determine with precision the properties of the composite. Wang and Zureick (1994) tested several coupons sawed from different location of a pultruded I-beam in order to obtain its tensile properties. Brooks and Turvey (1995) decided to carry out stress-strain

tests of the composite coupons of pultruded I-beam in order to adequately predict the lateral buckling response.

Because of the different applications, FRP composites may vary substantially in material compositions, design layouts, and mechanical properties. Coupon tests seems compulsory prior to any structural behaviour calculation. Bank reported (1995) that one of the difficulties of local buckling prediction arises from the fact that material data are never known with precision: the manufacturer data are generally very conservative. Moreover, the composite is usually inhomogeneous due to fabrication process. Large deviation can be expected throughout a unique composite. Bank insisted on the fact that the "actual" material properties are needed in order to predict with success the buckling behaviour of a pultruded section.

2.1.2 Durability of FRP composite in harsh environment.

Recently, most of the research on FRP durability deals with composite reinforcements for concrete structures. FRP reinforcing bars are being considered as replacements for steel reinforcements in concrete structures. Tests were conducted by Micelli and Nanni (2004) on FRP rods for concrete structures damaged by several aggressive environments such as hot water, cold water, thermal cycling and alkali agents. SEM images showed that most of the strength loss came from damages in the matrix and at fibre/matrix interface due to fluid diffusion. Karbhari (2002) studied carbon/vinlyster FRP composite used for external reinforcement of concrete cylinders. The author tested conditioned concrete cylinders strengthened with composite sheets. The effect of unexposed freeze, saturated freeze and saturated freeze/thaw cycles were examined on the tensile modulus and strength in the direction of the fibres. The results showed no change of the elastic modulus but significant reduction in the strength. A decrease of 40% of the strength was monitored for the worst environment, i.e. immersion and freeze/thaw cycles.

Because thin-walled FRP structures are often used directly in contact of aggressive environment such as in waterfront sheet pile wall applications, it was seen imperative to carry out independent study on FRP composite used in such structures. Gellert and Turley

(1999) studied four different glass-fibre composites. The composites were formed of alternative layers of woven roving and chopped strand mat; different kinds of matrix material were used: Polyester, Phenolic and Vinylester. The samples were aged in seawater at ambient temperature (30°C) during 810 days. For the polyester laminate, 17% reduction in strength and 6% decrease in the modulus were reported. These values could be related to FRP sheet pile studied herein for the composite is constituted by the same matrix. Creep was also reported to be higher in immerged conditions than in atmospheric conditions. The writers observed that Phenolic composites experienced higher degradation due to higher water uptake. It was assumed that damage resulted from fibre/matrix debonding and matrix cracking.

Shao and Kouadio (2002) studied the durability of the sheet pile panel composite (same panel used throughout this thesis). Samples were cut in the longitudinal direction in the web and main flange of the section. Water absorption tests were conducted at high temperature (70°C) and ambient temperature (23°C) during 260 days: the high temperature of 70 °C was used to accelerate saturation whereas the ambient temperature was used to simulate the service conditions. It was found that the elastic moduli of the composites (web and main flange) were maintained after hot water immersion. Nevertheless, high reduction of the longitudinal strength was observed for the high temperature immersion: it was 60% decrease in comparison to dry reference material. For ambient immersion, at 260 days, the strength reduction was only 17%. The high temperature immersion had accelerated the saturation, but at the same time, it could also introduce additional damage which might not be existent when composites are used at ambient temperature. To study long term performance of composites in water, it was seen better not to use high temperature to accelerate the tests. The saturated composites had shown excellent resistance to freeze/thaw cycles.

2.1.3 Buckling behaviour of FRP structures and critical load prediction.

Structural behaviours of composite structures can be predicted with success. Two major tools are used to make the prediction of local and global buckling of pultruded structures:

analytical tools based mainly on variational energy method and numerical tools such as finite element analysis.

Qiao and Shan (2004, a) used the energy method to analyze the flexural-torsional buckling of pultruded open channel beams. The second derivative of the strain energy was calculated and solved employing the Rayleigh-Ritz method. Finite element calculations were also completed using ANSYS. The experimental, analytical and numerical were compared with success. The same authors, Qiao and Shan (2004, b) developed local buckling equations in order to help design for several FRP profiles: Box, I-, C-, T-, Z- and L- sections. Explicit solutions for buckling of elastically retrained orthotropic plates were developed with the variational method. The second step was to determinate the rotational restraint stiffness of the junctions of the profiles. By joining both equations (buckling of individual plates and restraints coefficients of a particular section), the authors were able to develop a table of explicit critical local buckling stress of the different FRP shapes considered. In order to verify the results, the buckling of the restrained orthotropic plate was numerically calculated; the difference between numerical and analytical was always less than 1%. The buckling loads of the six FRP profiles (Box, I-, C-, T-, Z- and L- profiles) under compressive force were also calculated with ANSYS. The numerical buckling loads calculated were always within 5% of the analytical prediction.

Finite element programs are not always used as a verification tools. FEM are often used as design tools to directly predict buckling loads and to avoid long fastidious calculation. Brooks and Turvey (1995) studied the lateral buckling of pultruded GRP I-section cantilevers with the ABAQUS program using four node shell elements. The buckling load numerically obtained was found lower than the experimental value. It was suggested that introducing the non-linear deformation of the section in the buckling calculation would improve considerably the numerical prediction (more details in Chapter 5).

Bank and Yin (2000) predicted the buckling and post-buckling behaviours of a pultruded I-beam in four point bending by using a modified version of NIKE3D. The post-buckling

behaviour of the beam was obtained by introducing imperfection in the initial geometry in order to trigger the post-buckling shape (more details in Chapter 5). The experimentally observed flange and web separation was simulated by a node pair formulation added in the program by the authors. The Chang and Chang failure criteria was chosen as a separation trigger. With the help of this subroutine, the entire progressive failure load-displacement curve was obtained. The experimental and numerical failures were compared with success. It was found that the general failure load of the beam was identical to the local failure load of the web-flange junction: once the first node separation occurred, no further loading was possible.

The main criticism made by the scientific community on finite element program research is that it can not generate explicit design formulae as with the analytical approach. Models have to be run case by case. However, it was shown that design equations can be developed with the help of wide parametric studies and curve fitting using FEA. Barbero and DeVivo (1999) were able to develop design equations for pultruded I-beam in beam-column loading configuration failing due to local buckling of the flange. The I-beam was modelled with ABAQUS using quadratic thick shell element (S8R). A numerical parametric study on the compressive force eccentricity and on the initial imperfection of the beam was undertaken and explicit formulae of resistance factors were developed to take into account such imperfections in the design equations.

Pecce and Cosenza (2000) analyzed local buckling in FRP I-beams with the finite element code LUSAS. A wide parametric study on the dimensions and material properties of the section was aimed at developing an explicit formulation of the critical buckling stress in the flange, taking into account the web restraints.

ABAQUS/STANDARD provides its users a complete set of calculation options which permit calculation of the pre-buckling, buckling, post-buckling and failure of composite thin-walled shapes. Chapter 5 reviews all of the theory of numerical algorithms proposed in the Abaqus documentation, which were used in this research to analyze the local buckling of composite sheet piles subjected to uniformly distributed load.

2.2 Previous study of composite sheet piles at McGill University

2.2.1 Three-point and four-point bending tests of the sheet pile panel

In order to calculate the flexural and shear stiffness of the pultruded sheet pile panels, Giroux (2000) tested the profile with different spans under three and four-point bending tests using a single panel with standard installation (Figure 2.1. The flexural and shear rigidities were then calculated using Timoshenko's equation.

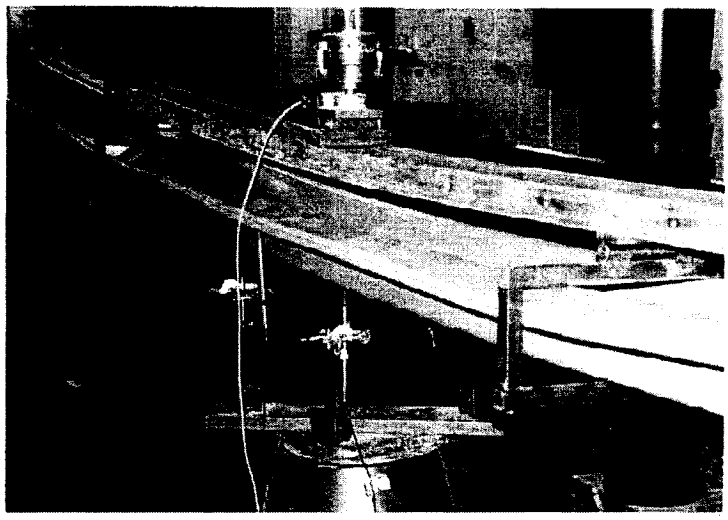

Fig 2.1: Layout of the four point bending tests on the FRP panel, Giroux (2000)

Failure tests were also performed by Giroux (2000) using the same three and four-point bending tests in an attempt to obtain the maximum moment that could be carried by the sheet piles. Because of local crushing of composites at load points and excessive deflection generated in such a large span, no conclusions were made for the moment carrying capacity. In order to assess the load-carrying capacity of sheet pile subjected to earth pressure, a uniform pressure test setup was developed by Shanmugan (2004).

2.2.2 Full scale testing of the FRP panel under uniformly distributed load

The FRP panels are installed in the field in two different positions, either in standard position or reverse position. Both configurations were tested in McGill Civil Engineering

Material Lab under simulated service loading by a uniformly distributed transverse load. This section is to present a brief review of the experimental work done by Shanmugan (2004). In this research, the finite element analysis was used to simulate those experiments and the numerical results were compared with the experimental data.

Standard position

In order to study the influence of the connection between panels, both single panels (B1, B2, B3 and B4) and connected panels (C1, C2, C3 and C4) were tested. The panels were placed in a steel frame. Pin and roller boundary conditions were applied by concrete blocks and steel bars. The tests setup is shown in Figure 2.2.

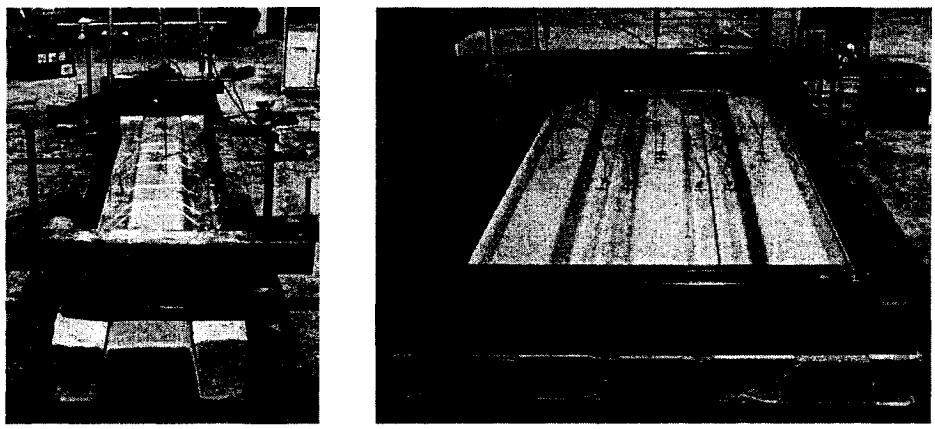

(a) Single panel test (b) Connected three-panel test

Fig 2.2: Uniform pressure tests of sheet piles in standard position

The loading was evenly distributed along the section by a pressure supplied by an airbag. Strain gauges and LVDT sensors were placed at mid span sections in order to monitor the deformation of the panels. It was reported that the connected and single panels behaved in a same way. The load-deflection curves and load-strain curves obtained and the final failure modes were very similar in both configuration. Figure 2.3 compares the two failure modes. The ultimate failure pressures for the eight panel tests are summarized in Table 2.1.

It was found that single panel exhibited 15% higher load capacity than connected panels. The difference between the two configurations was attributed to the friction between the

panel and the steel frame, which had more influence on the single panel configuration than on the connected panel.

Table 2.1: Experimental failure loads of the panels in standard position

Single Panel	Failure pressure
B1	48 kPa
B2	49 kPa
B3	42 kPa
B4	43 kPa

Connected Panel	Failure pressure
C1	42 kPa
C2	43 kPa
C3	36 kPa
C4	35 kPa

No buckling initiation was seen (waves on the compressive flanges) nor recorded via the strain locations prior to final failure. Buckling initiation and global failure of the sheet pile occurred almost simultaneously. A very complicated combination of composite delaminating and matrix failure was found at the junction between the web and the bottom flange (Figure 2.3).

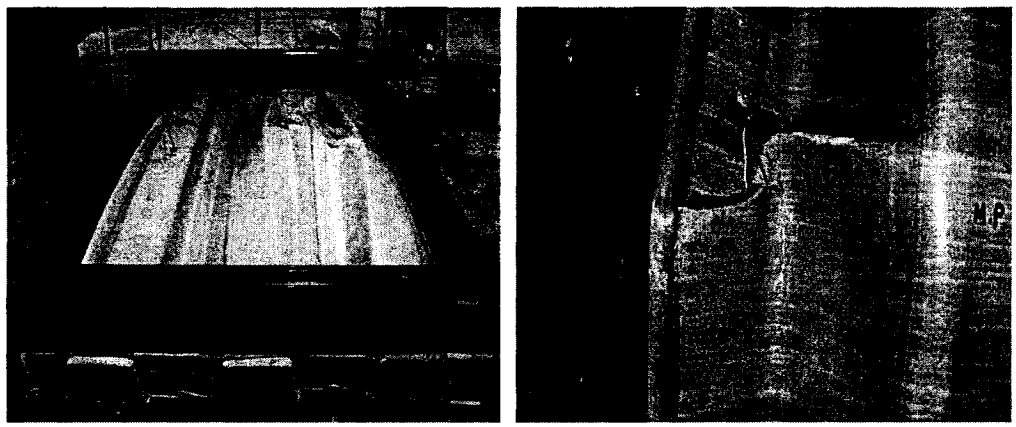

Fig 2.3: Experimental failure modes of the standard single and connected sheet piles

Reverse position

The test setup for the reverse position panel is shown in Figure 2.4. The results of the sheet pile in the reverse configuration were completely different to those in the standard configuration. Buckling of the compressive main flange occurred at a low pressure and

was observed by a sudden change of slope of the strain reading at center of the compressive flange. The reverse position panel exhibited a post buckling behaviour and ultimate failure occurred much later. Two different inverted panels were tested and their results are summarized in Table 2.2.

Table 2.2: Experimental buckling and failure loads of the reverse panels

Panel name	Buckling initiation	Final failure
R1	23 kPa	44 kPa
R2	27 kPa	48 kPa

The failure mode consisted of tensile tearing at both web-main flange junctions. Cracks were monitored in the webs and in the main flange along the compressive junctions at mid-span. The failure mode is shown in Figure 2.4.

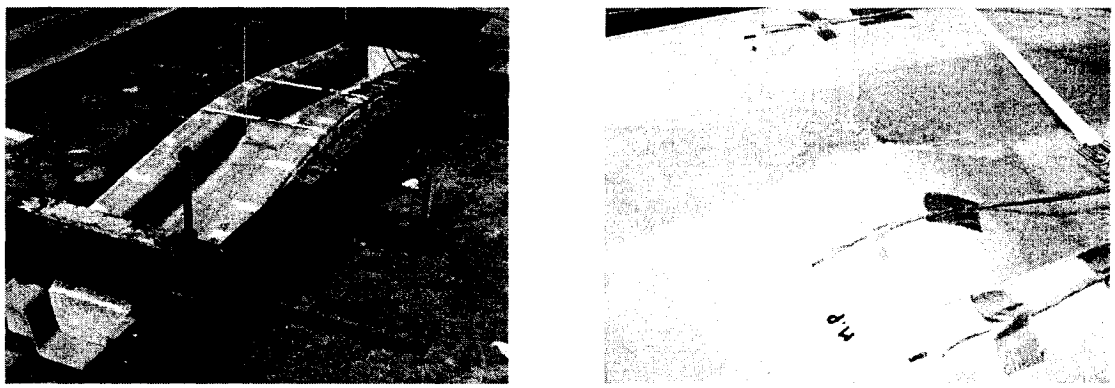

(a) Experimental setup (b) Buckling failure

Fig 2.4: Experimental setup and buckling failure of the reverse position sheet pile

In order to have a more precise understanding of the deformation, buckling and failure mechanisms of the reverse and standard position panels under service loading, the structural behaviour of the sheet pile panel was studied using a FEM program. Experimental data obtained by Shanmugan were used for comparison with the numerical calculations. In order to develop a precise model, mechanical properties of a pultruded FRP composite in longitudinal and transverse directions were investigated. This work will be explained in the next chapter.

Chapter 3: Mechanical Properties of Pultruded FRP Sheet Piles

3.1 Material properties of the dry composite

In order to obtain the mechanical properties of sheet pile panels in longitudinal and transverse directions, coupon tests were performed on the web, eye/pin flange and main flange of the FRP sheet pile studied in this project. The respective positions of the three members are shown in Figure 3.1. The detailed layer structure of the sheet pile is given in Table 3.1. Since the three members were composed of different fibre fractions, layer layouts and thicknesses, differences were expected in the values of the material constants.

Table 3.1: Layer structure of the sheet pile

Member	Layer	t_i [mm]	t [mm]	Fibre fraction
Main flange composite	Chopped mat	0.46	4.69	0.58
	Transverse mat	0.32		
	Roving	3.13		
	Transverse mat	0.32		
	Chopped mat	0.46		
Pin/Eye flange composite	Chopped mat	0.43	3.18	0.34
	Transverse mat	0.34		
	Roving	1.64		
	Transverse mat	0.34		
	Chopped mat	0.43		
Web composite	Chopped mat	0.33	3.18	0.37
	Transverse mat	0.34		
	Roving	0.84		
	Continuous filament mat	0.99		
	Transverse mat	0.34		
	Chopped mat	0.33		

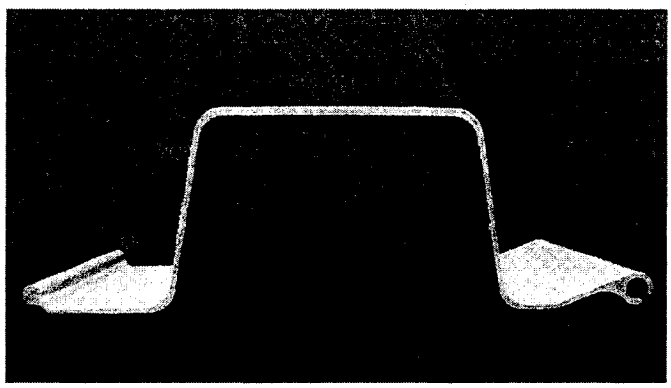

Figure 3.1: Section profile and nomenclature of the sheet pile

For the complete description of a 2D elastic orthotropic laminate, thirteen constants are needed:

- E_{11}: Young's modulus in longitudinal direction in tension and compression
- E_{22}: Young's modulus in transverse direction in tension and compression
- υ_{12}: Poisson ratio
- G_{12} (in plane shear modulus), G_{13} and G_{23} (transverse shear moduli)
- T_{11} and C_{11}: tensile and compressive ultimate strength in longitudinal direction
- T_{22} and C_{22}: tensile and compressive ultimate strength in transverse direction
- S_{12}: ultimate shear stress.

Because testing for G_{13} and G_{23} is very complicated, it is assumed that these latter are equal to G_{12}. This assumption was used by Bank (2000) in FE analysis of pultruded structural shapes.

3.1.1 Testing procedures

Tensile off-axis stress-strain responses were obtained following ASTM D 3518M for shear modulus and strength and ASTM D 3039 for longitudinal and transverse moduli and strengths. For each laminate member in each direction, at least three coupons were tested. If the results were scattered (variability over 10%), more tests were repeated. Compressive stress-strain curves were difficult to obtain due to the very small thickness of the FRP laminate plates; they were 4.69 mm for the main flange and 3.18 mm for the web and pin/eye flange. Following ASTM D695 standard for compressive stress-strain

curve, coupons should have the dimension of 4.69x12x15mm for main flange, 3.18x12x15mm for eye/pin flanges and 3.17x12x15mm for web. The small sized specimens made the placement of strain gauges impossible. Compressive modulus was obtained by using longer coupons tested within linear elastic limit. Compression tests were carried out for ultimate compressive stresses based on ASTM D695. When using free end conditions, end failure often occurred with scattered results. Clamped end conditions (therefore adding a grip zone) produced more consistent results. For each laminate in each direction, at least three coupons were tested to obtain average composite strength.

3.1.2 Elastic constants of composite sheet pile

Typical tensile stress-strain curves of main flange, eye/pin flange and web coupons tested in longitudinal, transverse and 45° off-axis directions are shown in Figure 3.2. It was observed that tensile stress-strain curves were quite linear in the three directions of loading until final failure. This was particularly true for loading in the longitudinal direction. In transverse and 45° off-axis directions, a small non-linear response was observed due to the increased role of the matrix.

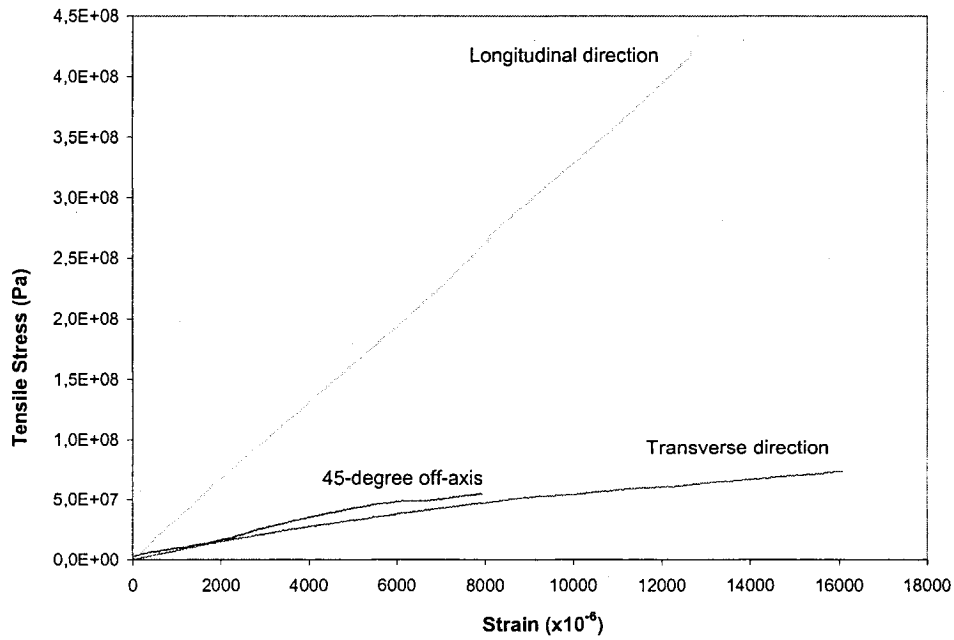

(a) Stress-strain curves for the main flange location

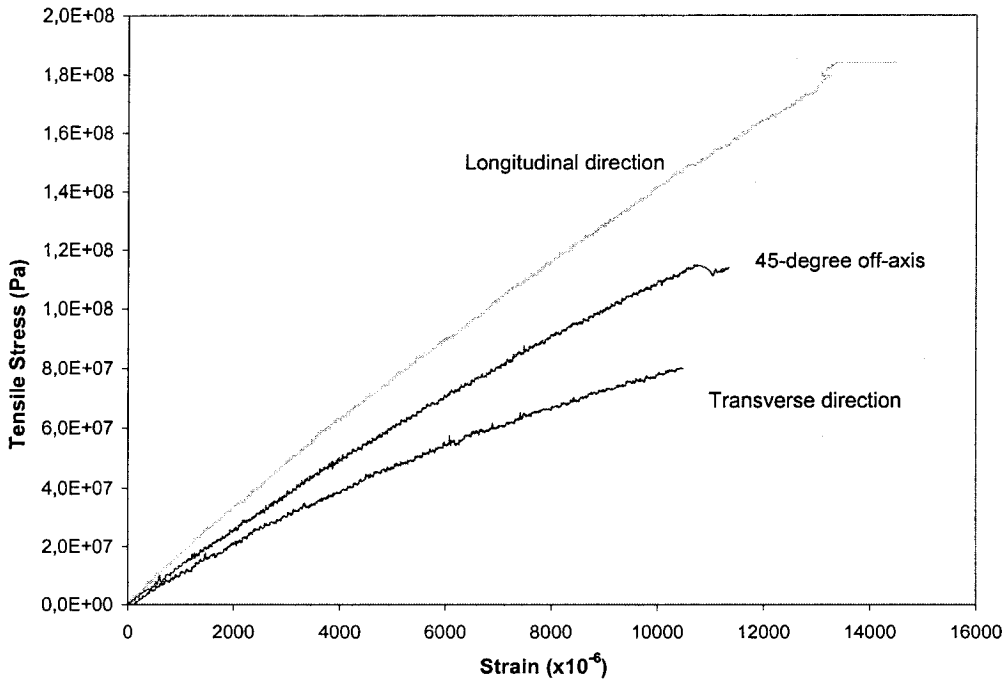

(b) Stress-strain curves for the web location

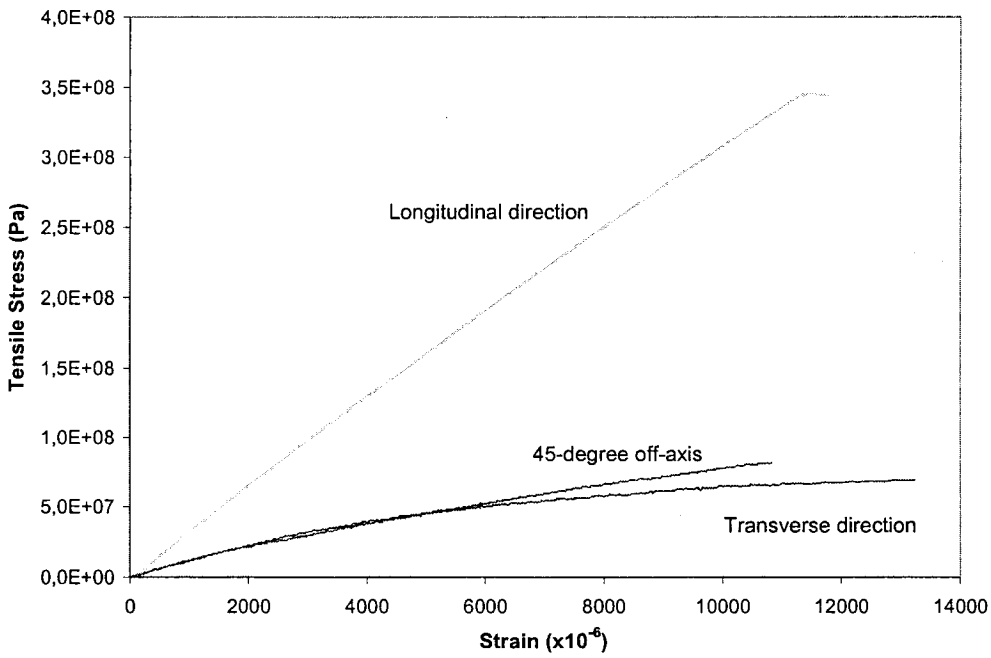

(c) Stress-strain curves for the eye/pin flange location

Fig 3.2: Tensile stress – strain curves for the main flange, web and eye/pin flange composites

The tensile elastic properties of dry composites were calculated from the stress-strain curves and are summarized in Table 3.2. As regard to the compressive elastic properties, due to the large slenderness ratio of the compression coupons, all samples failed from buckling. However, the compressive moduli were calculated from the linear portion of the curves.

Table 3.2: Elastic constants of composites [GPa]

Elastic constant	Main Flange	Web	Pin/Eye flanges
E_{11} tension (GPa)	31.4 ± 5%	16.1 ± 4%	30.2 ± 5%
E_{11} compression (GPa)	27.8 ± 6%	14.5 ± 5%	26.2 ± 5%
E_{22} tension (GPa)	7.28 ± 5%	12.3 ± 3%	7.9 ± 7%
E_{22} compression (GPa)	8.7 ± 7%	13.2 ± 6%	8.2 ± 4%
υ_{12}	0.18	0.20	0.18
G_{12} (GPa)	3.1 ± 6%	2.7 ± 10%	3.0 ± 6%

The composites constituting the main flange and the eye/pin flange had close values of moduli in tension and compression. It seemed that the roving layers played critical role in determining the stiffness constants: they were both very strong in the roving direction and quite weak in the transverse direction. In the web, the thickness of the roving layer was reduced and an additional CFM layer was added (see Table 3.1). Consequently, the laminate appeared to be more uniform: compared to the other two composites, the longitudinal modulus was reduced but the transverse modulus was enhanced. Concerning the 45 degree off axis test, G_{12} was found quite unchanged by the different layer structures.

Small differences were noted between the compressive and tensile moduli. An average of 12% decrease was found in compressive longitudinal moduli in comparison with tensile longitudinal moduli. For the transverse modulus E_{22}, the results were opposite: E_{22} in compression was found larger than E_{22} in tension for the three composites: the differences of the two moduli were 19% for the main flange, 7% for the web and 4% for the eye/pin flange.

3.1.3 Ultimate strength test results.

The ultimate stresses of the three laminate members of the sheet pile are presented in Table 3.3. They were used to determine the failure load based on composite failure criteria in the numerical simulation.

Table 3.3: Ultimate strength of composites [MPa]

Ultimate strength	Main Flange	Web	Pin/Eye Flange
T_{11} [MPa]	422 ± 3%	180 ± 9%	298 ± 10%
C_{11} [MPa]	314 ± 3%	178 ± 5%	250 ± 3%
T_{22} [MPa]	70 ± 4%	119 ± 3%	84 ± 5%
C_{22} [MPa]	79 ± 10%	99 ± 10%	66 ± 9%
S_{12} [MPa]	20 ± 5%	45 ± 5%	32 ± 7%

Whereas the main flange and the eye/pin flange had similar elastic properties, their ultimate stress results were quite different: in the longitudinal direction, the main flange composite was 40% stronger in tension and 25% in compression. The ultimate stresses in the transverse direction of the main flange and pin/eye flange were fairly close. Because of the CFM layer, the web composite was stronger in the transverse direction but weaker in the longitudinal direction than the other two composites. The 45-degree off-axis strength of the web composite was found the highest, suggesting that the use of CFM layer improved shear resistance.

It is important to keep in mind that these ultimate stresses were tested at the middle of each plate. The composite strength at the junctions between the plates remained unknown. In the numerical model, the junctions were assumed to be as strong as the nearby flanges in the longitudinal direction and as strong as the nearby web in the transverse direction. This assumption relied on the fact that the junctions had the same longitudinal roving density as the nearby flange and that the CFM mat of the webs were extended in the junctions (see Figure 1.2).

The typical failure modes of the main flange are displayed in Figure 3.3. According to Figure 3.2, for the tensile coupons, failure occurred at a strain ranging from 1.1% to 1.6% when loaded either in longitudinal or transverse direction. Since the maximum tensile strain was 1.5% in matrix and 4.4% in fibreglass, cracks had initiated first in the matrix and then propagated into fibres, leading to ultimate fracture. Tensile and compressive failures in the longitudinal direction were explosive. In tension, the fibres failed in bundles (Figure 3.3-a), whereas in compression, the fibres failed in kinking, i.e. shear buckling in the roving layer (Figure 3.3-d). In the transverse direction, failure cracks occurred in the matrix due to high elongation of the matrix (Figure 3.3-b). The 45-degree samples failed due to the shear failure of the matrix along the fibres of the roving layer (Figure 3.3-c).

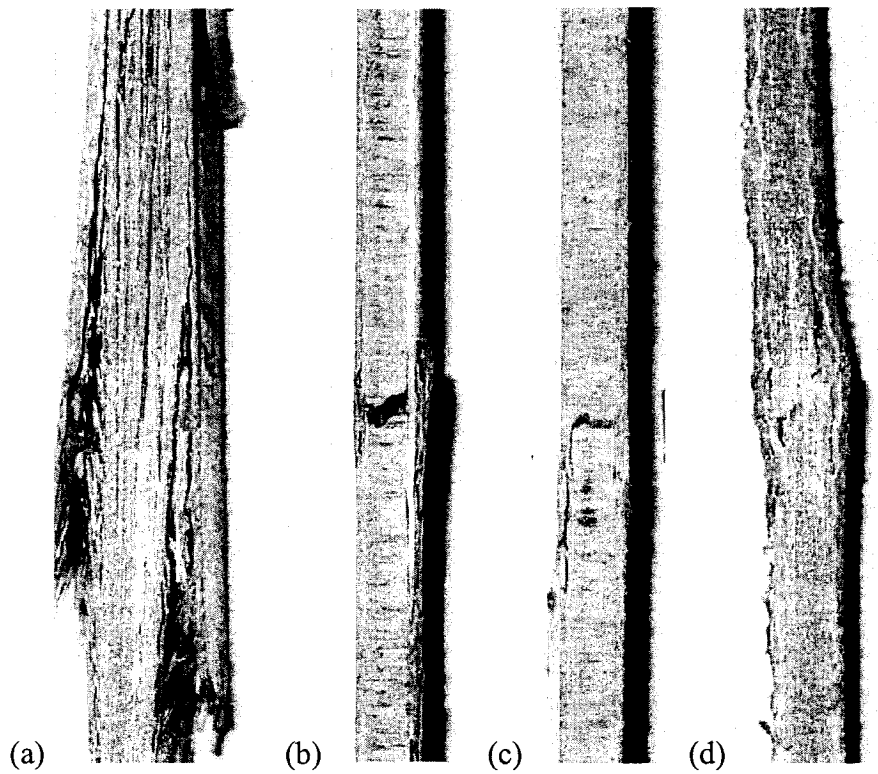

Figure 3.3: Failure modes of the main flange location

(a) Tensile failure in longitudinal direction

(b) Tensile failure in transverse direction

(c) Tensile failure in 45 degree direction

(d) Compressive failure in longitudinal direction

3.2 Effect of cold and moist environmental exposures on material properties.

Coupons were degraded and then tested in order to examine the effects of service environments on the FRP composite material properties. Three environmental exposures were investigated: (1) water immersion, (2) water immersion and freezing conditions (3) water immersion and freeze/thaw cycling conditions. Each group of tests consisted of longitudinal, transverse and 45° coupons for main flange, pin/eye flange and web and for tensile and compressive tests. Dry composites were also tested under freezing and freeze/thaw cycling for comparison. The freeze/thaw cycling of saturated composites were studied to simulate the usual environment of the waterfront sheet pile walls in Canada.

3.2.1 Degradation procedures

Totally six group of composites were tested at different environmental exposures: (1) Dry reference composites tested as-received; (2) Dry composites exposed to 60-day continuous freezing at -24 °C; (3) Dry composites exposed to 250 times freeze-thaw cycling between +5 °C and -18 °C; (4) Saturated composites after two years immersion in tap water at room temperature; (5) Saturated composites exposed to 60-day continuous freezing at -24 °C; (6) Saturated composites exposed to 250 times freeze-thaw cycling between +5 °C and -18 °C.

Water absorption tests were conducted following ASTM D570 in tap water at room temperature of $23^0 \pm 2^0$C for 2 years. Saturation was achieved after 540 days with an average water uptake of 1.54 ± 0.08%. Hot water aging was not employed to assure that the diffusion and relaxation through the water uptake by the composites were not exaggerated by the high temperature. The freeze-thaw cycling of saturated composites was performed using ASTM 666 chamber at a cycling rate of 4.5 hours per cycle and at temperatures between $+5^0$C and -18^0C. Half of the specimens were tested after 50 cycles, and the remaining ones after 250 cycles. The incidence of cracking often occurred during

the first few cycles and then levelled out with continued cycling (Shao and Kouadio, 2002). The other set of saturated composites were placed in a freezer to be exposed to a continuous freezing at $-24^0 \pm 3^0$ C for a period of 60 days. Dry composites were also tested after 250 freeze-thaw cycles and 60-day continuous freezing for comparison. The dry composites were thermal cycled in water between $+5^0$C and -18^0C. All tensile and compressive tests of composites exposed to different service environments were performed at room temperature of 23 ^{0}C. Therefore the low temperature stiffening of composites should not be expected.

Table 3.4 summarizes the complete results of the tests for the five environment conditions along with the reference of dry composites. The variability of the tests is given when more than one coupon was tested. Figs 3.5 – 3.10 compare the six material constants, respectively E_{11} and E_{22} in tension, T_{11}, C_{11}, T_{22} and C_{22}. The labels on the bar charts indicate the percent of retaining property as compared to the dry reference. For saturated samples under freeze/thaw cycling, only the test results after 250 cycles are presented since there were no significant differences between 50 cycles and 250 cycles.

3.2.2 Complete results

Table 3.4: Effects of environmental conditions on composite properties

		Moisture	Dry	Dry	Dry	Saturated	Saturated	Saturated
		Temperature	20°C	-20°C	-20°C/+4°C	20°C	-20°C	-20°C/+4°C
Elastic properties [Gpa]	*MAIN FLANGE*	E11	31.4 ± 5%	29,4	29,4	29.4 ± 6%	29,6	30,5
		E22	7.3 ± 5%	7,7	6,7	7.4 ± 2%	7,4	7,2
		G12	3.1 ± 6%	2,8	2,9	xxx	xxx	xxx
	WEB	E11	16.1 ± 4%	15,0	14,4	15.0 ± 12%	16,1	14,9
		E22	12.3 ± 3%	12,1	12,0	11.5 ± 9%	11,9	12,1
		G12	2.7 ± 10%	2,8	3,0	xxx	xxx	xxx
	EYE/PIN FLANGE	E11	30.2 ± 5%	28,7	27,6	28,7	27,8	27,2
		E22	7.9 ± 7%	7,3	7,3	7,3	8,3	7.4.
		G12	3.0 ± 6%	xxx	3,1	xxx	xxx	xxx
Ultimate stresses [Mpa]	*MAIN FLANGE*	T11	422 ± 3%	402 ± 2%	332 ± 1%	313 ± 6%	323 ± 3%	305 ± 3%
		C11	314 ± 3%	306 ± 8%	280 ± 5%	252 ± 7%	253 ± 1%	251 ± 5%
		T22	70 ± 4%	71 ± 6%	60 ± 1%	60 ± 3%	56 ± 3%	56 ± 1%
		C22	79 ± 10%	75	70	67 ± 10%	66 ± 4%	59 ± 10%
		S	20 ± 5%	21 ± 6%	20 ± 1%	17 ± 5%	xxx	xxx
	WEB	T11	180 ± 9%	167 ± 2%	160 ± 2%	164 ± 12%	154 ± 1%	139 ± 2%
		C11	178.2 ± 5%	195 ± 8%	142 ± 5%	138 ± 10%	136	139 ± 8%
		T22	119 ± 3%	119 ± 7%	115 ± 2%	101 ± 10%	90 ± 3%	85 ± 1%
		C22	99 ± 10%	96 ± 1%	93 ± 4%	86 ± 6%	80 ± 8%	77 ± 10%
		S	45 ± 5%	43.6 ± 2%	40 ± 4%	32 ± 3%	xxx	xxx
	EYE/PIN FLANGE	T11	298 ± 10%	291 ± 8%	266	216 ± 10%	xxx	xxx
		C11	250 ± 3%	239 ± 3%	215 ± 7%	xxx	xxx	xxx
		T22	84 ± 5%	77 ± 8%	76	75	65	xxx
		C22	66 ± 9%	62 ± 6%	57	58 ± 8%	55 ± 5%	xxx
		S	32 ± 7%	31 ± 10%	27 ± 6%	26 ± 3%	xxx	xxx

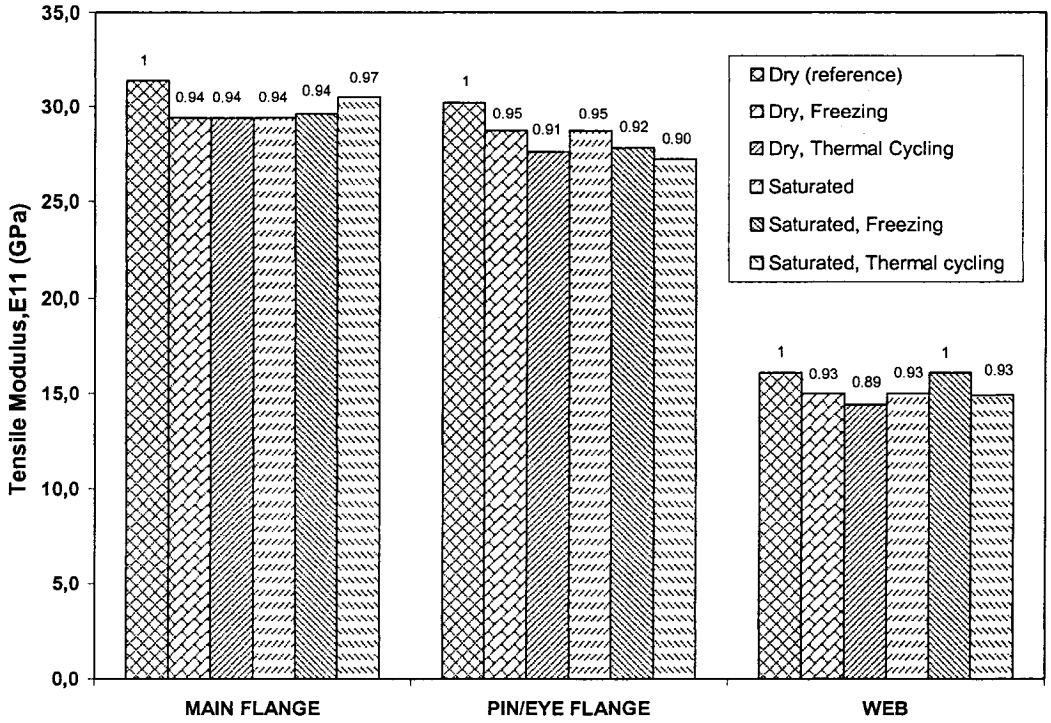

Figure 3.4: Effects of environmental conditions on tensile longitudinal modulus

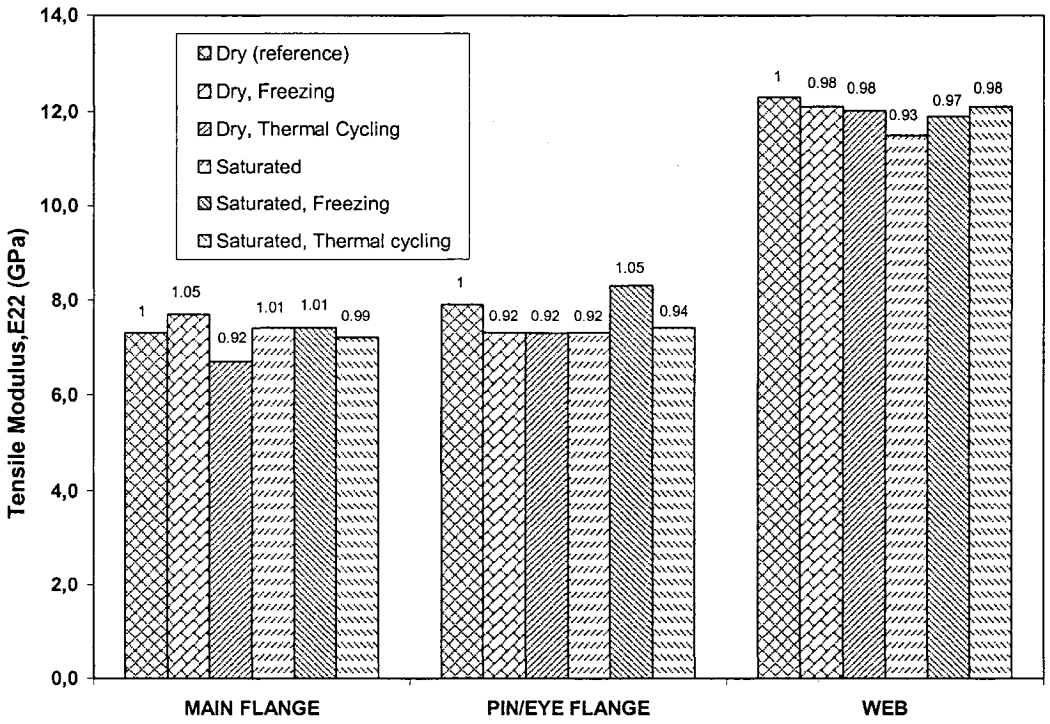

Figure 3.5: Effects of environmental conditions on tensile transverse modulus

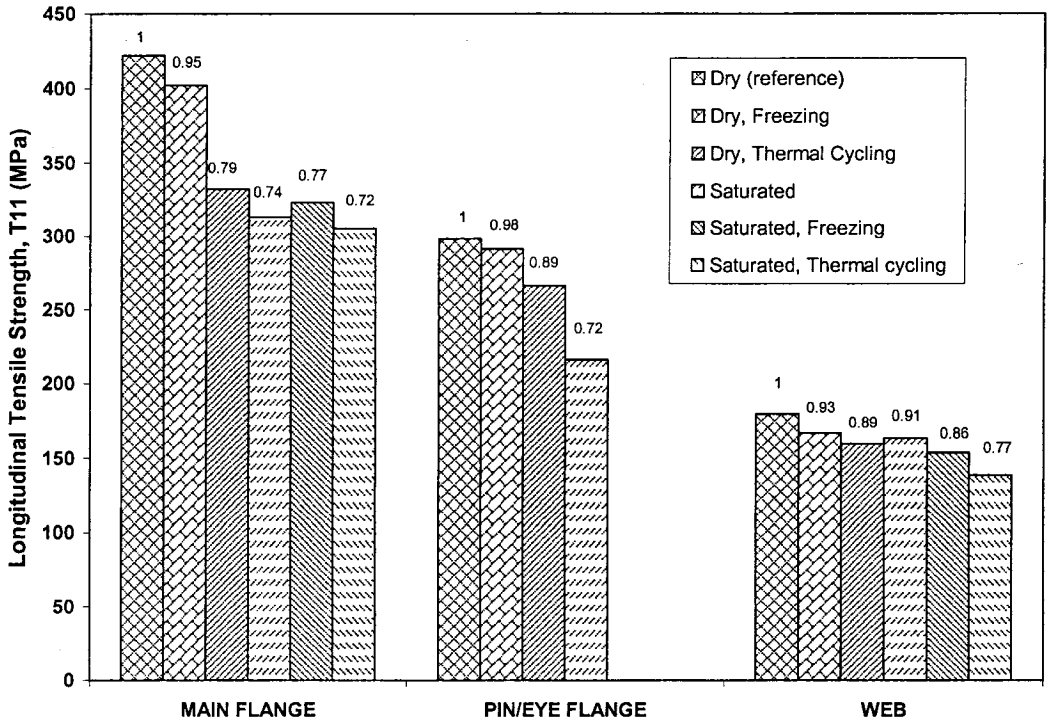

Figure 3.6: Effects of environmental conditions on longitudinal tensile strength

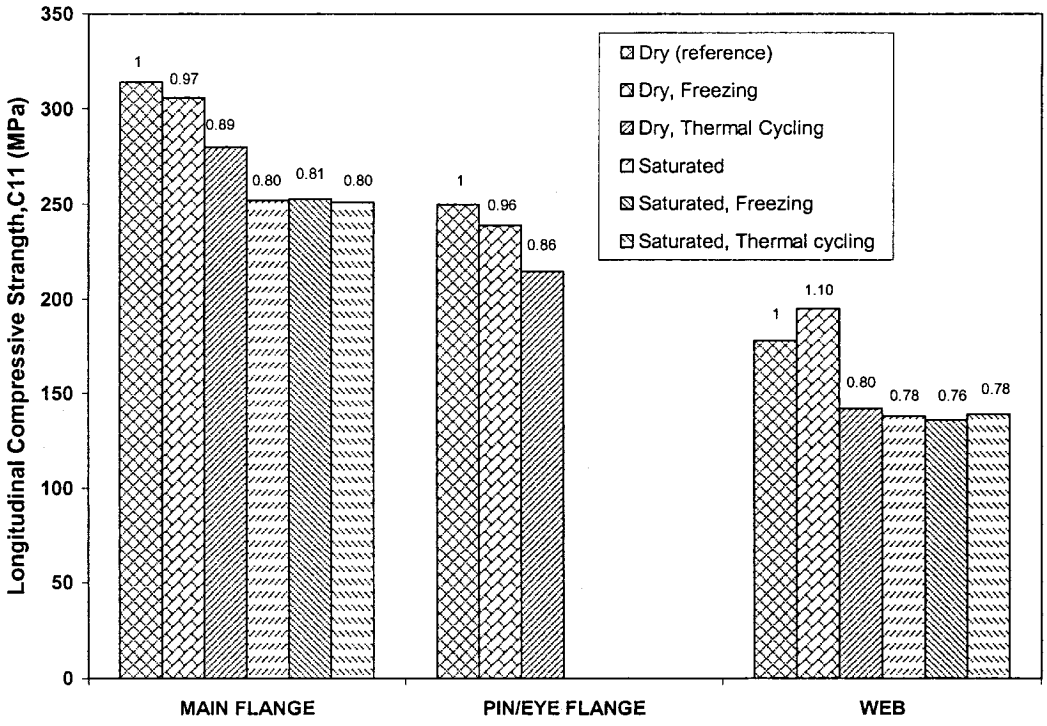

Figure 3.7: Effects of environmental conditions on longitudinal compressive strength

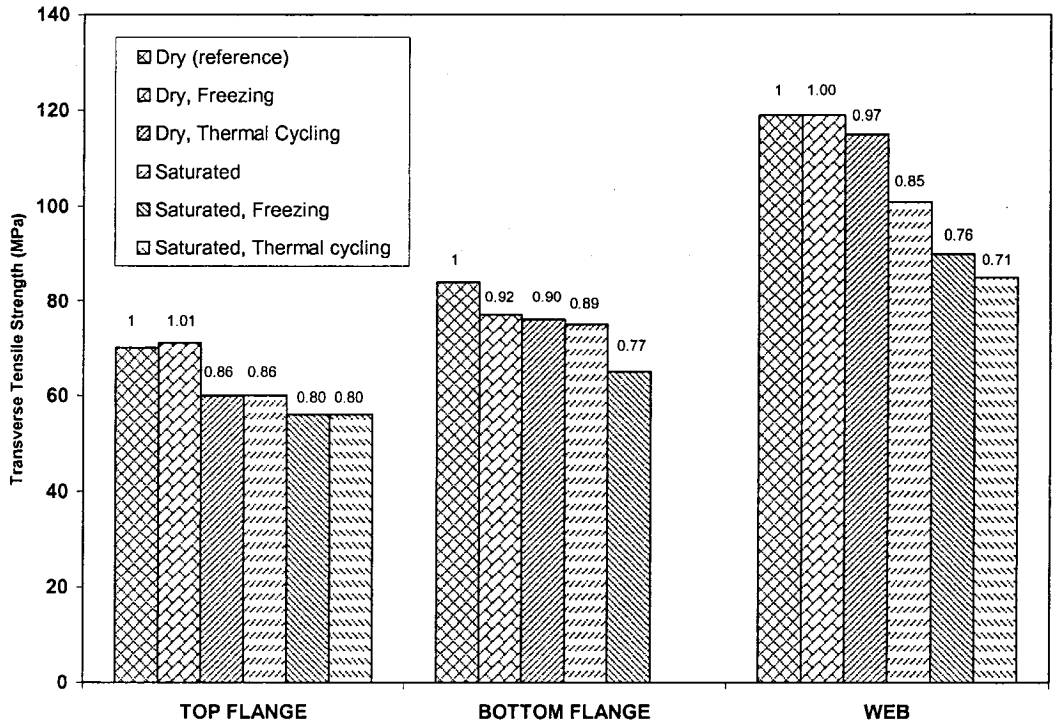

Figure 3.8: Effects of environmental conditions on transverse tensile strength

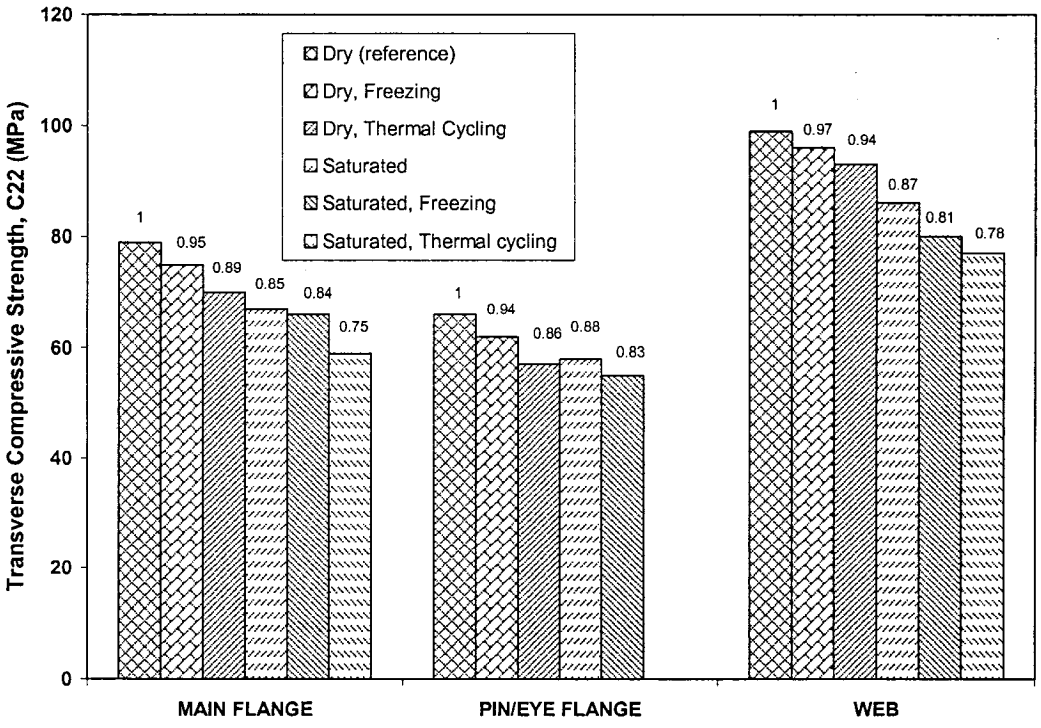

Figure 3.9: Effects of environmental conditions on transverse compressive strength

Comparisons of typical stress-strain curves of the main flange composite at different exposure regimes are presented in Figure 3.10. It was seen that the stiffness change was not considerable after exposure but the loss in strength was significant.

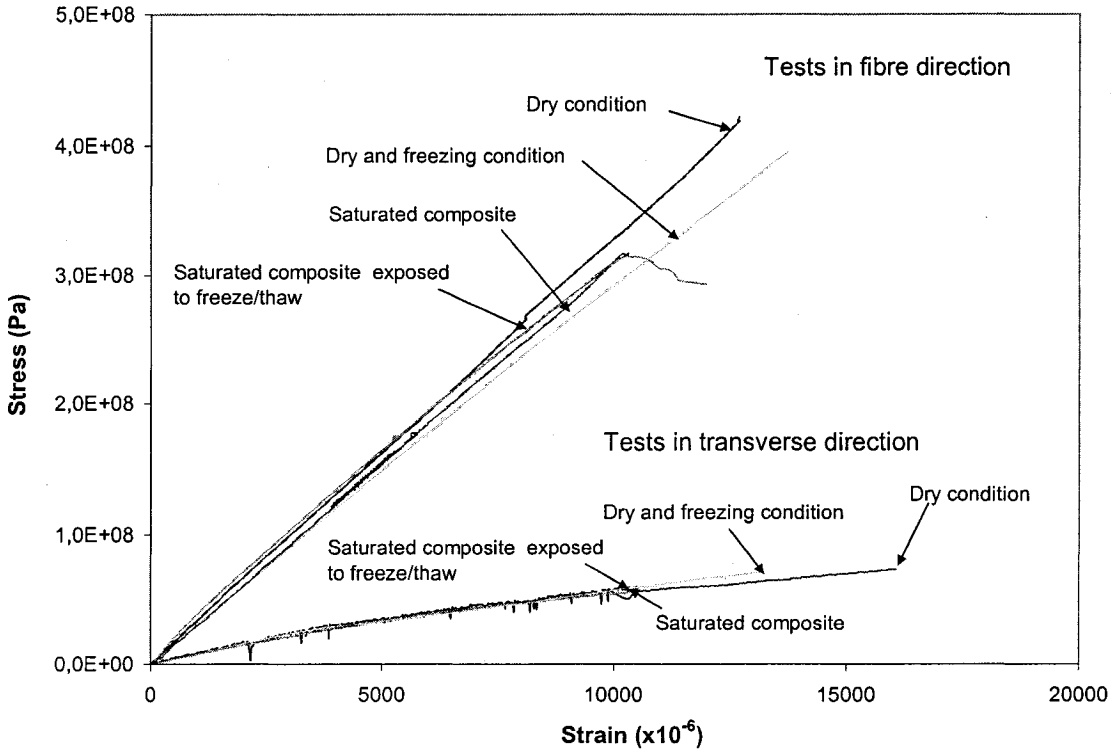

Figure 3.10: Effects of environmental conditions on the stress-strain curves of the main flange

In Figures 3.4 and 3.5, the variations of moduli E_{11} and E_{22} varied between +5% and -10%, and it seemed difficult to relate the variation trend to the exposure types, suggesting that the variation of the moduli was not related to the exposures but to the standard deviation of the test data. It is generally accepted that the harsh environment deteriorates the matrix, without damaging the glass fibres. Since E_{11} was mainly governed by the longitudinal fibres in the roving layer, and E_{22} by the fibres in the transverse layer, the stiffness change was not considerable.

In order to study the effect of each environmental exposure on the strength losses, Table 3.5 shows average losses for longitudinal and transverse directions. For the longitudinal

direction, C_{11} and T_{11} strength losses of web, main flange and eye/pin flange were averaged (totally six values when all available), whereas for results in transverse direction, C_{22} and T_{22} strength losses of web, main flange and eye/pin flange were averaged (totally six values when all available).

Table 3.5: Average ultimate strength losses for the two directions

Moisture	Dry	In water	Saturated	Saturated	Saturated
Temperature	-20°C	-20°C/+4°C	+4°C	-20°C	-20°C/+4°C
Longitudinal direction	-2% (± 12%)	-15% (± 6%)	-19% (± 11%)	-20% (± 6%)	-23% (± 5%)
Transverse direction	-4% (± 5%)	-10% (± 7%)	-13% (± 2%)	-20% (± 4%)	-24% (± 5%)

The dry freezing environment had little effect on the strength of the composite. The average reduction measured was 2 to 4% in Table 3.5. The dry composite was proven resistant to cold temperatures. The strength reduction was much more significant for the freeze/thaw cycling of dry composite. However, the cycling was done in water, and consequently, the coupons were left immerged 60 days. The reduction of the coupons for this batch could therefore have been caused by either freeze/thaw cycling, or by water absorption, or probably by both.

From Table 3.5, it was noticed for the last three environmental conditions with saturated composites, most of the degradation in the longitudinal direction occurred after the moisture uptake. An average of 81% of remaining strength was monitored after water saturation. Small additional damage was done by freeze/thaw or continuous freezing conditions with only 4% of subsequent damage. In Figure 3.6 and 3.7, this was particularly true for the longitudinal tensile strength, T_{11}, of the main and eye/pin flanges with respectively 74% and 72% of remaining strength after saturation; and for the longitudinal compressive strength, C_{11}, of the main flange and web with respectively 80% and 78% of remaining strength after water uptake. For those four constants, subsequent

freezing and freeze/thaw cycling conditions did not do further damage to the saturated composites. With respect to the longitudinal tensile strength of the web, the damage was shown to be more gradual: 9% reduction after saturation, 14% reduction for subsequent freezing and 23% reduction for subsequent freeze/thaw cycling. From Figures 3.6 and 3.7, it was also apparent that the longitudinal strength loss was slightly more significant in tension than in compression.

As regard to the transverse strength (T_{22} and C_{22}), the damage was found to be more progressive. In Table 3.5, the transverse direction was found to be more resistant than the longitudinal direction to the water uptake, with 13% of average strength loss. However, the subsequent freezing conditions and freeze/thaw cycles worsened the damage: after thermal cycles, the average remaining transverse strengths in the three composites decrease to 76%, a value comparable to the remaining strength in the longitudinal direction which was 77% under the same environmental conditions. Figures 3.8 and 3.9 confirmed this average trend: the transverse tensile strength, T_{22}, of the eye/pin flange and of the web and the transverse compressive strength, C_{22}, of the web and of the main flange showed gradual damage. Similar to the case of the longitudinal direction, comparison of Figures 3.8 and 3.9 showed that the strength loss in transverse direction was slightly more significant in tension than in compression.

It appeared that the strength reduction never exceeded 30% in both the transverse and longitudinal directions. Consequently, the ambient temperature water absorption tests produced much less strength loss than the hot water accelerated tests, where a strength loss of 60% was reported (Kouadio, 2002) for accelerated water absorption at 70°C, for the same composite.

Since the same results were obtained after 50 and 250 cycles for the saturated samples, it was concluded that most of the freeze/thaw damage to the saturated samples probably occurred during the first few cycles.

Chapter 4: Numerical Model

4.1 Geometry and material properties

The cross section of the FRP sheet pile panel is presented in Figure 4.1. To simplify the geometry, the section was divided into eleven different members; each member corresponded to one set of material properties and one thickness. A span of 2.13m was used as in the experiments (Shanmugan, 2004).

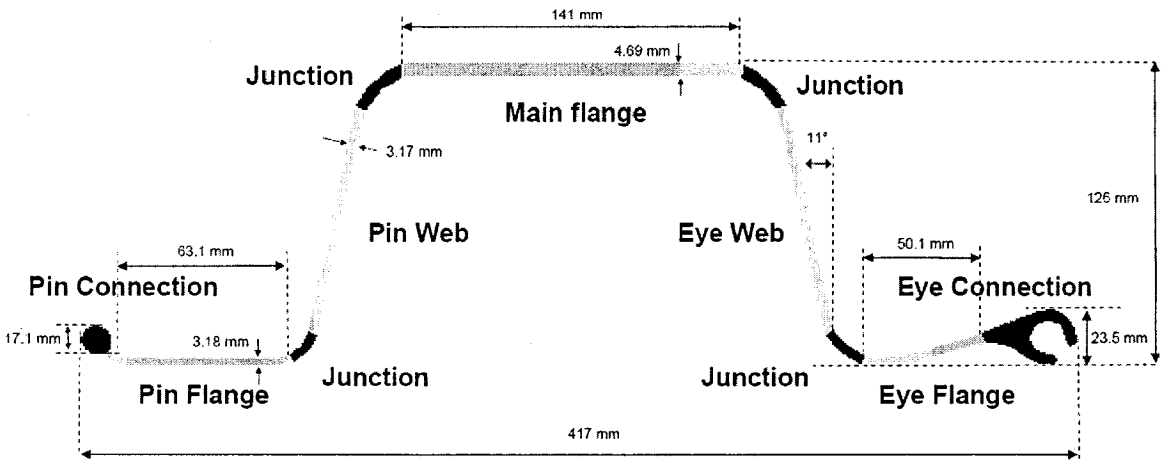

Figure 4.1: General layout of the panel section

Due to the small thickness to width ratio of the flanges and webs, shell elements were used. The effective round corners of the junctions were modelled in order to simulate with efficiency the restraints between the plates (especially important for the calculation of the buckling load).

Two different models were developed to simulate the pin and eye connections:

(1) The first model (which was called 3D-connection geometry) gave a 3D geometry of the connections. The exact geometry of the eye and pin connections was imported from the AutoCAD drawing of the panel. Difficulties appeared to connect the shell elements of the eye/pin flanges plates to the 3D elements of the connections: the 3D element nodes

have three degrees of freedom (three displacements), whereas the shell element nodes have six (displacements and rotations). A special option the FEM program allowing transition from shell to solid modelling (shell to solid coupling) was used.

(2) The second geometry (Shell-connection geometry) modelled the connections with shell elements with thickness computed to obtain the same cross section area as the effective connections.

Figure 4.2: Geometric modelling of the FRP panel
Left: 3D-connection geometry; Right: Shell-connection geometry.
In black: 3D elements; in grey: shell elements

The 3D-connection model was seen to be a lot more time consuming (more nodes and therefore more unknowns). Further studies with both model showed that the shell-connection model was sufficient (See Chapter 6).

The layer structure of the composite was not considered and was replaced by smeared properties (averaged properties for the composite laminate). All members of the section were assumed to be orthotropic materials and linear elastic up to failure:

(1) For the flanges and webs, material constants as input were obtained from coupon testing (Table 3.3). For simplification matters, only one modulus was used for compression and tension; the tension modulus was chosen.

(2) The junctions were assumed to have the same mechanical properties as the nearby flanges in the roving direction and the same mechanical properties as the nearby web in the transverse direction. This assumption relied on the fact that the junctions had the same longitudinal roving density as the nearby flange and that the CFM mat of the webs were prolonged in the junctions (see Figure 1.2).

(3) The connections were supposed to have the same properties as the main flange for they are mainly constituted of longitudinal roving. In the case of 3D-connection model, the extra material coefficient E_{33} was set equal to E_{22}.

4.2 Element used to take into account shear deformation, Mesh density

Due to the low shear modulus (G_{12}), composite sections usually experience large shear deformation in bending. The FEM program proposes three kinds of shell elements:

(1) General-purpose shell elements used to model thin or thick elements (S4R)

(2) Thin shell elements using Kirchoff shell theory (STRI3)

(3) Thick shell elements (S8R)

In order to select the correct one, a 4-Point-Bending beam test in a span of 2.13m was numerically simulated using the three kinds of shell elements, and the results were compared to the experimental data (Giroux, 2000) using EI = 206kN.m^2 and kAG = 872kN. Figure 4.3 shows the load-deflection curves obtained for the three elements along with the Timoshenko's prediction using equation (4.1).

$$\delta_{with\ shear\ deflection} = \frac{23}{1296}\frac{PL^3}{EI} + \frac{1}{6}\frac{PL}{kAG} \tag{4.1}$$

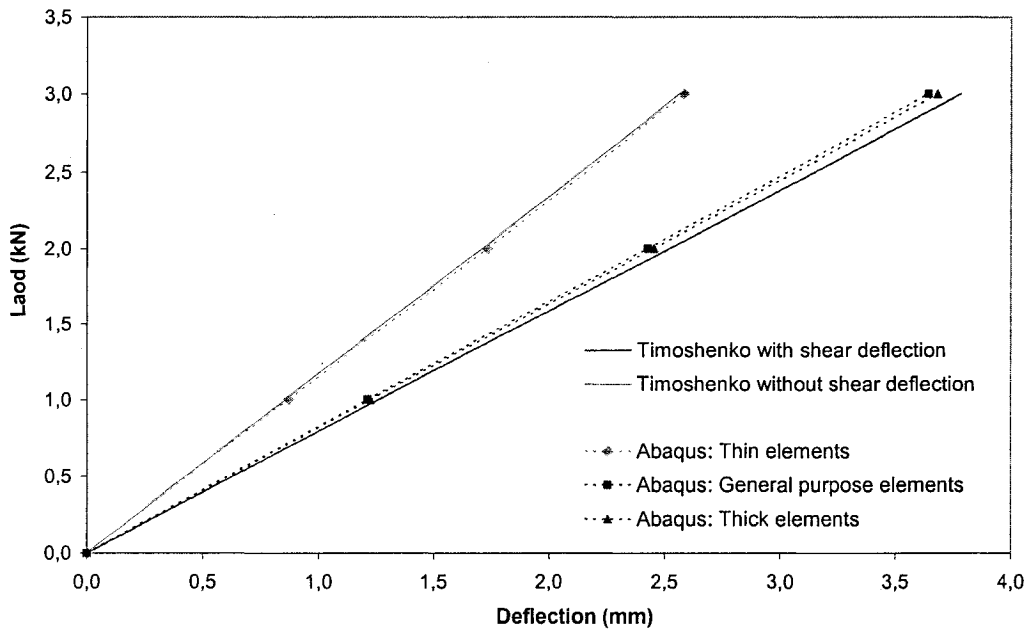

Figure 4.3: Comparison of element efficiency for shear calculations.

Obviously, the thin shell element was not sufficient to simulate the FRP beam with significant shear deflection for it only took into account the bending deflection: the load-deflection curve of the thin shell element was found to coincide with Timoshenko

bending-only curve (the first term of equation 4.1). Elements of S4R and S8R were both found to simulate with effectiveness the shear and bending deflections. In the following work, S4R was used for it required less nodes (four versus eight for the thick shell) and therefore less computational time for the same number of elements.

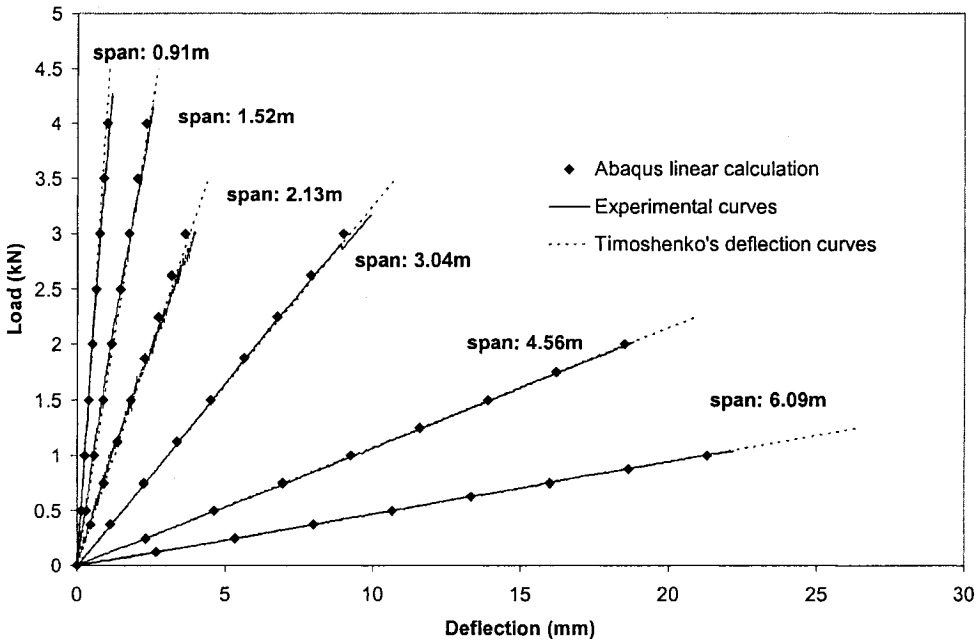

Figure 4.4: Experimental, analytical and numerical (using S4R shell elements) four point bending tests for six different spans.

The S4R element was used to simulate four-point bending tests within the linear proportional limit at six different spans: 0.91m, 1.52m, 2.13m, 3.04m, 4.56m and 6.09m (Giroux, 2000). Results are presented in Figure 4.4. The numerical, experimental and analytical load-deflection curves agreed with accuracy. From the short beams where shear deflection was dominant to the long ones where bending was governing, the S4R element performed with satisfaction.

The mesh density was chosen as to obtain accurate results. For this purpose, the element density was increased until the convergence of the results for the pre-buckling, buckling and post-buckling of the panels (see Chapter 6 and 7) was judged satisfactory. The density of the elements was enhanced at mid-span of the panels where the buckling behaviour was expected. The shell-connection model was made of 9200 shell elements

(see Figure 6.1 for mesh density: 92 elements in the transverse direction and 100 elements in the longitudinal direction). The 3D-connection model was made of 6700 shell elements and 6500 3D elements (see Figure 6.8 for mesh density).

4.3 Boundary conditions and uniform pressure load

Loads and boundary conditions were applied to the sheet pile panel in a way to simulate the laboratory experiments of sheet pile panels subjected to uniform pressure to the best accuracy. An analysis of the experimental setup was necessary to match the numerical model. The experimental layout can be seen in Figure2.2.

4.3.1 Loading Inputs

In experiments (Shanmugan, 2004), foam was inserted between the air bag and the panel to transfer the load. It was idealised in the numerical model to be represented by a vertically distributed force on the entire section of the beam. Figure 4.5 shows the loading inputs for the single panel cross section at standard and reverse installation position.

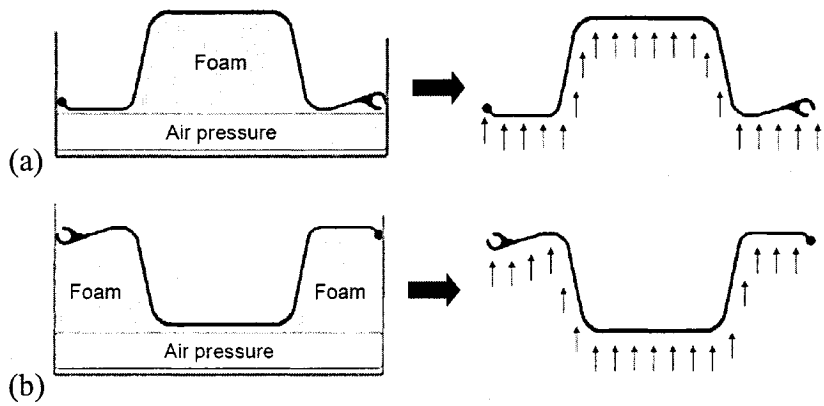

Figure 4.5: Load model of the (a) standard (b) reverse installation positions

In the effective experimental case, as the section deformed, the forces at each node slightly changed. However, this non-linear phenomenon was very difficult to simulate. Consequently, the force at each node of the section was supposed to remain constant throughout the numerical calculation. For the reverse loading configuration, the force vectors were simply inverted from the standard case as show in Figure 4.5.

4.3.2 Boundary conditions

Three different kinds of boundary conditions were necessary to simulate the entire layout of the experiments: ends conditions, cross section constraints (interface with steel frame) and finally the interlocking connections between the panels (when connected panel was considered). The panel was supported by a line at each end where boundary conditions were imposed as roller (in the longitudinal direction) on one end and pinned on the other.

The cross section constraints of the single panel depended on the two installation configurations. In standard position, the section tended to open (see dashed arrows in Figure 4.6); therefore the pin/eye flanges were, all along the loading, transversely restrained by the steel frames. In reverse position, on the contrary, the section tended to close (dashed arrows in Figure 4.6): thus, no direct contact existed between the pin/eye flanges and the steel frames. Consequently, no constraints were considered. Equivalent boundary conditions were defined for the 3D connection model in single configuration.

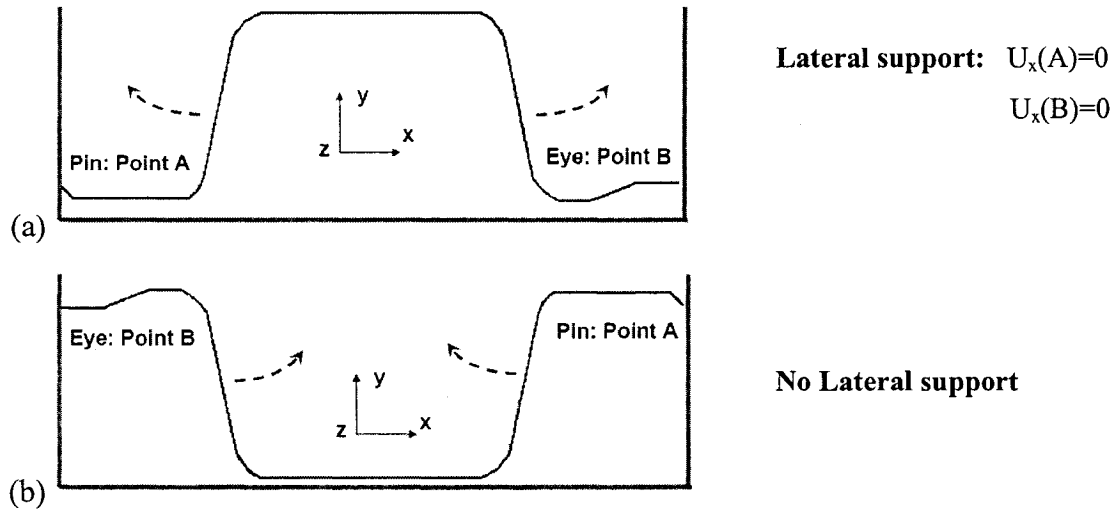

Figure 4.6: Cross section boundary for the (a) standard, (b) reverse single panels

The interlocking connection was more complicated to simulate. For the shell-connection model, a sheet pile constituted of an infinite number of panels was simulated as shown in Figure 4.7. Because of the symmetry of translation of the structure, all panels behave in

the exact same way. Therefore, one single panel was used with translation symmetry boundary conditions

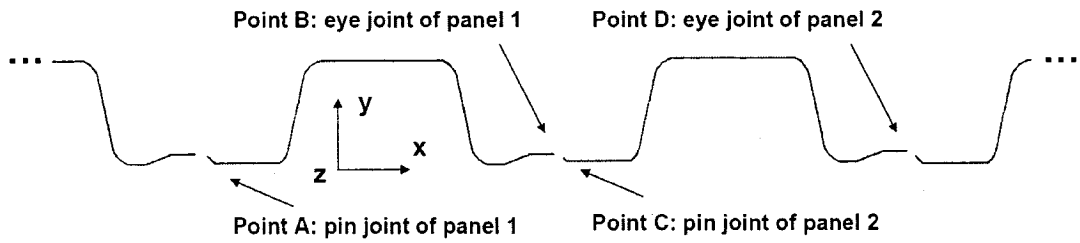

Figure 4.7: Model of the infinite sheet pile wall with shell connection models

Because all panels behave in the exact same way, the displacements in the x and y directions of nodes A and C are equal all along the longitudinal direction (equivalent relations for nodes B and D):

$$U_x(A)=U_x(C)\ ;\ U_y(A)=U_y(C) \tag{4.1}$$

The longitudinal ball in socket connection is assumed to be a perfect pin connection along z. Consequently the relative z-displacement and z-rotation of nodes B and C are completely free. In the x and y direction, the displacements are continuous:

$$U_x(B)=U_x(C);\ U_y(B)=U_y(C) \tag{4.2}$$

By combining Equations (4.1) and Equations (4.2), it is derived that nodes A, B, C and D have all equal x and y displacements. Therefore, it is found possible to reduce the problem to one single panel with the boundary conditions assumed in Figure 4.8. Equivalent boundary conditions were used for the reverse position connected panel.

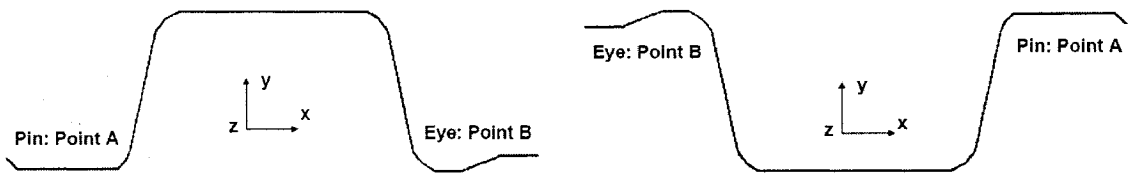

$$U_y(A)=U_y(B);\ U_x(A)=U_x(B)$$

Fig 4.8: Cross section boundary conditions for the standard and reverse connected panels (Shell connection model)

In order to verity the precedent assumptions, two 3D-connection profiles were generated and contact properties were defined on the pin and eye connections. The surface based contact simulation was used and a contact pair was defined between the surface of the eye and the surface of the pin connector. The properties of the interface were defined without friction and using the finite-sliding formulation, which assumes unlimited sliding between the two contact pair's surfaces. The two unconnected flanges were supposed transversely restrained (Figure 4.9).

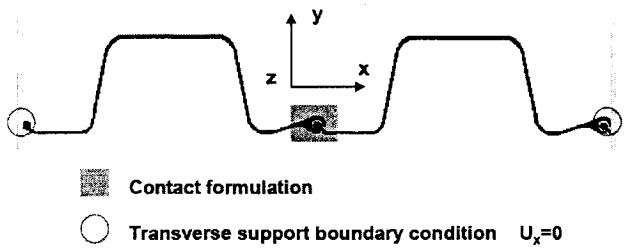

Figure 4.9: Cross section boundary conditions for the connected 3D-connection panels

4.4 Time efficiency of the four models.

The sizes of the different models are shown in Table 4.1. The time index used represents the computational time needed to calculate the deformed shape of the FRP panel in standard position at a pressure of 10 kPa. The shell-connection model was always less time consuming because of the larger number of variables of the 3D-connection model. As regard to the 3D-connection connected model, the contact algorithm introduced a huge amount of additional calculations. Therefore, the first step of the work was to verify the accuracy of the shell-connection model.

Table 4.1: Computational time of the four numerical models

Model	Number of elements	Time index
Single – Shell connections	92 000	1 min
Single – 3D connections	132 000	4 min
Connected – Shell connections	92 000	1 min
Connected – 3D connections	264 000	70 min

Chapter 5: Theory of the Numerical Algorithms Used in the FEM Calculation

The FEM program proposes a complete set of calculation options which permits to calculate the pre-buckling (section 5.1), buckling (5.2), post-buckling (5.3) and failure (5.4) of composite shapes. This chapter is to review entirely the theory of numerical algorithms proposed in the Abaqus documentation (Abaqus, 2004).

5.1 Non-Linear pre-buckling calculation

Non-linear response was observed in the experimental pressure-strain and pressure-deflection curves of sheet piles in the pre-buckling stage of the loading (Shanmugan, 2004). In order to simulate the experiments, the following assumptions were made:

(1) No nonlinearities due to contact or friction between the panel and the steel frame.

(2) No nonlinearities due to material properties. It was seen in Chapter 3 that the composite plasticity was quite negligible.

(3) Only geometrical nonlinearity (large displacements, large rotations and large strains) were taken into consideration.

Classic static nonlinear calculation (Newton Raphson Method) was proceeded in order to obtain the pre-buckling behaviour of the panel. Because of these nonlinearities, an incremental and iterative approach was necessary to obtain the field outputs. The mathematical formulation of the static problem at an increment number "i" is stated in Equation (5.1).

$$\left(\mathbf{K_{linear}} + \mathbf{K_{geometric}(P_i)} \right) . \mathbf{v_i} = \mathbf{\Delta P_i} \qquad (5.1)$$

Where:

$K_{linear} + K_{geometric}(P_i)$ is the tangent matrix of the structure at load P_i.

P_i is the current load (P_i=0 at first increment).

v_i and ΔP_i are respectively incremental displacement and load.

K_{linear} is the linear elastic rigidity matrix.

$K_{geometric}$ is the geometrical rigidity matrix; it takes into account the geometric nonlinearities of the system. Since it is a function of the loading, it is the non linear term.

The left-hand side of static Equation (5.1) is the incremental internal force which is set equal to the incremental external loads, ΔP_i.

5.2 Bifurcation loading calculation

In certain case, the term $\mathbf{K_{geometric}(P_i)}$ in Equation (5.1) can lead to instability problem. At a certain load Pi, the tangent matrix $\mathbf{K_{linear} + K_{geometric}(P_i)}$ can become singular. Because it becomes non reversible, Equation (5.1) can have more than one solution. From this load Pi, several equilibrium paths exist; therefore Pi is called a bifurcation loading.

The bifurcation load is mathematically defined by the following relationship:

$$\mathbf{Determinant\ (K_{linear} + K_{geometric}(P_{bifurcation}))= 0} \tag{5.2}$$

The physical process underlying the mathematical concept of bifurcation load is buckling behaviour. When the rigidity matrix becomes singular, out of plane displacements (or non trivial displacements) are permitted. At the bifurcation loading, Equation (5.3) has two solutions.

$$\mathbf{(K_{linear} + K_{geometric}(P_{bifurcation})) \cdot v_{mode\ shape} = 0} \tag{5.3}$$

The first solution is the trivial zero solution and the other one is out of plane displacements (waves in plates, for example), also called buckling mode.

To find the bifurcation load of a structure, it is necessary to solve Equation (5.2) for $P_{bifurcation}$. To transform this difficult non linear problem into a much simpler linear eigenvalue problem, the perturbation model is used. Perturbation means that the structure is placed in a base state and assumed to be having a linear behaviour around it. Equation (5.3) is transformed into Equation (5.4). The 0 subscript represent the base state

$$\mathbf{P_{buckling} = P_0 + \lambda P, \text{ and } (K_0 + \lambda K_\Delta) \cdot v_i = 0 \ (\lambda \text{ and } v_i \text{ are unknowns})} \qquad (5.4)$$

Where,

P is the perturbation load (which will trigger the buckling) and Po is the dead load.

$Ko = K_{linear} + K_{geo}\ (P_0)$ is the stiffness matrix corresponding to the base state. When no dead load is considered, it is exactly the linear matrix. When dead loads are applied, it includes the non-linear geometric effect of the dead loads.

K_Δ is the differential stiffness matrix.

λ is the incremental factor (unknown).

v is a unknown DOF vector column corresponding to the buckling displacement.

From this calculation, it is possible to find the buckling load: $(\lambda_i P+P_0)$ and the corresponding mode shape v_i, which reveals of the post-buckling shape of the structure after the critical load.

Because this method is a linear perturbation step it is valid only near the base step. In other word λP must not be too large. Generally speaking, the results are found to be good when the equilibrium path from load P_0 to $P_0+ \lambda P$ is near to linear. In the present case of the FRP panel, since the behaviour is strongly non-linear up to the experimental buckling load, the buckling calculation must be done on a loaded base state. This loaded base state P_0 should be taken as near as possible from the numerical bifurcation load in order to minimize errors. Incorporating pre-buckling non-linear deformation in a buckling calculation for FRP structures was strongly suggested by Brooks and Turvey (1995).

Equation (5.4) has more than one solution. However, in most analyzes, the buckling mode corresponding to the lowest value of λ is the one of interest.

5.3 Post-buckling calculation after bifurcation load

Because the post-buckling behaviour of the panel was searched, it was seen necessary to pursue the numerical calculation after the bifurcation load. The use of the Newton Raphson algorithm is efficient if the equilibrium path is smooth and does not bifurcate brutally. In the case of brutal change of the slope of the equilibrium path, the algorithm stops for convergence problem (See Figure 5.1). Sudden bifurcation is usually due to buckling phenomenon.

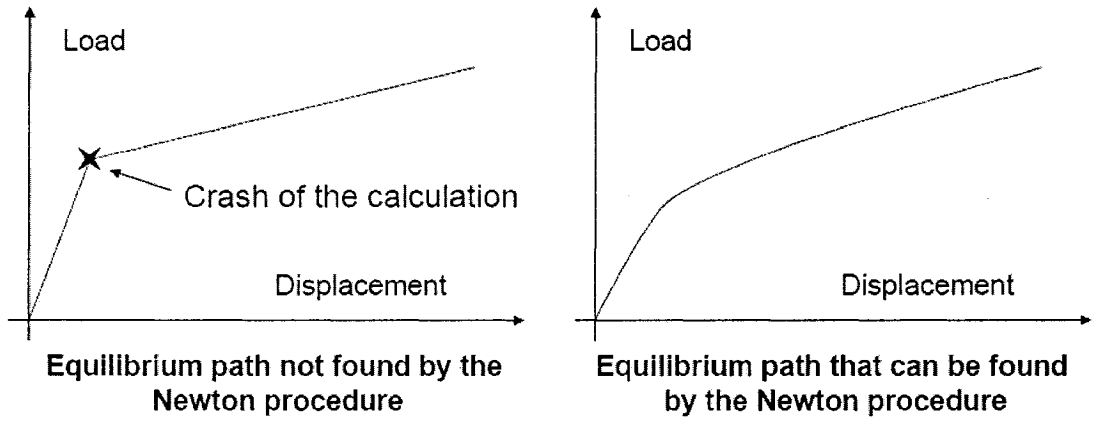

Fig 5.1: View of equilibrium paths found and not found by Newton procedure

Two methods are usually used to solve post-buckling problem, both of which will be used in the FRP panel calculations:

(1) Introducing imperfections in the initial geometry

(2) Introducing dynamics

5.3.1 Introducing imperfection in the initial geometry

One solution to bypass this "bifurcation" difficulty is to artificially smoothen the equilibrium path: this can be done by adding some geometric imperfections to the initial perfect geometry of the structure. If the imperfections are well chosen, the new equilibrium path will be continuous and adequate for a nonlinear calculation. In order to

succeed in the calculation, it is necessary to perturb the structure in the expected buckling mode. Therefore, it is usual to introduce imperfections similar to the buckling mode found in the bifurcation loading calculation.

The main drawback of this "trigger" imperfection is that it underestimates the critical load because the structure collapses more easily; the "error" introduced depends on the sensibility of the buckling of the structure to imperfections. However, in the case of structures made of flat plates (like the FRP sheet pile studied herein), if the amplitude of the imperfection is small enough, the post-buckling behaviour obtained will be very close to the one of the perfect geometry; buckling and post-buckling behaviours of flat plate structures are indeed not extremely sensible to imperfections. Therefore, by combining the results of the perfect and imperfect structures, the entire problem can be solved:

- The bifurcation loading is found by a regular buckling eigenvalue calculation.
- The post-buckling curves are given by the imperfect structure.

5.3.2 Introducing dynamics in the calculation

Another solution to go beyond the bifurcation point is to treat the problem dynamically, i.e. introducing a rate of loading and a mass matrix of the panel. At the bifurcation point, the structure is willing to release strain energy in order to remain in equilibrium. With the help of dynamics, the structure will snap in its post-buckling shape by releasing strain energy in the form of kinematic energy.

The post buckling curves obtained are of course a function of the load rate used to perform the calculation. The buckling load is always overestimated in dynamic calculation. However, since the loading rate is chosen very small, the panel will be in a quasi-static mode.

5.4 Failure criteria used throughout the thesis

In order to calculate the failure loads of the panels, two composite failure criteria were used. The simplest one is the Maximum stress criterion: it does not consider any stress interaction and judges failure to occur when the stress in any direction exceeds the strength in that direction. The Tsai Hill criterion is generally used to predict the failure of long fibre composites. Unlike the maximum stress criterion, it accounts for mixed mode failures. The mathematical formulations are stated in Equation (5.5) and (5.6).

If $\sigma_{11}>0$, then $X = T_{11}$, otherwise $X=C_{11}$; If $\sigma_{22}>0$, then $Y = T_{22}$, otherwise $Y=C_{22}$

(1) Maximum stress criterion: failure if $\max\left(\frac{\sigma_{11}}{X}, \frac{\sigma_{22}}{Y}, \left|\frac{\sigma_{12}}{S}\right|\right) = 1$ (5.5)

(2) Tsai Hill criterion: failure if $\frac{\sigma_{11}^2}{X^2} - \frac{\sigma_{11}\sigma_{22}}{X^2} + \frac{\sigma_{22}^2}{Y^2} + \frac{\sigma_{12}^2}{S^2} = 1$ (5.6)

Where, T_{11} and C_{11} are respectively the tensile and compressive ultimate strengths in the roving direction, and T_{22} and C_{22} are respectively the tensile and compressive ultimate strengths in the transverse direction.

Many other criteria exist for composite plates. In the following work, it was seen that the use of the Max Stress Criteria was largely sufficient to predict with success the failure of the panel and the Tsai-Hill criterion was used for confirmation. A special option (*FAIL STRESS) available in the FEM program allows to define the five ultimate stresses (T_{11}, C_{11}, T_{22}, C_{22} and S_{12}) as inputs for an anisotropic material. The output option CFAILURE automatically calculates the combinations of stresses of Equations (5.5) and (5.6) for every element of the model. In chapters 6 to 9, the failure load of the sheet pile was defined as the pressure to which those combinations of stresses exceeded one in any element of the numerical model. Consequently, it was assumed that the local failure of the composite (whatever the location) initiated directly the general failure of the sheet pile. The application of strength criteria did not consider any progressive failure.

5.5 Overview of the calculations

Figure 5.2 summarizes the steps of the calculation which were used in Chapter 6, 7, 8 and 9. Step 1, 2 and 3 must be run one after another, whereas step 4 can be processed directly. These steps are classical buckling calculations referenced in the Abaqus examples of the Abaqus documentation.

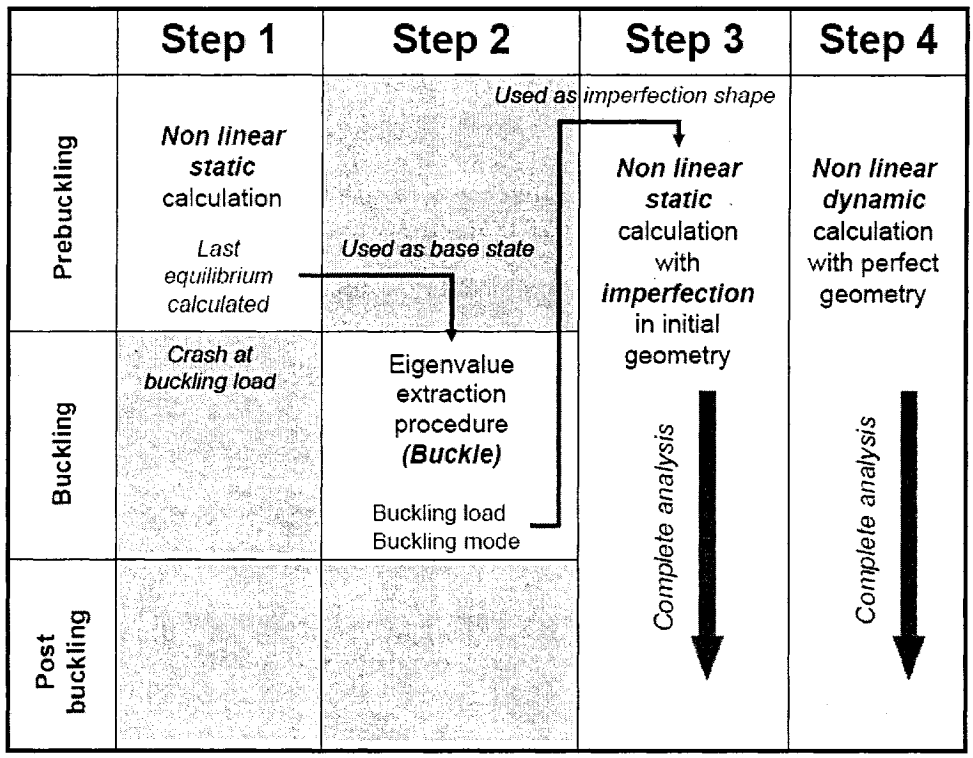

Fig 5.2: Calculation chart of the buckling analysis using FEM
Abaqus/standard key words are in italic bold characters.

In chapter 6, 7, 8 and 9, references to the steps of Figure 5.2 were made when describing the calculations done.

Chapter 6: Finite Element Analysis of FRP Sheet Pile Panel at Standard Position

6.1 Non linear, pre-buckling behaviour of the single panel in standard position

The two sheet pile models (with shell connections, and 3D connections) were progressively loaded by a transverse pressure increasing by steps of 2 kPa, from 0 kPa to 50 kPa. At some point during the calculations, the program stopped for convergence problem due to the existence of a bifurcation loading: they were 42 kPa for the shell-connection model and 44 kPa for the 3D-connection model.

The boundary conditions and load inputs for the single standard position panel were described in Section 4.3. Figure 6.1 shows the deformed shape of the single shell-connection model at 40 kPa.

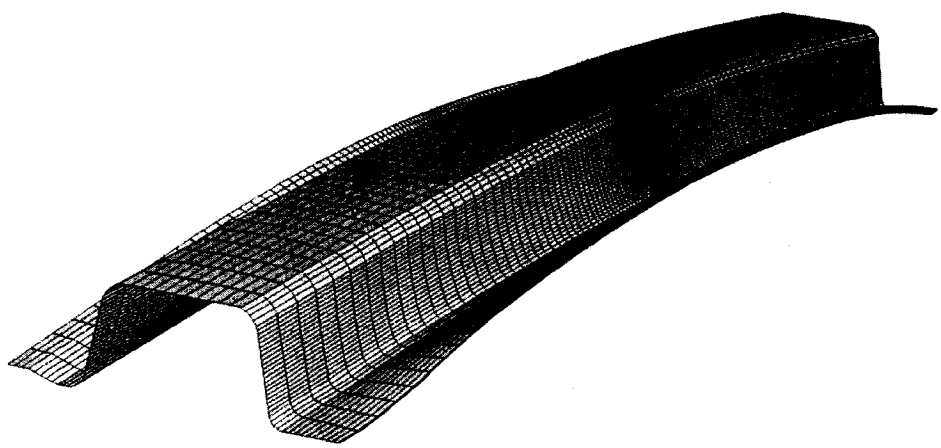

Fig.6.1: Standard position panel at 40 kPa (Shell connection model)

In order to validate the models, the outputs of the numerical pre-buckling calculations were compared to the experimental data of single panel tests. The pressure-deflection curves of the main flange obtained by the two numerical models and by experiments are

presented in Figure 6.2. Shell-connection model and 3D-connection model agreed well with experimental results. The comparison also implied that the shell-connection model is equivalent to the 3D-connection model.

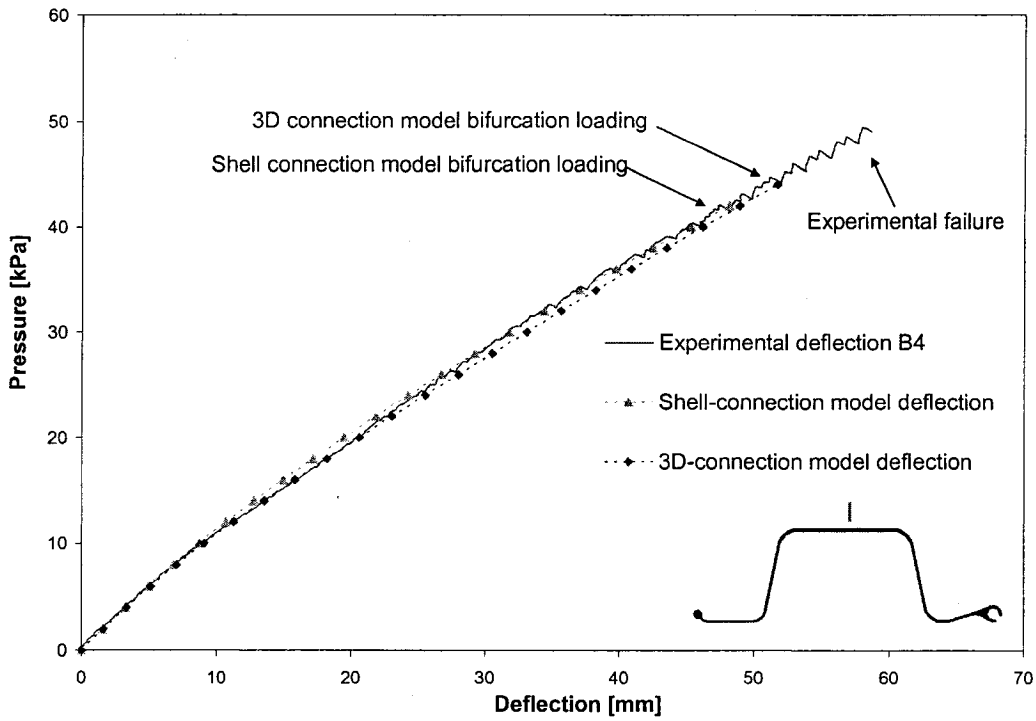

Fig.6.2: Experimental and numerical deflections for the single standard position panel

The experimental strain data were obtained on the top of the three flanges (pin, eye and main flanges). The strains were measured in the fibre direction on the middle span section of the beam with gage location. The strain gauges were placed at the middle of each flange (Figure 6.3).

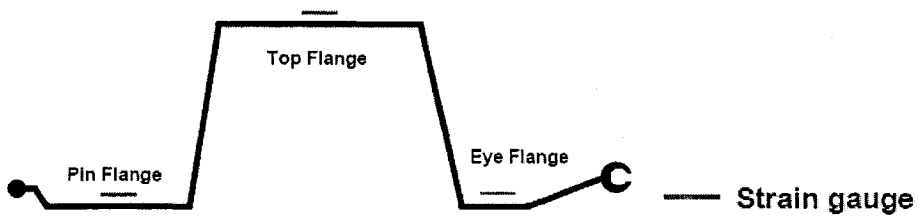

Fig.6.3: Strain gauges placements for the single standard position panel

The values were compared to the FEM output data in Figure 6.4. In order to obtain comparable values, the strain on the top of the three flanges ($\epsilon_{effective}$) was computed with Equation (6.1) from the FEM strain output, SE1 value of strain at the mid-thickness of the plate; the longitudinal curvature output, SK1; and the thickness of the plate, t.

$$\varepsilon_{effective} = SE1 + \frac{t}{2}.SK1 \tag{6.1}$$

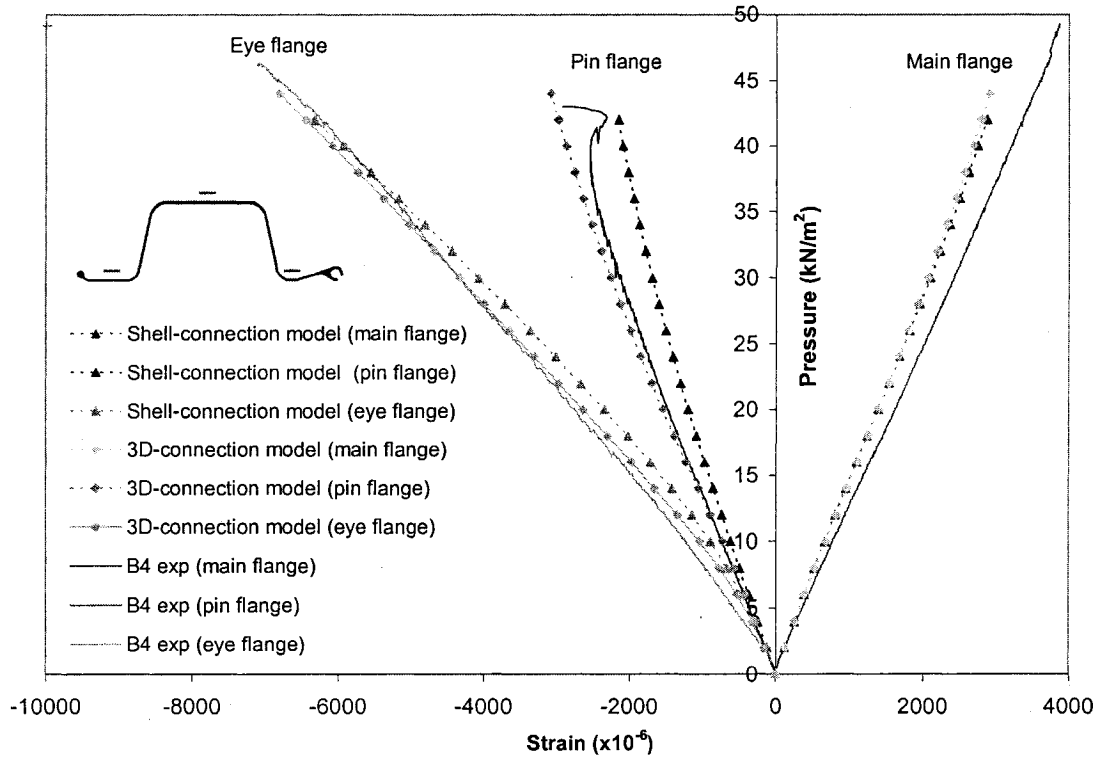

Fig.6.4: Experimental and numerical strain data for the single standard position panel

The comparative results agreed well for the two models. Deflection and strains were very well predicted by the FEA program. Furthermore, FEM curves for the 3D-Connection and the Shell-connection models were very close. Therefore, the Shell-connection model appeared to be sufficient to predict the behaviour of the single panel. Consequently, detailing of the connections did not seem to be critical for the Prebuckling behaviour of the single panel.

6.2 Non-linear, prebuckling behaviour of connected panels in standard position

The next step was to simulate the pre-buckling behaviour of the connected panel configuration. As for the single panel, the simulation outputs were compared with the experimental data (deflection and strain with bending correction).

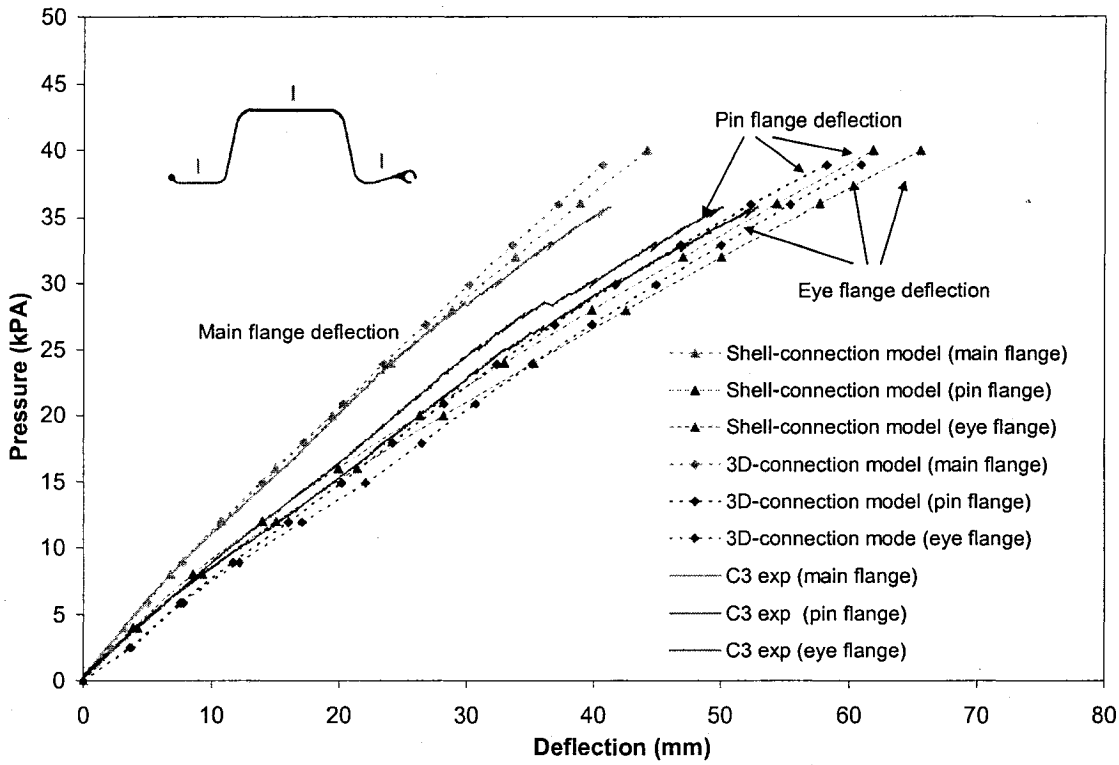

Fig.6.5: Experimental and numerical deflections for the connected configuration

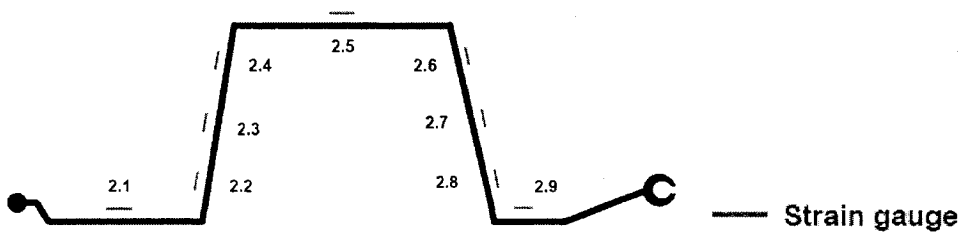

Fig.6.6: Strain gauges placements for the connected standard position panel

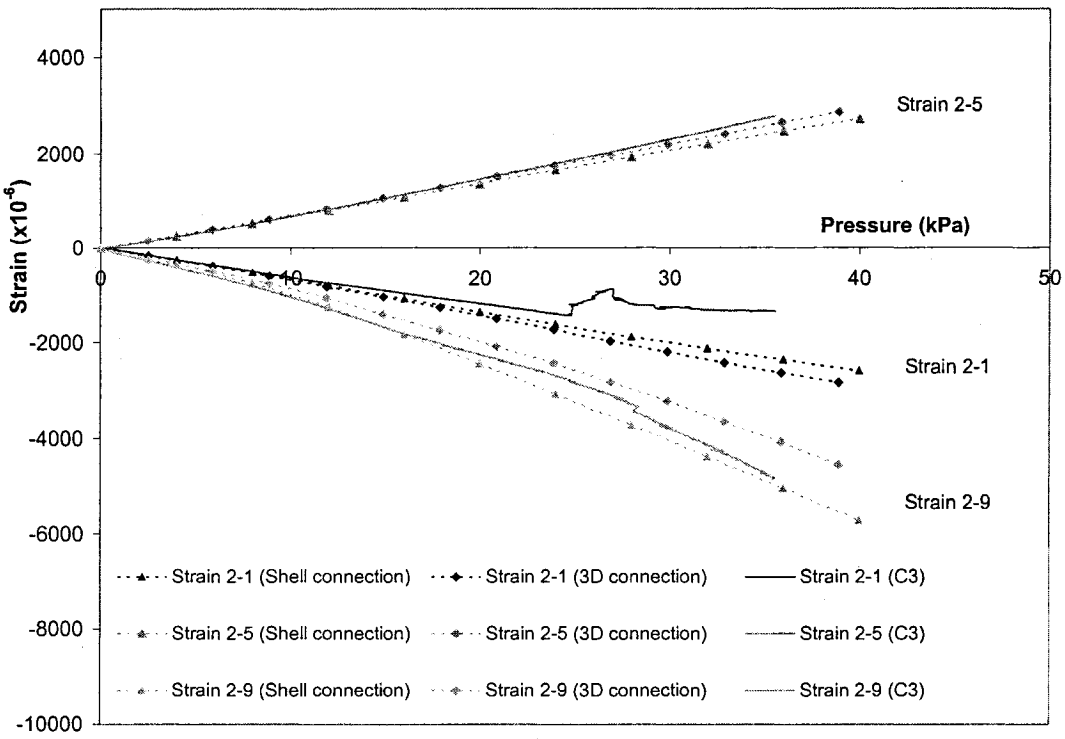

(a) Comparative strains in the three flanges

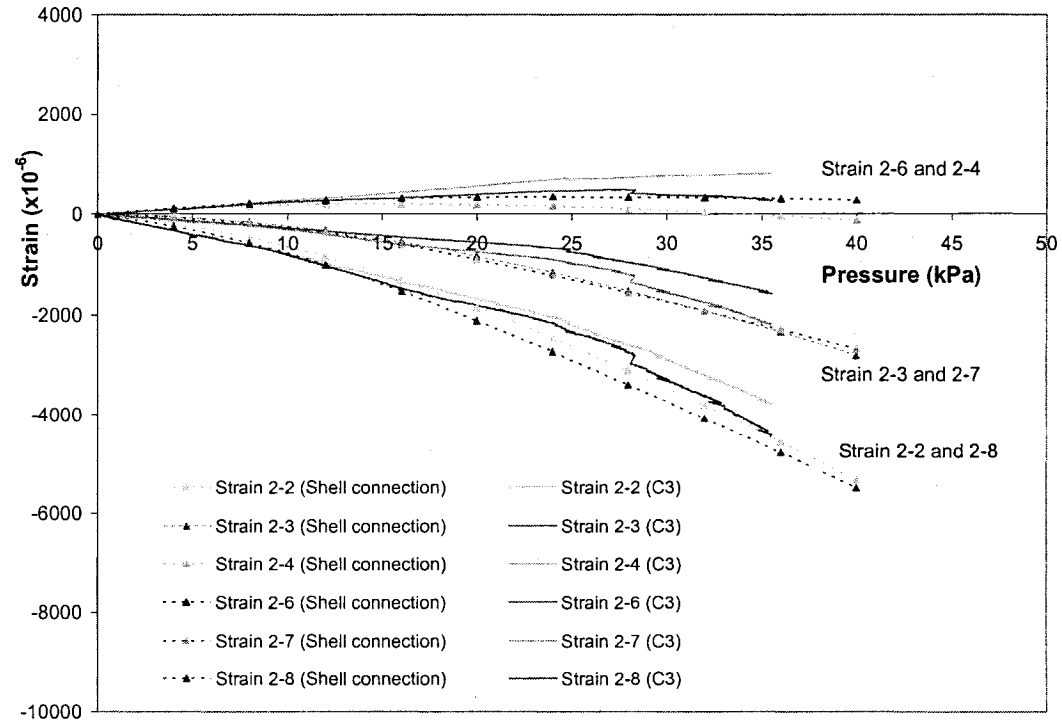

(b) Comparative strains in the two webs

Fig.6.7: Experimental and numerical strains in the connected configuration. (Gauge locations are shown on Figure 6.6)

The comparative deflections of the three flanges are shown in Figure 6.5. The comparative strain data are shown in Figure 6.7. For the strains in the three flanges, both models were used (3D-connection and shell-connection models), whereas for the strains in webs, only the shell connection model was shown to avoid overload of the Figure. The FEA analysis gave very good prediction for all pre-buckling curves: all FEM curves were very close to the experimental results. It was interesting to notice that the numerical pressure-deflection and pressure-strain curves exhibited softening behaviour. In Figure 6.5, the deflections of the pin/eye flanges were larger than the deflection of the main flange. It was due to the bending of the two compressive flanges about junctions, leading to the shift of the neutral axis of the section towards the main flange and the reduction in flexural rigidity. In Figure 6.7, it was clear that the neutral axis was positioned initially half way between strain gauges 2-3 and 2-4 and gauges 2-6 and 2-7. With the increase of the pressure and the increase of the compressive strains in gauges 2-3 and 2-7, the neutral axis moved towards strain gauges 2-4 and 2-6. The flexural rigidity reduction explained the non-linear softening response in the load-deflection curves (Figure 6.6). The non-linear deformation of the section is visible in Figure 6.8.

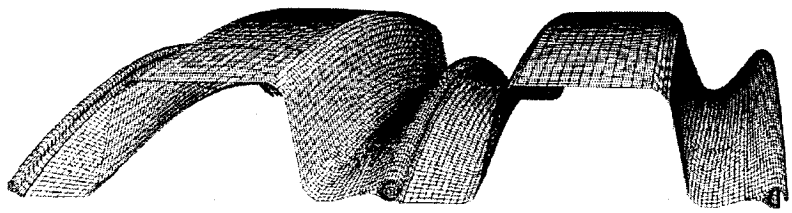

Figure 6.8: Non linear deformation of the 3D connected model section at 40 kPa

The ball in socket connection was studied more closely with the 3D connection model. Figure 6.9 shows the calculated rotation of the pin ball in the eye connection at 0 kPa, 9 kPa, 21 kPa, 30 kPa and 39 kPa. It was noticed that from 0 kPa to 21 kPa, the relative rotation was completely free which resulted in the sliding of the pin ball along the inner surface of the eye circle. At 20 kPa, a second contact zone appeared between the pin flange and the bottom edge of the eye circle. This new contact zone restrained the relative rotation from 20 kPa to 40 kPa. Also in Figure 6.9 was calculated the eye width (distance between the two points of the arrow on the 0 kPa deformed shape). While the rotation was free, the width remained constant. From 20 kPa, the width started to increase,

showing that the rotation continued but was restrained. The tearing (Figure 6.10) of the eye circle could lead to the failure of the connection (Pin and Eye separation).

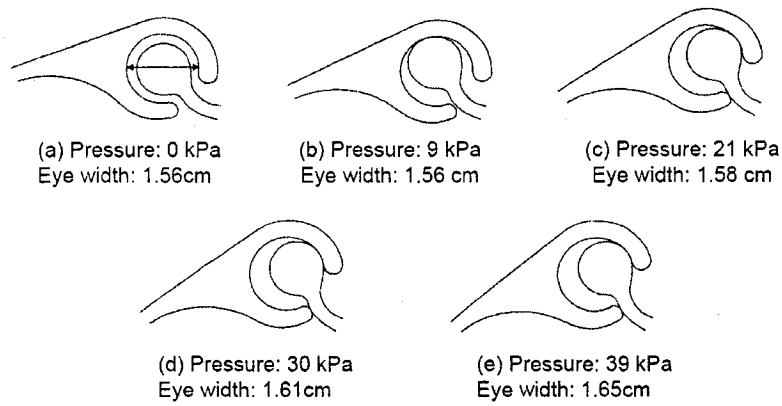

Figure 6.9: Deformation of the ball in socket connection

Figure 6.10 illustrates the maximum tensile and shear stresses at ball in socket connection when the pressure reached 40 kPa and their locations. The ultimate stresses of the eye connection were supposed to be the same as of the web because of the presence of a CFM mat in the inner surface of the eye connection (Figure 1.2). At 40 kPa, the stresses in the connection remained largely under their ultimate stresses. Therefore, the applied load was not likely going to cause connection failure at 40 kPa which was consistent with the experiments, where no joint failure was observed.

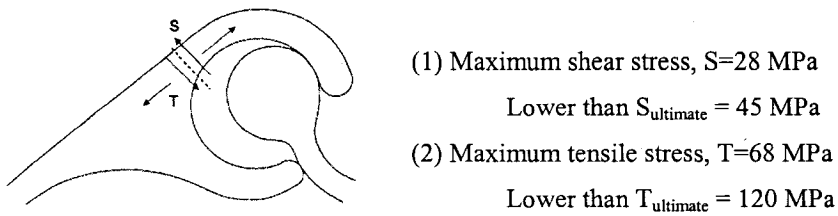

Figure 6.10: Critical stress in the ball in socket connection at 40 kPa

Figures 6.9 and 6.10 proved that the perfect pin-eye connection between the pin and eye joints used in the shell-connection model was not perfectly correct; from 20 kPa, the rotation became restrained. However, the effects of the differences of the two models were so small (Figures 6.5 and 6.7) that the shell-connection model seemed still largely sufficient to simulate the sheet pile panel at 40 kPa: detailing of the connections did not seem to be critical for the pre-buckling of the connected panel.

6.3 Bifurcation loads and buckling modes

At the end of the pre-buckling study, the tangent stiffness matrix of the structure had become singular. The traditional way of studying this singularity, i.e. buckling phenomenon, was applying a linear perturbation procedure to the panel usually called eigenvalue buckling prediction (Chapter 5). A buckling extraction calculation, step 2 of Figure 5.2, was performed on the deformed base state of the panel at 40kPa for each configuration and each model. The distributed transverse pressure created moments in every section of the panel. Compressive forces were created in the eye/pin flanges. Because the neutral axis was very close to the main flange (Figure 6.7), the web was mainly in compression. Coincidently, the two compressive plates buckled at the same pressure.

6.3.1 Results for the single panel

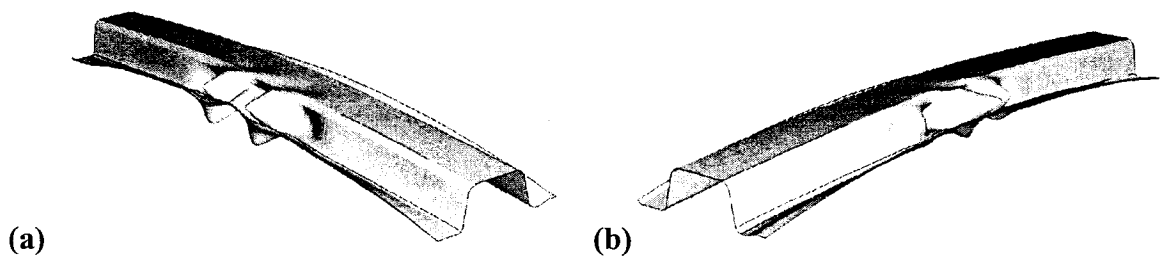

(a) (b)

Figure 6.11 First two buckling mode shapes of the single shell-connection model
(a) First mode on pin side, (b) Second mode on eye side

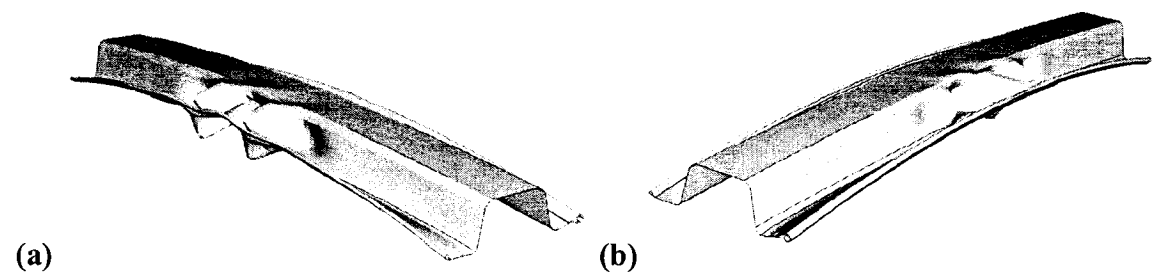

(a) (b)

Figure 6.12 First two buckling mode shapes of the single 3D-connection model
(a) First mode on pin side, (b) Second mode on eye side

Table 6.1: Buckling loads for the single panel

Model	Mode 1 (Pin side)	Mode 2 (Eye side)
Shell-connection	43kPa	45kPa
3D-connection	45kPa	47kPa

For the two models simulating the single panel configuration, similar results were found. The first mode consisted in combined waves on the pin flange and on the pin web, whereas the second one consisted in combined waves on the eye flange and on the eye web (Figure 6.11 and 6.12). It was found that the two buckling loads corresponding to the two modes were also closely spaced in Table 6.1 with less than 5% difference between the two first modes in each model; therefore it was impossible to predict with certainty which side would buckle first. Experiment results showed that buckling could happen on either side (Shanmugan, 2004). The small difference on the buckling load between the two models could be attributed to the different modelling of the connections. However, the difference remained quite negligible by only 5%.

6.3.2 Results for the connected panel

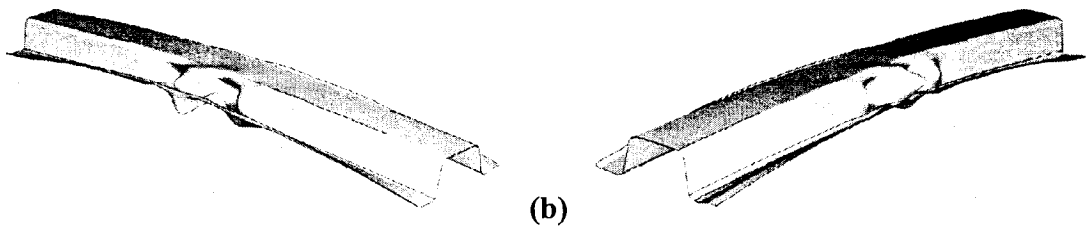

(a) (b)

Figure 6.13 First two buckling mode shapes of the connected shell-connection model (a) Right: First mode on pin side (b) Left: Second mode on eye side

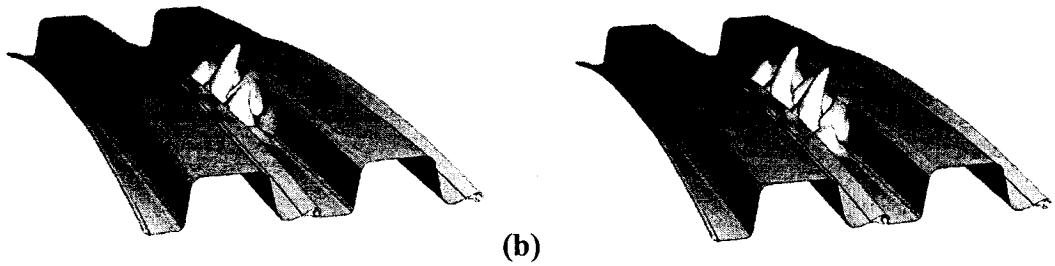

(a) (b)

Figure 6.14 First two buckling mode shapes of the connected 3D-connection model (a) Right: First mode on pin side (b) Left: Second mode on pin side

Table 6.2: Buckling loads for the connected panel

Model	Mode 1	Mode 2
Shell-connection	43kPa	44kPa
3D-connection	42kPa	43kPa

As regard to the shell-connection model, very similar results to the single panel configuration were found: the first mode consisted in combined waves on the pin side and the second one on the eye side (Figure 6.13). The first two buckling loads were also found fairly close (Table 6.2). For the 3D-connection model with contact formulation, the two first modes consisted in combined buckling of pin flange/pin web but with different numbers of waves. Buckling mode in an eye side appeared in further modes. The corresponding buckling loads were found very close in the two models.

6.3.3 General discussion

The results of the buckling study were quite similar for the four different models: the buckling loads were all between 42 kPa and 47 kPa. The buckling mode shapes were all equivalent thus confirming that the single and connected panels had very similar buckling behaviours. In experiments (Shanmugan, 2004), the buckling pressure of the single panels was found 15% larger than for the connected panels (Table 2.1), difference which was not obtained with FEM. A possible explanation could come from the boundary conditions enforced to the single panel: friction with the steel frame was ignored whereas it could have more influence on the single panel configuration than on the connected one.

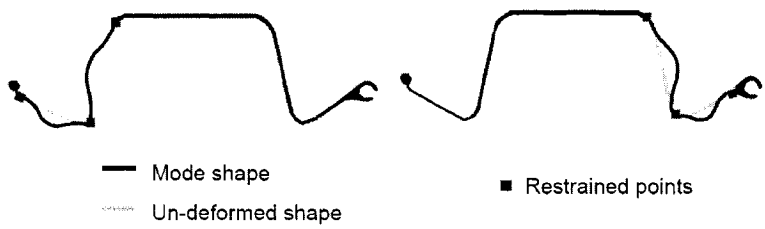

Fig 6.15: Schematic view of the modes, Mode 1 (left) and Mode 2(right)

The two modes of Figure 6.15 were of interest because their respective buckling pressures were very close. In the buckling process, eye and pin connections acted as restrained end

conditions for flanges: because they were a lot thicker than the pin/eye flanges (see Figure 4.1), the connections did not participate in the buckling wave. The junction ends (web/flanges) played a similar role: the junctions between webs and pin/eye/main flanges were restrained end conditions for the adjacent plates.

As seen in Chapter 2, predicting analytically the buckling load of a thin-walled structure requires knowledge of the restraints between the different plates and of the equation governing the relation between axial stresses in compressive plates and external loads on the structure. In order to find if the buckling load of the standard position panel could be predicted with such tools, analytical and numerical axial stress distributions were compared in the compressive plates just before buckling. Figures 6.16 to 6.19 give the axial stress distributions in the four plates of mid-section (Pin web, Eye web, Pin flange and Eye flange) at 40 kPa, using the Shell-connection model in connected configuration (the 3D connection model would give similar results). The same stress distribution was calculated analytically at a pressure of 40 kPa and added to the Figures 6.16 to 6.19. The following classic assumptions were used for the analytical calculation:

(1) Plane section remains plane after the panel is loaded. The cross section shape will not change as the panel deflected in bending. This assumption is commonly used in linear beam theory (Timoshenko).

(2) The classic beam theory Equation (6.2) is used to calculate the axial stress distribution, where: M is the moment in the section at mid-span, L the span, q the transverse load, $(EI)_{section}$ the flexural rigidity of the section, E_{11} the longitudinal modulus of the location where the axial stress is calculated and $y_{location}$ the distance from the location of stress to the neutral axis.

$$\sigma = \frac{M.y_{location}}{(EI)_{section}} E_{11-location} \quad \text{Where } M = \frac{q.L^2}{8} \tag{6.2}$$

(3) The initial unstressed position of the neutral axis was calculated using transformed section method. It was positioned at about 47mm from the main flange. This was found consistent with Figure 6.7-2 where the neutral axis was found about half way between strain locations 2-3 and 2-4. Using the first assumption, this position was supposed to remain unchanged as the pressure increased.

(4) The flexural rigidity was determined using multi-span test method (Giroux, 2000), and $(EI)_{section}$ = 206 kN.m^2. Based on the first assumption, this value was supposed to be constant as the pressure increased.

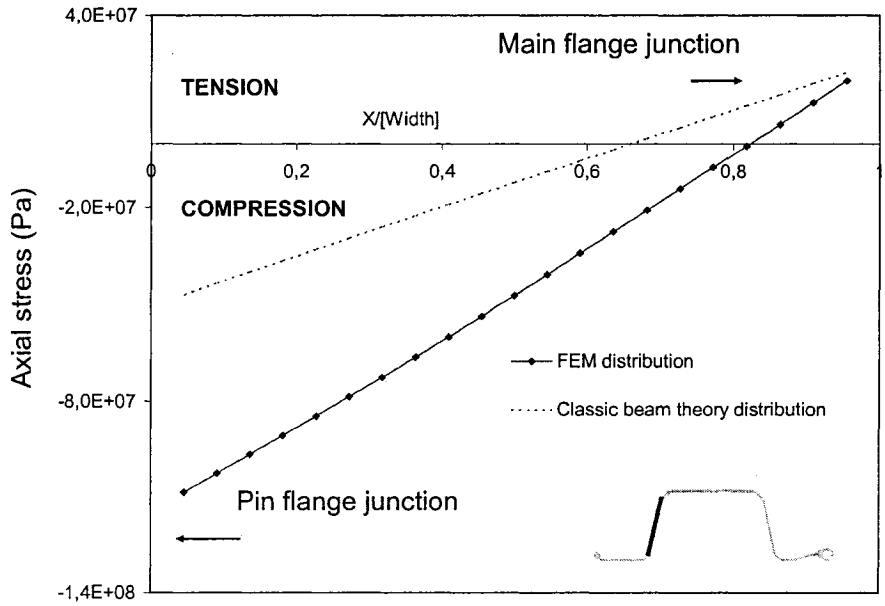

Fig 6.16: Axial Stress distribution in the pin web just before buckling (40kPa) (Shell-connection model in connected configuration)

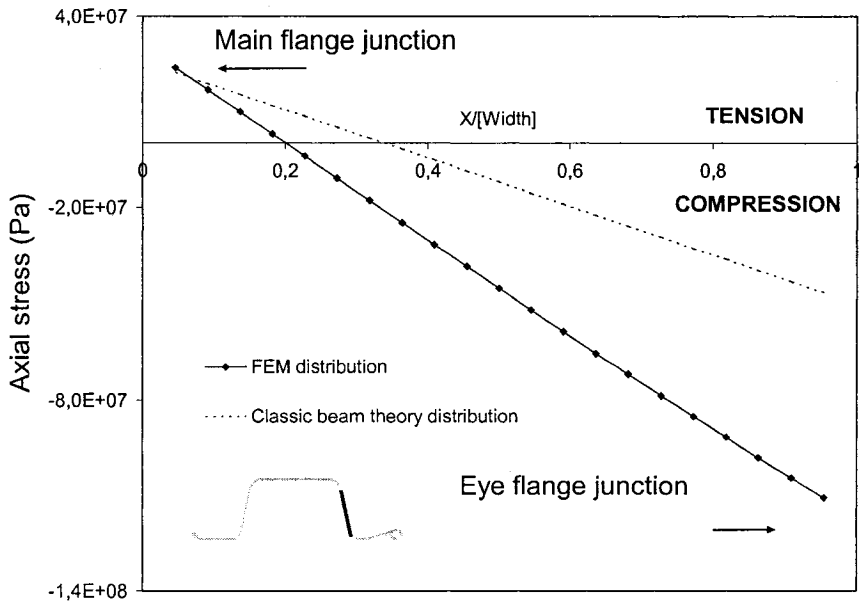

Fig 6.17: Axial Stress distribution in the eye web just before buckling (40kPa) (Shell-connection model in connected configuration)

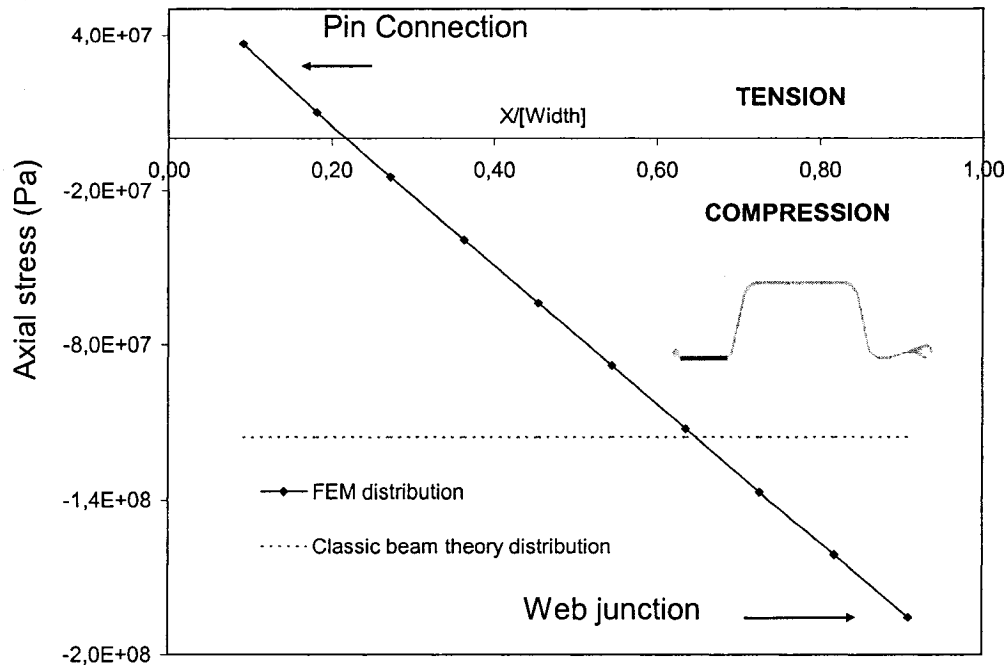

Fig 6.18: Axial Stress distribution in the pin flange just before buckling (40kPa) (Shell-connection model in connected configuration)

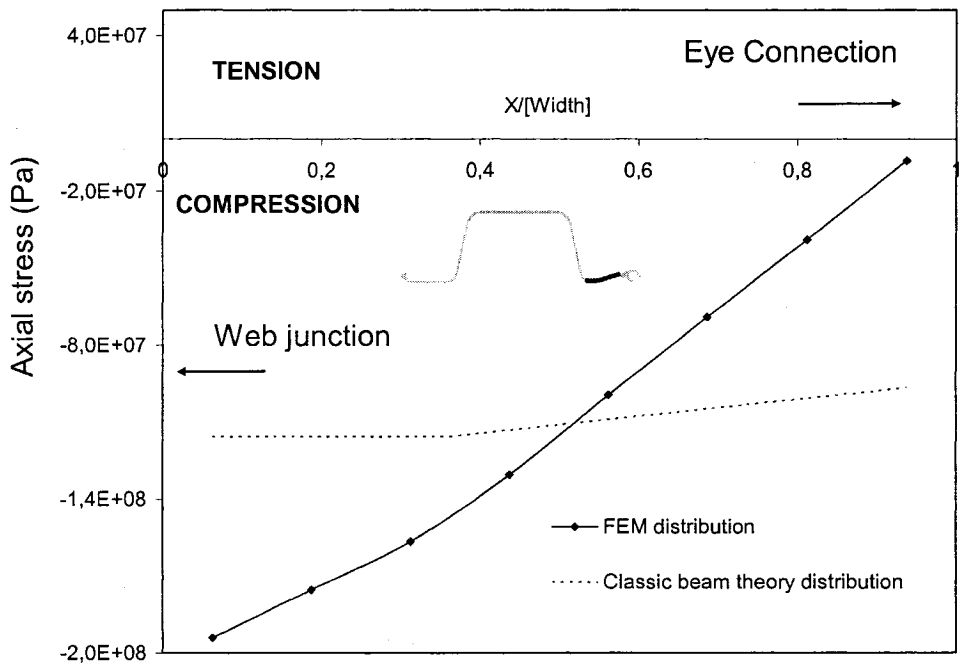

Fig 6.19: Axial Stress distribution in the eye flange just before buckling (40kPa) (Shell-connection model in connected configuration)

The two FEM curves in Figures 6.16 and 6.17 for the two webs showed very similar results: the same neutral axis position (80% of web in compression), same linear distribution and same stress values. At a pressure of 40 kPa, which was near the ultimate experimental failure, the stress distribution was still symmetric. The two FEM curves for the pin and eye flanges (Figure 6.18 and 6.19) were also very comparable. This similarity explained why buckling could happen at either pin or eye side without preference in experiments.

The numerical and analytical results were compared with Figure 6.16 to 6.19 and it appeared that the results were completely different. The analytical approach did not take into account the shift of the neutral axis towards the main flange and the flexural rigidity reduction due to the uplift movement of the two compressive flanges. These inaccurate assumptions made it difficult to predict the stress distribution using Equation (6.2). In eye and pin flanges, Equation (6.2) could only predict a constant compressive stress, whereas the FEM results showed an almost linearly distributed axial stress. With the axial stress calculated with Equation (6.2), it would be difficult to predict with accuracy the buckling load of the sheet pile panel in standard position (Chen, 2005). For comparison, the buckling load of a steel plate with fixed boundary conditions and subjected to linear axial stress is almost two times larger than if the axial stress was uniformly distributed (for the same average stress). It would be possible to use Equation (6.2) if shifted neutral axis position and the reduced $(EI)_R$ could be experimentally determined (Chen, 2005). However, the need of experimental results to predict the axial stress in the compressive flange showed the difficulty of giving an explicit design equation for the buckling of the standard position panel. This buckling analysis showed the importance of including nonlinear deformation in the buckling study.

Consequently, Figure 6.16 to 6.19 demonstrated that an all-analytical approach was inappropriate to predict the buckling of the standard position panel. More generally, when important non-linear deformation of the section occurs (which is often the case in bending of FRP structure where the transverse rigidity is small), the Finite Element approach is the best tool for buckling calculation.

6.4 Post-buckling behaviour of the sheet pile panel at standard position

In order to simplify the study, and to reduce the number of case, only the shell-connection connected panel was considered for the following study. This choice was made because very similar results were found when using the shell-connection and 3D-connection models and the connected and single configurations in pre-buckling and buckling calculations (See section 6.1 to 6.3).

To investigate the post-buckling behaviour of sheet pile after the critical load of 43 kPa, post-buckling analysis was performed. As shown in Chapter 4, there is two ways to execute such calculations:

(1) Imperfection method: the initial perfect geometry was perturbed by the introduction of a superposition of the two first buckling modes found by the buckling calculation shown in Figure 6.13. Different levels of perturbation were tried: 1.0 mm, 0.5 mm and 0.3 mm; the value indicates the upper bound of the geometric imperfection added.

(2) Dynamic method: several loading rates were applied to the panel: 5 kPa/s, 2 kPa/s and 0.3 kPa/s. The last value was the loading rate used in the single and connected panel tests and could be used to obtain the quasi static post buckling curves. The dynamic loading was applied from 0 kPa to 60 kPa.

The six different calculations, three with imperfection and three with dynamic loading, gave very similar results; in each case, the same post buckling wave pattern appeared at the two junctions (web / pin flange and web / eye flange). The pin side always buckled first, followed by the eye side. Figure 6.20 demonstrates the deformed shape and the stress distribution in longitudinal direction (σ_{11}), transverse direction (σ_{22}), and in shear (σ_{12}) at pin flange and web junction.

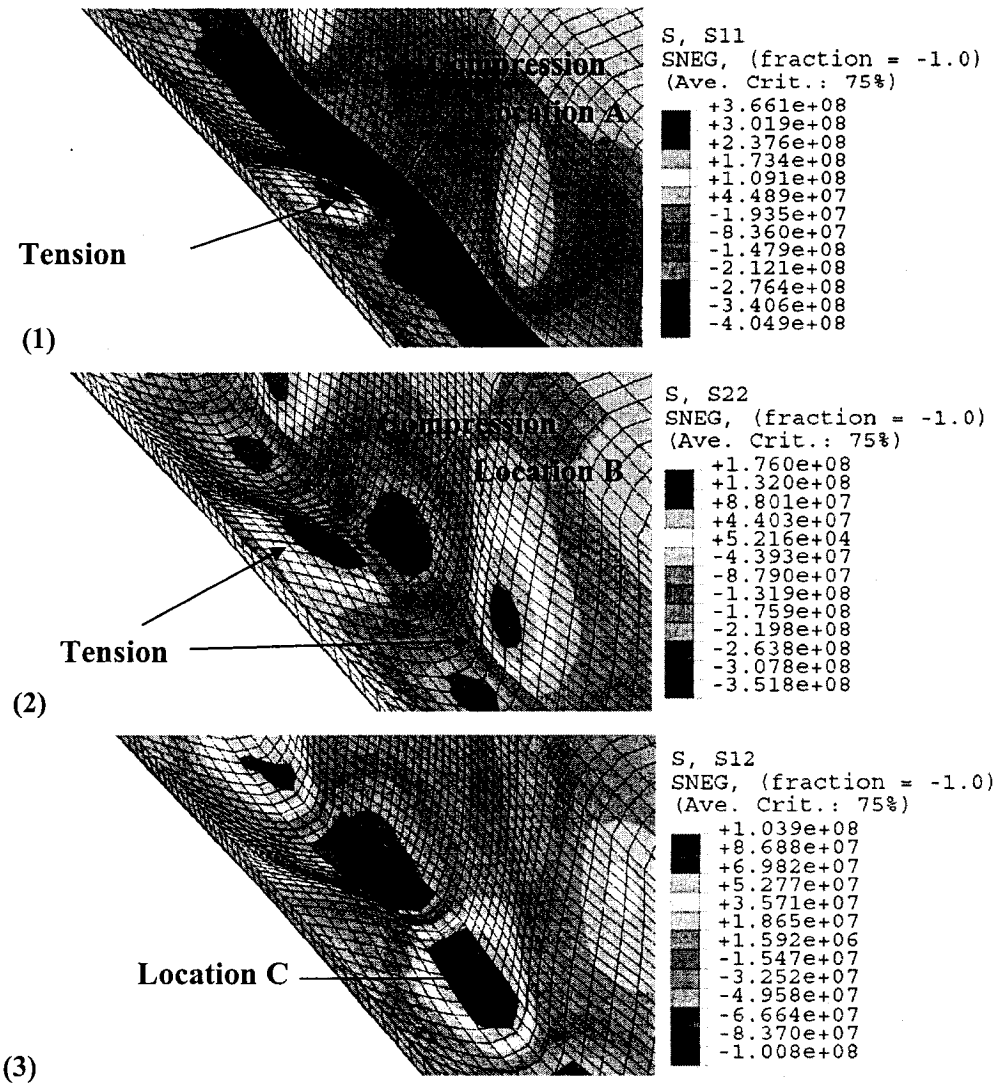

Fig 6.20: Stress distributions in the post-buckling waves at 45 kPa (imperfection: 0.5 mm); (1) σ_{11}, (2) σ_{22}, (3) σ_{12} (Unit: Pa)

High stress concentrations over small areas appeared after buckling which would lead to localized failure of the panel. In order to understand the mechanism of the failure of the panel, three different locations (Location A, B and C) were defined in Figure 6.20 and their maximum stresses using the six simulations (three with imperfection and three dynamics) are displayed in Figure 6.21. The parallel study of Figure 6.20 and 6.21 permitted to have a good appreciation of stress development in the standard position panel after buckling.

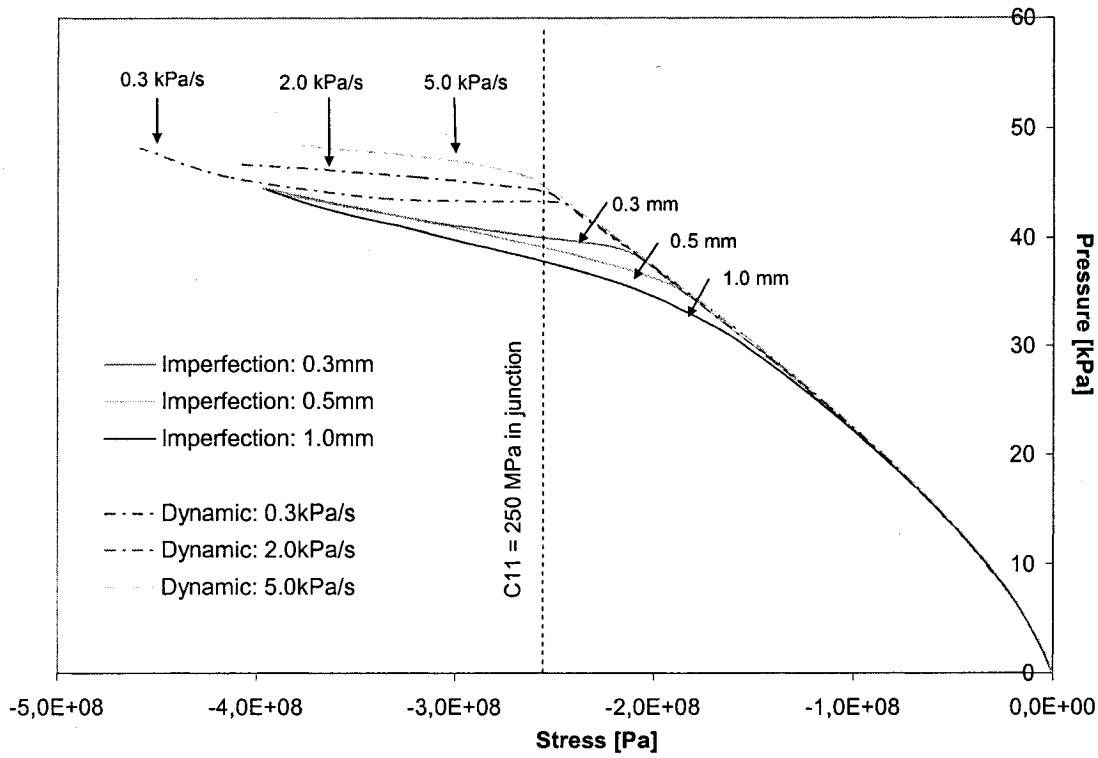

(a) σ_{11} in compression in the junction at location A

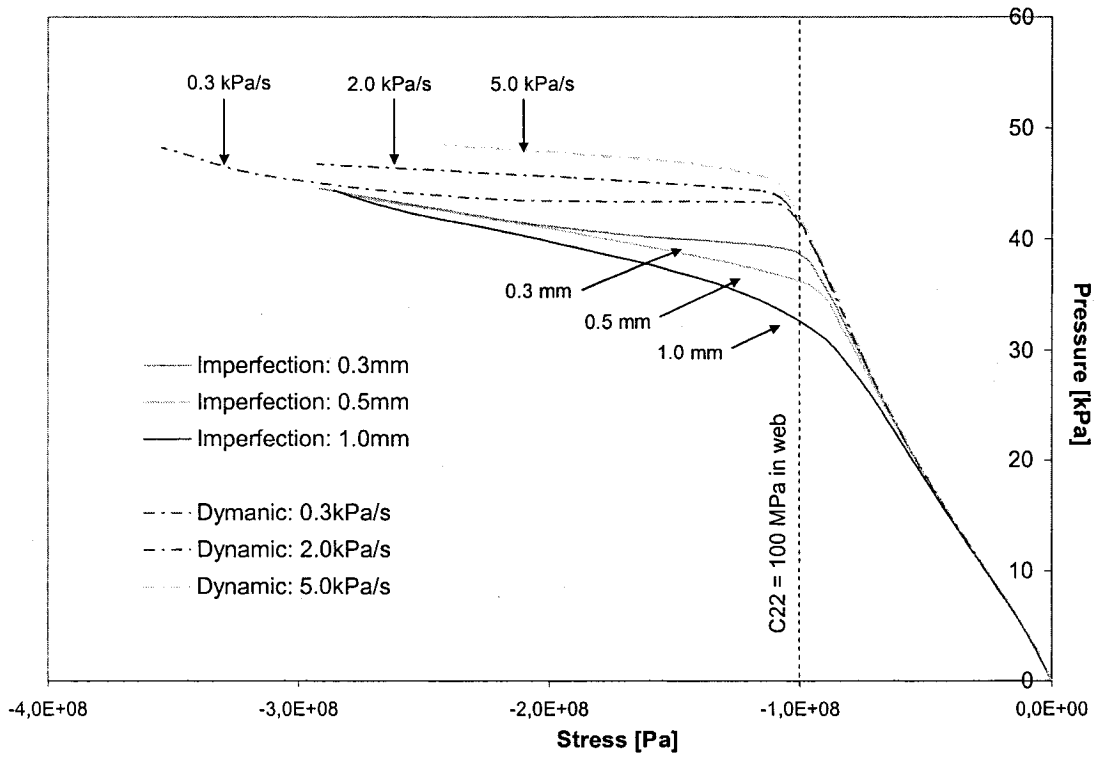

(b) σ_{22} in compression in web at location B

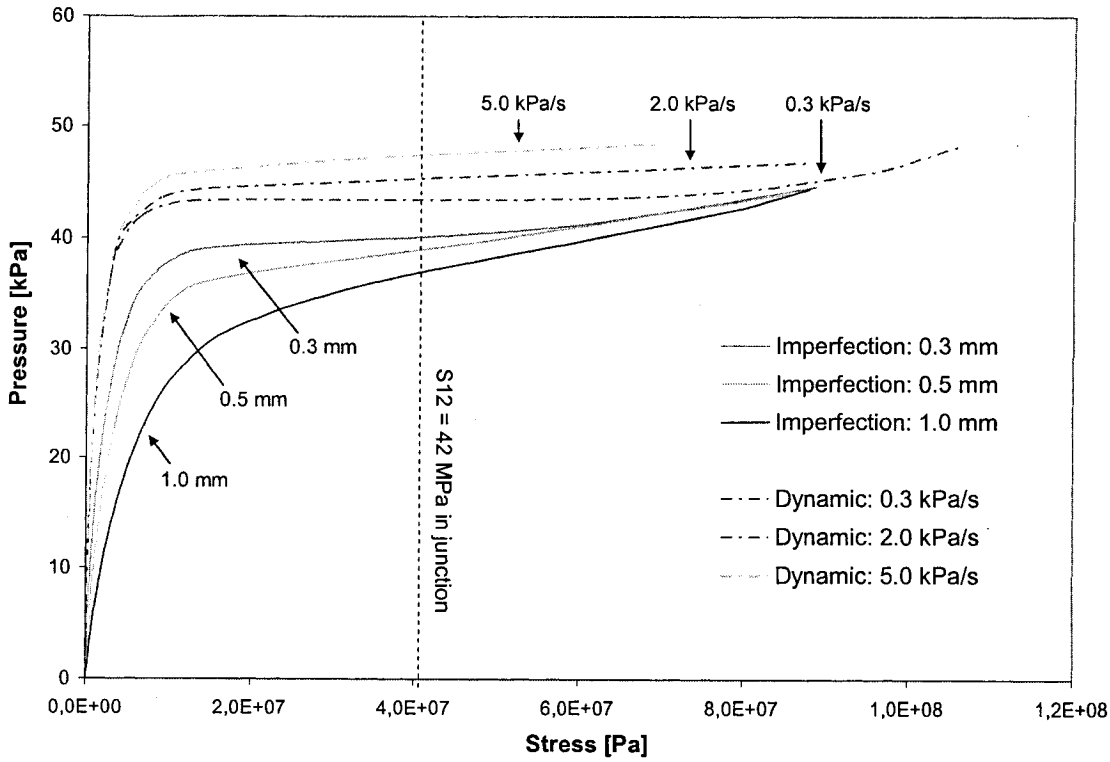

(c) σ_{12} in junction at Location C

Figure 6.21: Stress developments in the plates near junction

The pressure-stress curves of Figure 6.21 agreed very well for the two perturbation methods. It was possible to identify three different stages in the overall buckling behaviour of the sheet pile panels with imperfection or with dynamic loading.

(1) At beginning of loading, the panels with imperfection and dynamically loaded panels behaved exactly alike, indicating that the pre-buckling stage was not sensible to imperfection (if they remained in a reasonable range) or to the rate of loading (as long as it was not an impulse loading). The σ_{11} and σ_{22} pressure-stress curves followed exactly the perfect static equilibrium path curve.

(2) At buckling of the pin side, the six curves started to separate and showed distinct buckling behaviours. The more the amplitude of imperfection introduced in the panel, the sooner it buckled. Similarly, the larger the rate of loading, the later it buckled. The perfect static post-buckling curve was assumed to lie between the 0.3 kPa/s curves and the 0.3 mm imperfect curves.

(3) After buckling, the sensitivity to imperfection or dynamic loading of the panel disappeared, which is typical of post-buckling of plates, and the curves converged. The transition to the post-buckling stage consisted of a very brutal change of the slope of the pressure-stress curves. In Figure 6.21, for the 0.3 kPa/s simulation, from 43 kPa to 44kPa, the maximum value of σ_{11} at location A was multiplied by 1.5, σ_{22} at location B by 2 and σ_{12} by 8 at location C, identical brutal change were monitored for the five other simulations. This brutal increase of the stresses near the junction did not permit the standard position panel to exhibit post-buckling load capacity.

6.5 Failure of the standard panel

In Figure 6.21, the ultimate values for each stress obtained in Chapter 3 are also shown. In order to find which location failed first, the maximum stress criterion was used. Table 6.3 indicates the pressure to which the criterion was reached at each location. This pressure did not take into account mixed mode of failure. For example, in Figure 6.21-a, the compressive longitudinal stress at location A of the 0.3 kPa/s simulation reached C_{11}=250 MPa at 43 kPa.

Table 6.3: Exceeding pressures based on Maximum stress criterion

Simulation	σ_{11} failure (Location A)	σ_{22} failure (Location B)	σ_{12} failure (Location C)
Imperfection: 0.3mm	40 kPa	**39 kPa**	40 kPa
Dynamic: 0.3 kPa/s	43 kPa	**41kPa**	43 kPa

Rigorously, according to the maximum stress criterion, the standard position panel was predicted to fail at a pressure 41 kPa due to excessive transverse compressive stress in the web at location B using the dynamic 0.3 kPa/s simulation. As regard to the imperfect panel with 0.3 mm of perturbation, failure was of same mode, at same location but at 39 kPa. The Tsai Hill criterion is usually more appropriate to take into account failure due to the interaction of the three main stresses. The Tsai Hill criterion was computed with the FEM program (Automatic computation with option Fail Stress) for every shell element constituting the perfect dynamic panel. Table 6.4 gives the panel failure loads for the two

criteria. Slightly the same failure pressure was found. The element leading to failure was found to be the same for both criteria: it was the element at location B.

Table 6.4: Failure loads as a function of the criteria used (Dynamic, 0.3 kPa/s)

Criterion used	Failure load
Maximum stress theory	41kPa
Tsai Hill theory	40kPa

These two failure loads were consistent with the experimental failure: the experimental connected panels were found to fail between 35 kPa and 43 kPa. The values of the failure loads (Table 6.4) and of the buckling load (43 kPa) were so close that it was difficult to distinguish the two, suggesting that buckling initiation and failure occurred simultaneously. In other words, there was no apparent post-buckling region in FRP Panel in standard position, which was consistent with experiments.

Rigorously, the panel was predicted to fail from excessive transverse compressive stress in the web at location B. However, Table 6.3 shows that all ultimate stresses were reached within the same range of pressures, thus suggesting that either failure could occur; the failing pressures corresponding to the three stresses were so close that it was merely impossible to predict with certainty the failure mode (σ_{11}, σ_{22} or σ_{12}). This numerical result was confirmed by experiments. In the case of the experimental sheet pile panels at standard position, there were three distinct failure modes, (1) based on compressive failure of the pin or eye junction in longitudinal direction (C_{11}), (2) compressive failure in transverse direction (C_{22}) in the web and (3) in-plane shear failure of the junction (S_{12}). This classification was made possible by the comparison of the crack patterns with the stress distributions found in Figure 6.20.

In Figures 6.22 to 6.24, the left pictures correspond to the photographs of the failed experimental panels at the junction. On the right is the corresponding stress distribution: point failure was drawn with a star, major cracks in solid black line and minor cracks

(caused by additional progressive failure) in dashed line in order to amplify the correspondence.

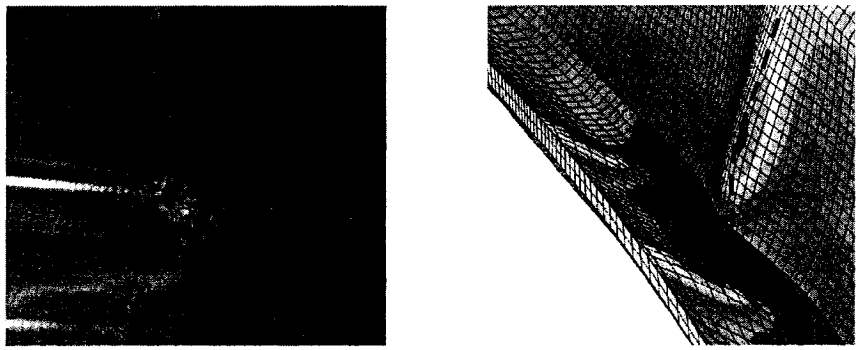

Fig 6.22: Local crushing of flange at junction due to excessive compressive σ_{11}

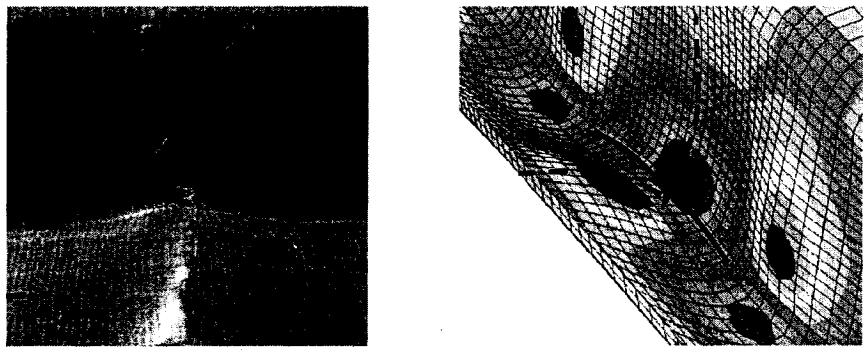

Fig 6.23: Local crushing of web near junction due to excessive compressive σ_{22}

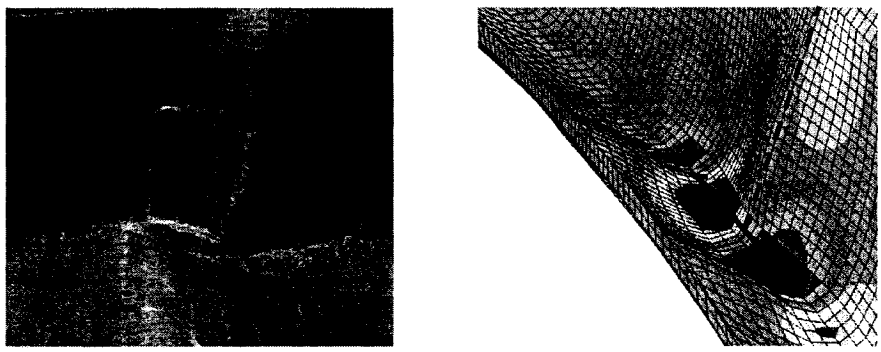

Fig 6.24: Local shear failure of junction due to excessive shear stress σ_{12}

In Figure 6.22, the composite failed due to a point failure (very localized crushing) at junction, which corresponded exactly to the location of maximum compressive stress σ_{11}. The crack in the junction was in transverse direction, therefore due to σ_{11} stress, and close observation showed material compressive failure, not tearing. This failure point was

accompanied with a crack thought the web, which corresponded to the buckling wave in the web.

In Figure 6.23, the failure mode was completely different. The failure pattern was composed of a point failure with a long crack along the junction. Two waves were visible: one coming out of the pin flange and one in the web with opposite direction, which corresponded exactly to the deformed shape calculated. The longitudinal crack corresponding to a σ_{22} failure was marked in the picture: in experiments, it was measured to be 147 mm long. This length was found very close to the width of the high transverse stress concentration zone developed between 41 kPa and 43 kPa near location B in Figure 6.25: the measured length was 140mm (5% difference with experimental crack length).

The cracks on Figure 6.24 were observed in two different panels. Contrary to the other failure modes, the two visible waves were shifted from one of the other along the junction. The two waves were curved towards each other. This anti-symmetry is characteristic of a shear failure. The main crack was located at junction between the two waves, exactly where the shear stress reached maximum.

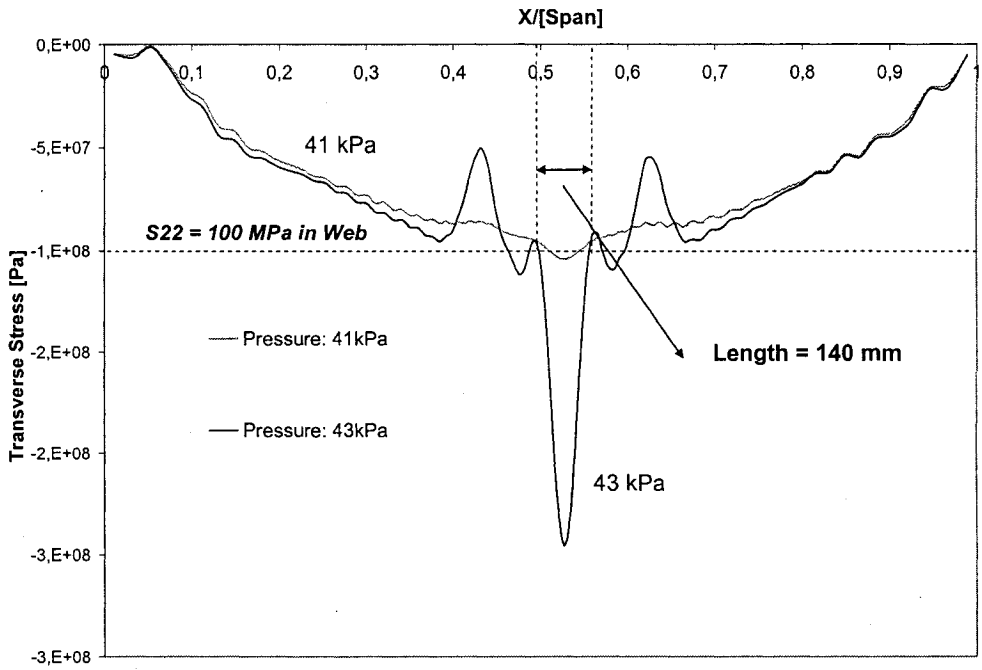

Figure 6.25: Transverse stress in web near junction along the span

Chapter 7: Finite Element Analysis of FRP Sheet Pile Panel in Reverse Position

The same calculation method presented in Chapter 6 was applied to sheet pile panel at reverse position. A parallel study permitted to point out the differences between the two configurations. Only the simplified shell-connection model was used for it was demonstrated that the simplified model yielded similar results as the 3D-connection model and demanded far less computational time. In section 7.1 to 7.4, the single reverse panel was analyzed and its results were compared with experimental data. The same four steps of Figure 5.2 were repeated. The connected reverse position panel, which was not experimented, was studied in section 7.5.

7.1 Non-linear, pre-buckling behaviour of the single reverse panel

The first step was to carry out a simple non-linear static calculation. The calculation stopped for convergence problem at a pressure of 24 kPa as a bifurcation loading. This was about half the buckling load carried out by the same panel but loaded at standard position. Presented in Figure 7.1 is the deformed shape of the reverse panel at 24 kPa, just before buckling initiation.

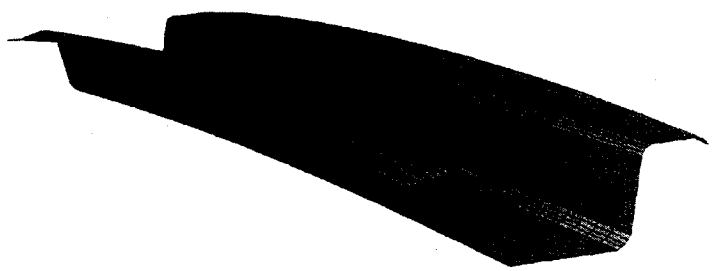

Figure.7.1: Deformed reverse position panel at 24kPa.

During the experiments, three strain gauges were placed on the three flanges at mid-section. The mid-point deflections of these three flanges were also measured. Figure 7.2 compares the deflection curves and the strains of numerical simulation with experiments. For the FEM strain curves, curvature effect due to longitudinal curvature was added using equation 6.1 in order to compute the effective strain on the top of the flanges.

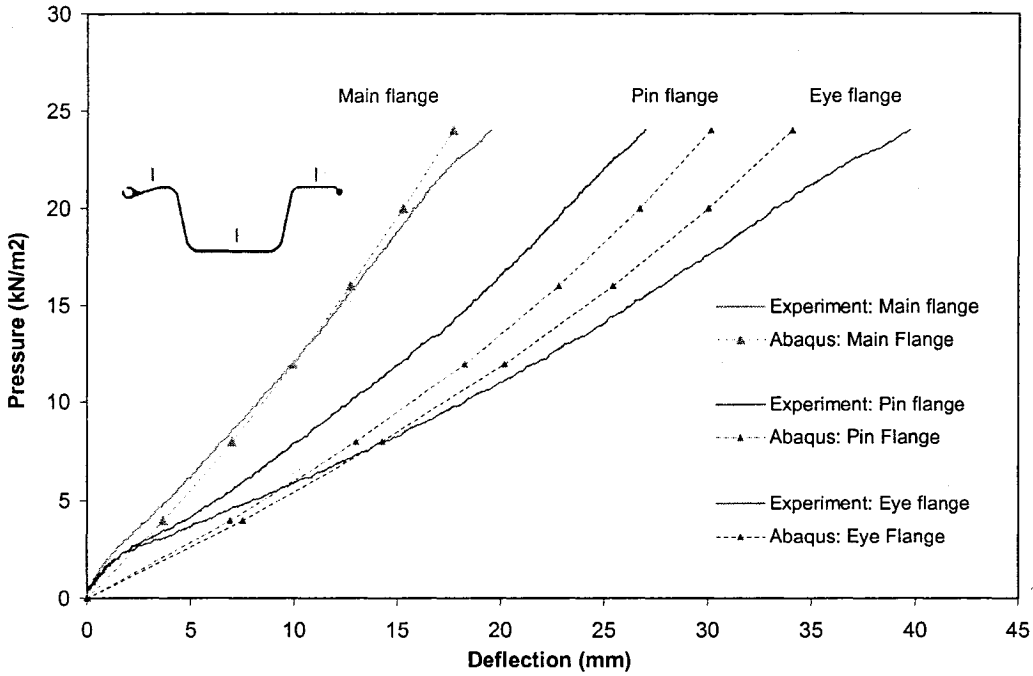

(a) Deflections in the reverse single panel

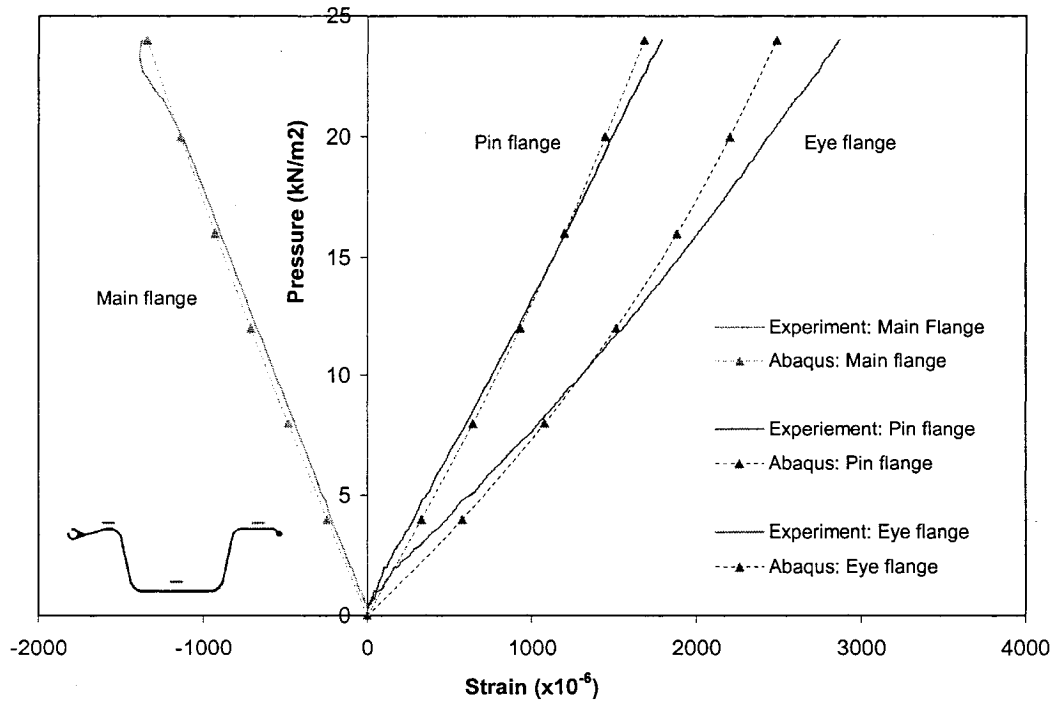

(b) Longitudinal strains in the reverse single panel

Fig 7.2: Comparison of pre-buckling deflections and strains in the reverse position panel

In Figure 7.2 (a), the finite element deflection in main flange agreed very well with experiment. The differences in deflections of the pin and eye flanges were significant between the experimental and numerical curves. The comparative results appeared to suggest that the relative displacement, or the twist, between the pin and eye flanges was smaller in FE simulation than in the experimental results. The calculated deflections of the pin/eye flanges were much closer to each other than what was obtained experimentally. The extra twist observed in the experiments could be explained by an uneven pressure that was distributed to the eye/pin flanges via the foam (see Figure 4.5). The numerical tensile strains compared very well with experiments in Figure 7.2 (b) in the three flanges.

It was interesting to notice that the numerical pressure-deflection and pressure-strain curves in the three flanges exhibited hardening behaviours. By comparing the pressure-deflection and pressure-strain curves of the two loading configurations (Figures 6.2, 6.4 and 7.2), it was noticed that the curves of the two configurations had opposite curvatures. In the standard position, the eye and pin flanges were moving towards the neutral axis under the action of a distributed pressure (opening of the section), therefore reducing the flexural stiffness, and leading to non-linear softening pressure-deflection and pressure-strain curves. In the reverse position, the mechanism was seen opposite: the two eye/pin flanges were pushed away from the neutral axis (closure of the section), which enhanced substantially the flexural rigidity of the reverse panel and resulted in a hardening response in both deflection and strain curves.

7.2 Bifurcation load and buckling mode

A buckling extraction procedure was performed on the deformed base state of the reversed panel at a pressure of 24kPa. The first two buckling modes and associated pressures are presented in Figure 7.3 and Table 7.1. The panel was flipped with compressive main flange on top to get a better view of the buckling mode.

In the reverse position, compressive forces were created in the main flange. It was expected that buckling would occur in the main flange.

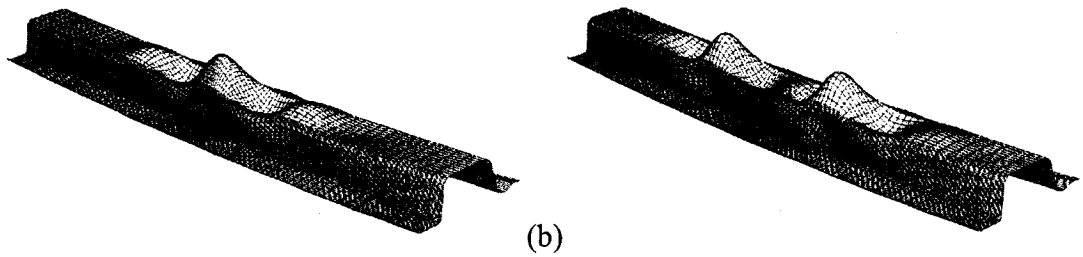

(a) (b)

Figure 7.3 First two buckling mode shapes of the single reverse model (a) First mode, (b) Second mode

Table 7.1: Buckling loads for the single reverse position panel

Mode number	Buckling load
Mode 1	25kPa
Mode 2	29kPa

The two first modes in Figure 7.3 consisted of buckling waves in the main flange. The only difference between the two modes was the number of half waves: five for the first mode and six for the second. Contrary to the standard position configuration where the two first buckling loads only differed by 4%, the two first buckling loads of the reverse panel (Table 7.1) differed by 15%. Consequently, only the first mode with less half waves was the one of interest.

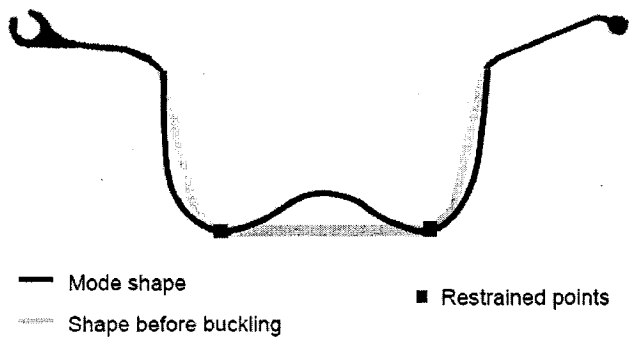

Fig 7.4: Schematic view of the main flange mode

Figure 7.4 shows the schematic view of the main flange buckling mode. The two web/main flange junctions acted as restraints for the calculation of the buckling load. Because the thickness of the main flange was 1.5 larger than the thickness of the webs, it was expected that the rotation restraints on the main flange were low.

Figure 7.5 shows the distribution of axial stress in the compressive main flange at mid span which will initiate buckling using FEM results and the Classic beam theory calculated distribution (same calculation as in section 6.3.3) at a pressure of 24kPa.

For the usual classic beam theory calculation, the section was supposed to remain un-deformed as it deflected in bending. The axial stresses at mid span in the top flange were calculated with the Equation (7.1).

$$\sigma = \frac{M.y}{(EI)_{section}} E_{11-main-flange} \quad \text{Where } M = \frac{q.L^2}{8} \tag{7.1}$$

Where: M is the moment in the section at mid-span, L is the span, q the transverse load, $(EI)_{section}$ the flexural rigidity of the section (equal to 206 kN.m^2, Giroux 2000), E_{11} the longitudinal modulus of the main flange and y the distance between the main flange and the neutral axis equal to 4.7 cm (Giroux 2000). The value of the flexural rigidity and the neutral axis position were experimentally determined using beam theory equation. Because it was supposed that the section remained un-deformed, those two values were supposed to remained constant as the pressure increased.

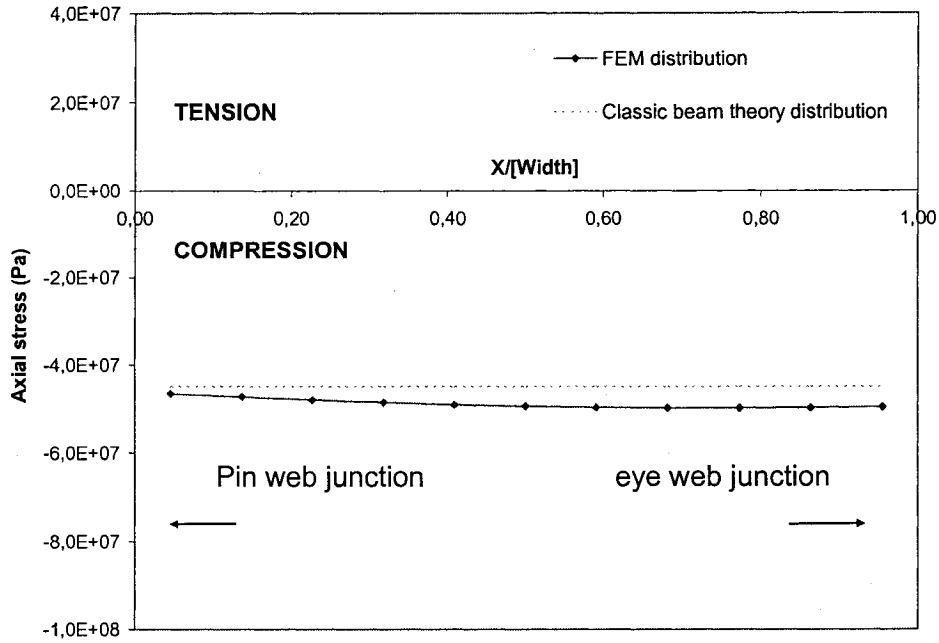

Figure 7.5: Distribution of longitudinal stresses in main flange before buckling initiation

Figure 7.5 shows a uniformly distributed axial stress in the main flange by both FEA and beam theory. Unlike the standard position panel, the classic beam theory seemed to agree well with numerical results. If the deformation of the section was considered, it would be necessary to take into account in equation (7.1): the increase of $(EI)_{section}$ (hardening response) and the shifting of the neutral axis towards the tensile flanges. However, it appeared that for the calculation of the longitudinal stresses in the main flange at 24 kPa, their effects were negligible.

As seen in Chapter 2, predicting analytically the buckling load of a thin-walled structure requires knowledge of the restraints between the different plates and of the equation governing the relation between axial stresses in compressive plates and external loads on the structure. Figure 7.5 proves that in the case of the reverse position panel, the flexural stress formula was efficient to relate the axial stress in the main flange to the loading. It was concluded that if the restraints between the webs and main flange were known, the buckling pressure of the reverse panel would be predicted with success with the buckling equation of a restrained compressive plate.

7.3 Post buckling behaviour of the sheet pile panel at reverse position

To obtain the post buckling behaviour of the reverse panel, the same two methods used with the standard configuration were adopted:

(1) Imperfection method: the initial perfect geometry was perturbed by the introduction of an imperfection with shape of the mode found in the eigenvalue extraction procedure (mode 1 of Figure 7.3). Amplitude of only 0.05 mm was used, which was the smallest value to trigger the post-buckling behaviour of the reverse position panel.

(2) Dynamic method: a small rate of loading of 0.3 kPa/s was applied to the numerical panel. This rate of loading was nearly the same as the one used in tests.

It was decided not to use other rates of loading or other amplitudes of imperfection, for only the quasi-static postbuckling curves were of interest. It is known that the effective quasi static behaviour was bounded by those two modified panels.

7.3.1 Comparison between numerical and experimental results

Unlike the standard panels, the reverse panels showed in experiments post-buckling load bearing capacity: the reverse panel was able to take load after buckling initiation. The post-buckling behaviour was manifested through complete pressure-deflection and pressure-strain curves for the three flanges. Figure 7.6 shows the complete results for strains and deflections for the FEM dynamic perfect panel, FEM static imperfect panel and the experimentally tested panel.

Concerning the pin and eye flanges, the differences between the deflection and strain curves of the imperfect panel and the dynamic panel were very small throughout the calculation, thus confirming that the effects of the imperfection and the rate of loading chosen were not significant. The comparative results of the experimental and numerical curves showed that the results were comparable for the pin flange but less agreeable for the eye flange. As said before, the numerical panel did not twist as seen in the experimental panels.

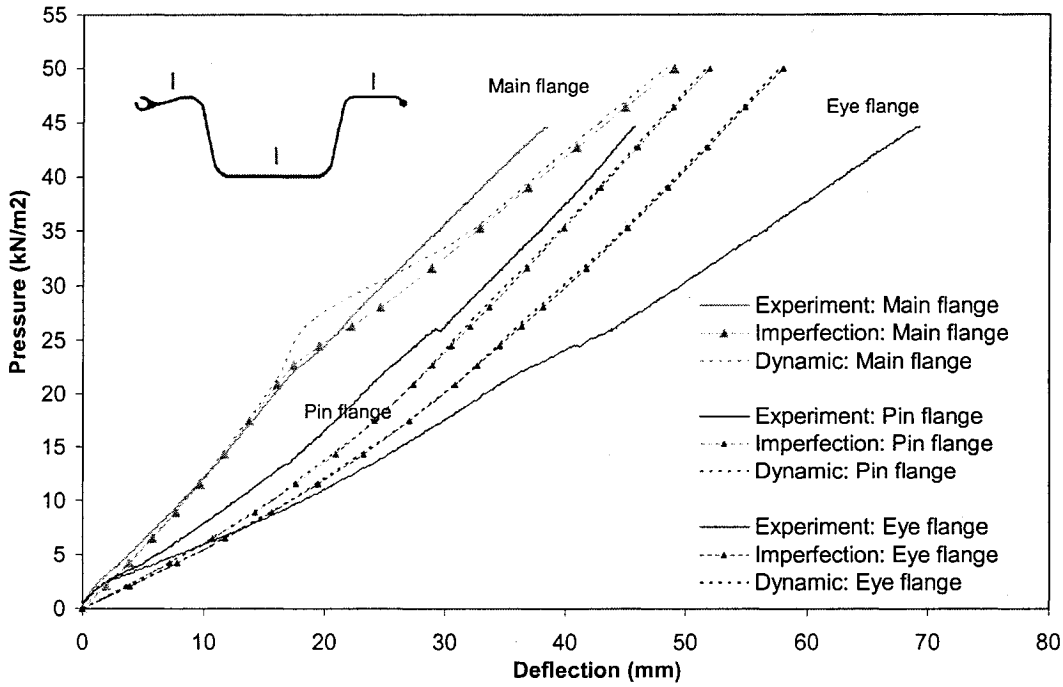

(a) Deflection in the reverse single panel (Pre-buckling and Post-buckling)

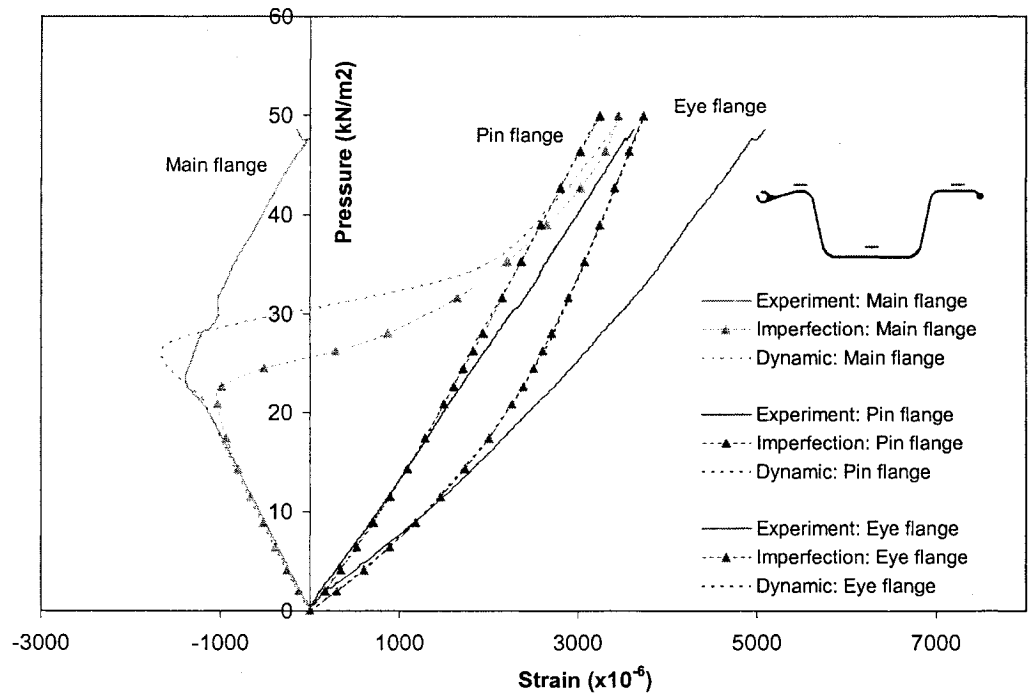

(b) Longitudinal strains in the reverse single panel (Pre-buckling and Post-buckling)

Fig 7.6: Comparative of post-buckling deflections and strains for the reverse position panel

As regard to the main flange plate which was subjected to compression, the static-imperfect, dynamic-perfect and experimental strain and deflection curves coincided perfectly before the bifurcation load: as for the standard position panel, the pre-buckling behaviour was not sensible to imperfection or to rate of loading. At a critical pressure, decease in the compressive strain in the main flange with increasing load was observed: this snap back was indicative of the sign change in strain from compression to tension (Figure7.6 (b)). This critical pressure or buckling load and the snap back were found different in the two perturbation methods used. The critical numerical pressures are displayed in Table 7.2. The two values obtained from the perturbation methods placed a boundary on the perfect static bifurcation load calculated in section 7.2. The numerical values of the buckling load were consistent with the experimental buckling; the experimental reverse panel was found to buckle between 23 kPa and 27 kPa.

Table 7.2: Bifurcation loadings as a function of the imperfection or rate of loading

Imperfect static panel (Figure 7.6)	**Perfect static panel (Section 7.2)**	**Perfect dynamic panel (Figure 7.6)**
23 kPa	25 kPa	27 kPa

After the bifurcation transition, the static-imperfect and dynamic-perfect main flange curves converged: the post-buckling curves were found to be not sensitive to imperfection and dynamic loading which is typical of buckling of plates. The numerical main flange strains deviated completely from the experimental strain: it was found that the post-buckling value of the main flange strain was extremely sensitive to the placement of the gauge. The numerical strain location was at the exact center of the buckling wave whereas in experiments, the same strain location was always found shifted from the center of the wave.

As regard to the deflection of the main flange in Figure 7.6 (a), a sudden change of the deflection slope was monitored at bifurcation in the main flange due to buckling. This change of slope was found larger in the numerical panel than in the experimental panel.

7.3.2 Stresses distribution

Figure 7.7 summarizes the stress distribution (σ_{11}, σ_{22}, σ_{12}) after buckling of the main flange.

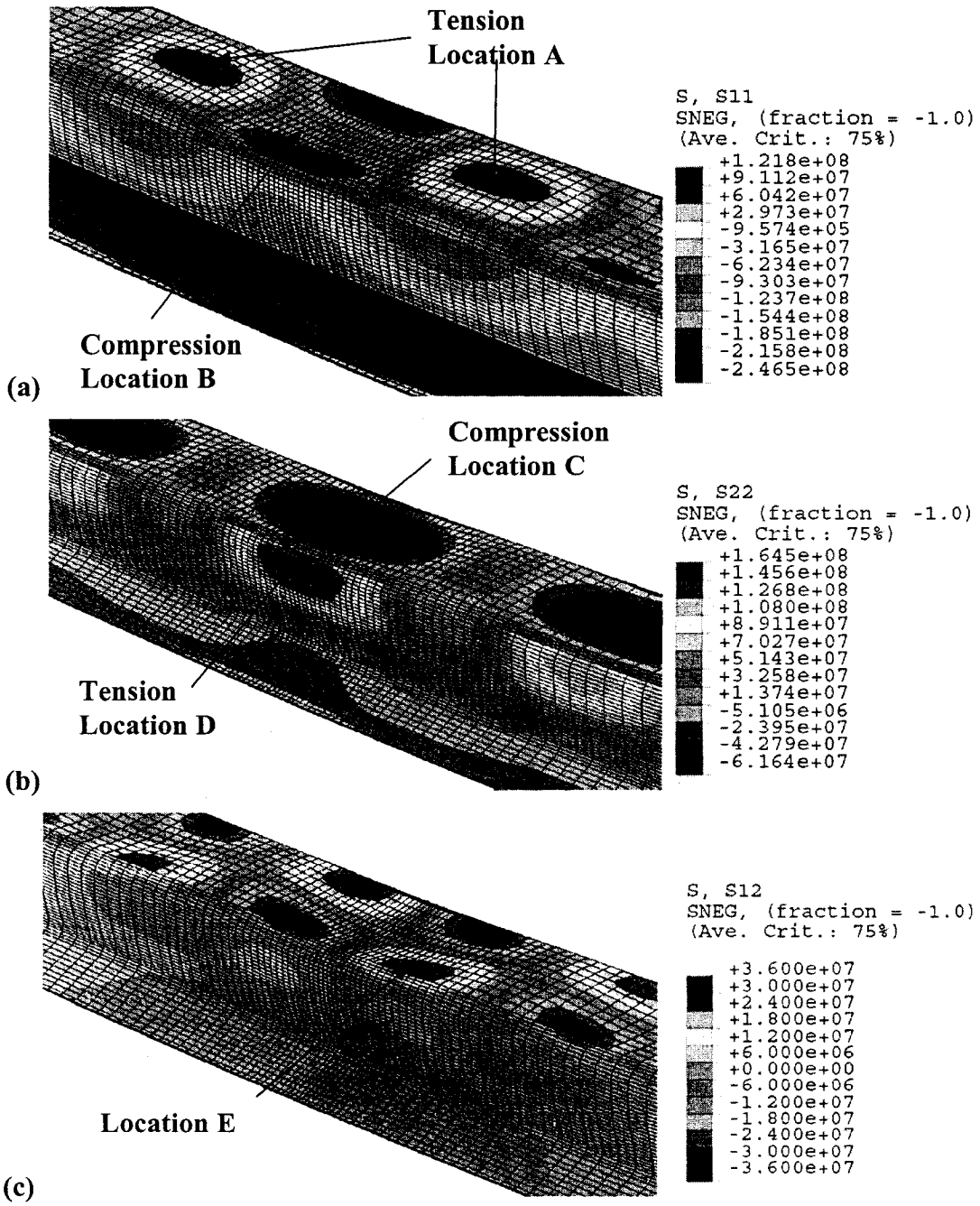

Fig 7.7: Stresses distribution in the post-buckling waves at 50kPa (Imperfection: 0.05 mm)

(a) σ_{11}, (b) σ_{22}, (c) σ_{12} Unit: Pa

Five different locations were defined in Figure 7.7 which corresponded to high stress concentration zones. Figure 7.8 shows the evolution of the stresses from 0 kPa to 60 kPa at locations A, B, C, D and E using the static imperfect panel and the perfect dynamic panel. The pressure-stress curves agreed very well for the two perturbation methods. The parallel study of Figures 7.7 and 7.8 permitted to have a good appreciation of stress evolution in the reverse position panel after buckling.

Before buckling, the compressive axial stress in the main flange was uniformly distributed along the width (Figure 7.5). After buckling, tensile stress appeared on the positive waves (Location A) because of the length extension of the fibres and high compressive zones were developed near the two web junctions at negative waves at Location B as shown in Figure 7.7 (a). In Figure 7.8 (a), the evolutions of the axial stresses at those two locations are displayed. Initially, the two stresses were both in compression and had parallel evolution, thus confirming that longitudinal stress was evenly distributed along the width of the main flange. This uniform distribution changed radically at buckling: At Location A, σ_{11} became tensile and at location B, the pressure-stress slope rapidly increased to form a high compressive zone near the web junctions. After buckling, the neutral plane in the web had the shape of a sinusoid along the span, as visible in Figure 7.7 (a).

Figure 7.7 (b) and Figure 7.8 (b) shows the transverse stress distribution. Before buckling, transverse stress at location C (middle section of main flange) was very small. After buckling, σ_{22} rapidly grew to compression in each negative wave of the main flange. In the same section, high tensile stresses were created in the web near the main flange junctions (Location D) due to tearing effect of the negative wave.

Figure 7.8 (c) shows that shear stress was initially very low in the reverse panel. After buckling of the main flange, high shear zone were created in main flange, Location E in Figure 7.7 (c), where curvature of the main flange changed, i.e. between negative and positive waves.

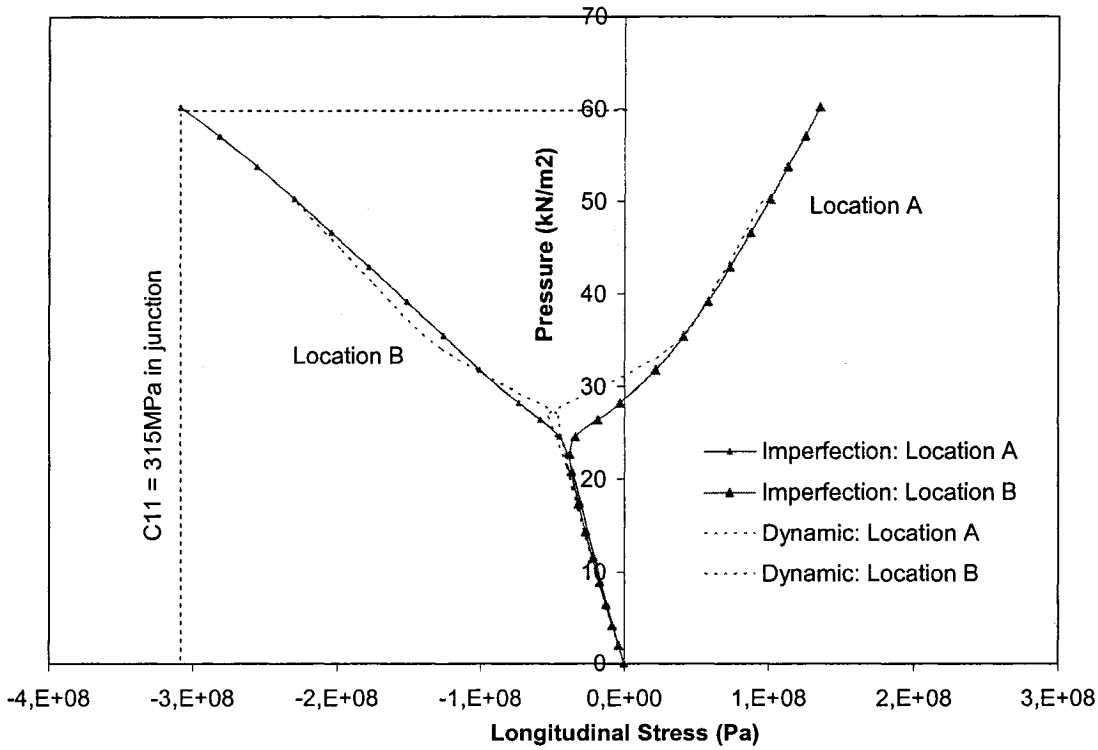

(a) σ_{11} evolution at location A and B

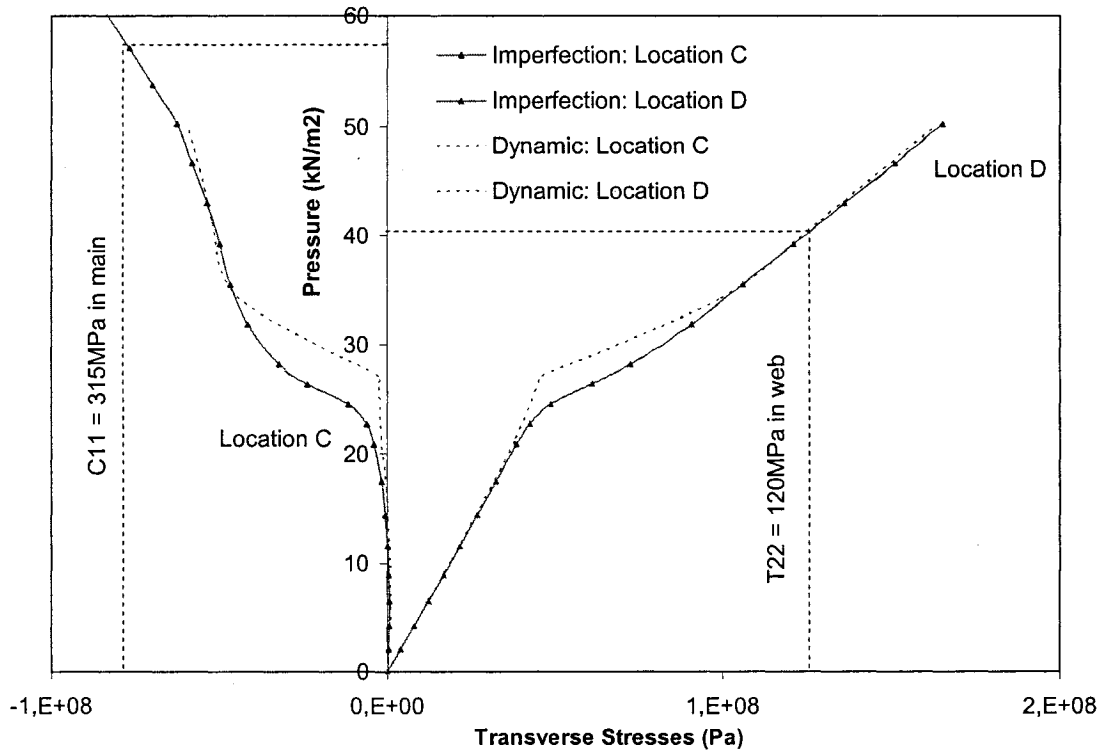

(b) σ_{22} evolution at location C and D

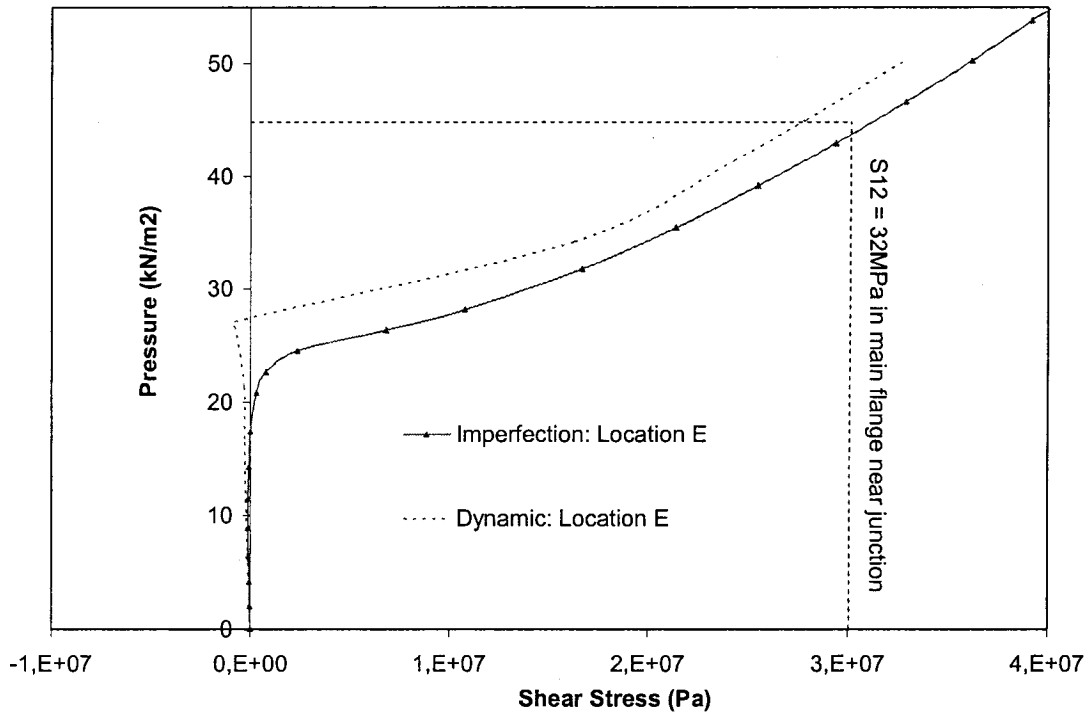

(c) σ_{12} evolution at location E

Fig 7.8: Critical stress evolutions in the reverse position panel

In Figure 7.8, the ultimate stress values for each stress are also shown. As seen in Chapter 3, these values were a function of the location and of the compressive or tensile nature of the stress. Concerning the shear ultimate strength of the junction (Location E: interface between the junction and the main flange), the average value of S_{12} of the web and of S_{12} of the main flange was chosen.

Those strength indicators permitted to study the failure of the reverse panel. Contrary to the standard position panel, it was observed in Figure 7.8 that all ultimate values were exceeded during the post-buckling stage, confirming that the reverse position panel had post-buckling load bearing capacity, which was seen coherent with experiments where the failure load was found almost twice as large as the buckling load (Table 2.2).

7.4 Failure of the reverse panel

7.4.1 Experimental failure

In the experiments, the reversed beam failed at a pressure loading between 44kPa and 48kPa. Contrary to the standard panel, only one failure mode was obtained. It is shown in Figure 7.9. Experimentally, the buckling of the main flange under compression was followed by separation of the main flange from the webs initiating tearing failure near the two junctions. Four main cracks orientated in the longitudinal direction were all located at mid-span of the panel (the cracks are marked in Figure 7.9):

Crack 1: In the pin web near junction with the main flange

Crack 2: In the main flange near junction with pin web

Crack 3: In the eye web near junction with the main flange

Crack 4: In the main flange near junction with eye web

These four cracks were usually accompanied with transverse cracks through the webs.

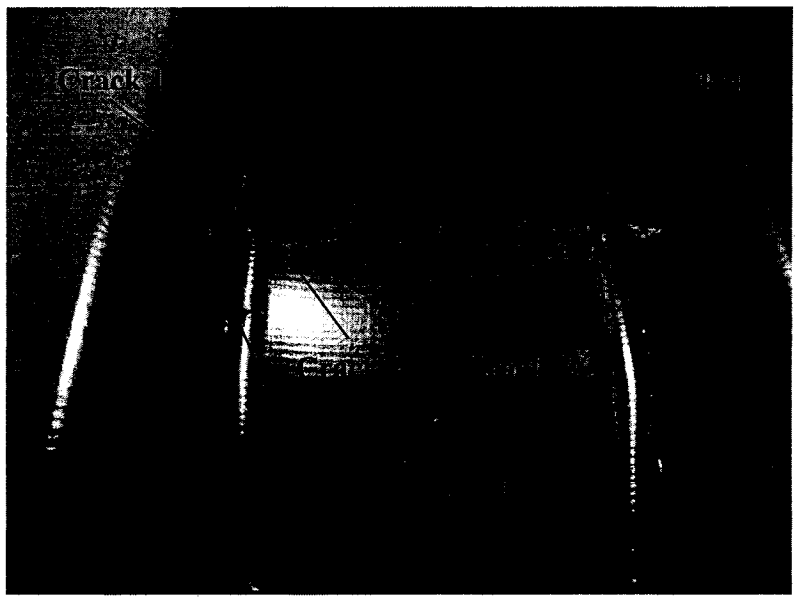

Figure 7.9: Cracks in reverse panel at failure

The length of the longitudinal cracks was measured on the failed beam. The average value was 254mm. In the two experimental panels, it was observed that this length could be related to the length of one buckling half-wave in the main flange.

7.4.2 Numerical failure

In Figure 7.8, the evolutions of the stresses at the critical locations (A, B, C, D and E) are displayed along with the ultimate stresses of the composite at the same location. In order to find which location failed first, the maximum stress criterion was used at each location and the pressure to which the criterion was reached is reported in Table 7.3. For example, in Figure 7.8 (a), the compression longitudinal stress at location B reached C_{11}=315MPa at 60 kPa.

Table 7.3: Failure pressures based on Maximum stress criteria

Stress concerned and location	Exceeding pressure
Compressive σ_{11} at location B (at junction)	60 kPa
Tensile σ_{11} at location A (in main flange)	>60 kPa
Compressive σ_{22} at location C (in main flange)	58 kPa
Tensile σ_{22} at location D (in web)	**41 kPa**
Shear stress at location E (in main flange)	45 kPa

From Table 7.3, the first stress to exceed its ultimate value was the transverse tensile stress in the web at Location D. When the loading exceeded 41kPa, the panel was predicted to fail from transverse tensile cracks in web at location D along the longitudinal junction, which was consistent with the experimental tearing cracks 1 and 4 in Figure 7.9. The other cracks (cracks 2 and 3 and in the webs) seen in the experimental panel were assumed to be caused by the progressive additional damage of the panel after failure initiation. The numerical failure pressure agreed well with the experimental failure which occurred between 44 kPa and 48 kPa.

These conclusions were based on the maximum stress failure criterion. In order to take into account interaction of the three stresses, the Tsai Hill criterion (Equation 5.6) was automatically computed with the FEM program for every shell elements constituting the panel. Similar results to the maximum stress criterion were obtained: the Tsai Hill failure criterion was reached for the first time at 41kPa in the shell element at Location D.

Figure 7.10 shows the transverse stress waves developed in the web near the main flange junction along the span at 41 kPa. As shown before, the first location to reach failure was location B, point at mid span. The half wave length was 220mm which was close to the length of the cracks of 254 mm measured in the experiments, thus suggesting that in experiments the failure propagated along this half wave.

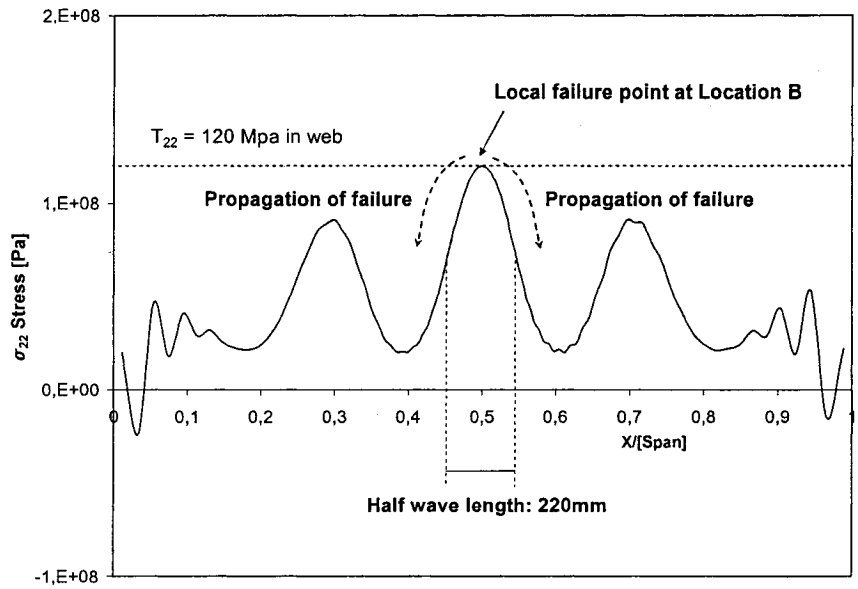

Fig 7.10: σ_{22} stress in web near main flange junction; failure propagation

7.5 Buckling and Failure of the reverse connected panel

So far, the FRP reverse sheet pile panel was studied only in single configuration. This did not represent the field service condition, since the panels are always connected and the two connection pin and eye flanges are therefore restrained. To obtain the buckling and failure loads of connected reverse panels, the boundary conditions shown in Figure 4.8 (perfect pin connection) were enforced on the shell-element model in reverse position. The main change concerned the section boundary conditions: the FEM reverse single panel section had no transverse support (Figure 4.6), whereas the FEM reverse connected section was enforced to remain of equal width throughout the calculations (Figure 4.8). The pre-buckling calculation, bifurcation load calculation and post-buckling calculation using the imperfection method described in Figure 5.2 were applied to this new model.

The buckling extraction procedure showed very similar results for the two configurations. The same buckling mode as in Figure 7.3 was found for the connected configuration, and nearly the same buckling pressure was found: 24 kPa for the connected reverse panel versus 25 kPa for the single configuration (Table 7.1). The two post-buckling deformed meshes in Figure 7.11 were obtained with the single and connected shell-connection models, imperfections were added in the initial geometry in order to obtain those post-buckling deformed shape. It is visible that the lateral restraints on the connected panel permitted to reduce significantly the deflection of the pin and eye flanges.

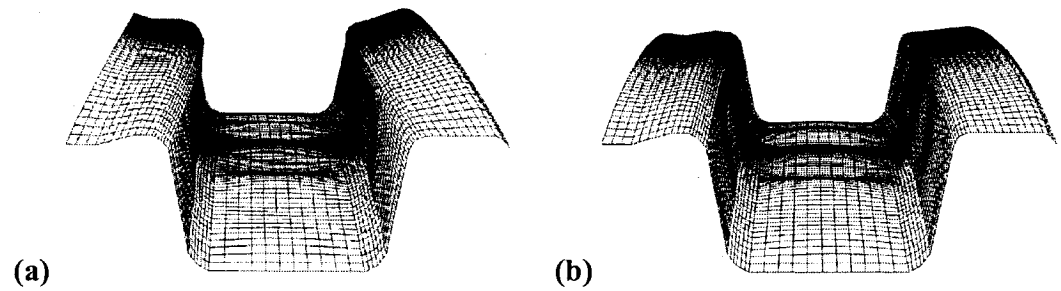

Fig 7.11 Deformed shape of single (a) and connected (b) reverse position panel at 40 kPa

The deflection of the main flange calculated for the two configurations are shown on figure 7.12. Very similar results were found for the two models.

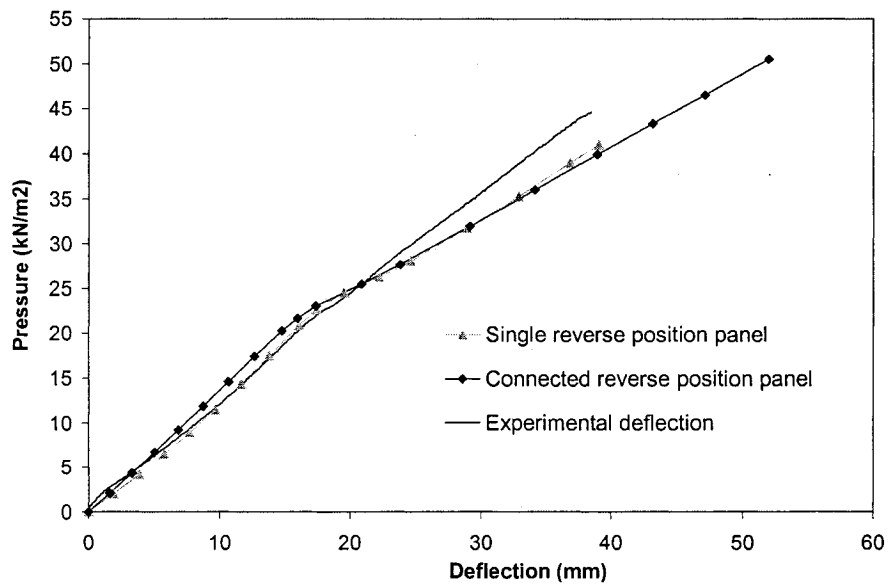

Fig 7.12: Comparative deflections of the single and connected reverse panels

The stresses analysis showed also a very similar distribution to the one in Figure 7.7, and failure of the reverse connected panel was also found at location D (defined in Figure 7.7). Figure 7.13 gives the evolution of the critical transverse tensile stress at location D for the two configurations.

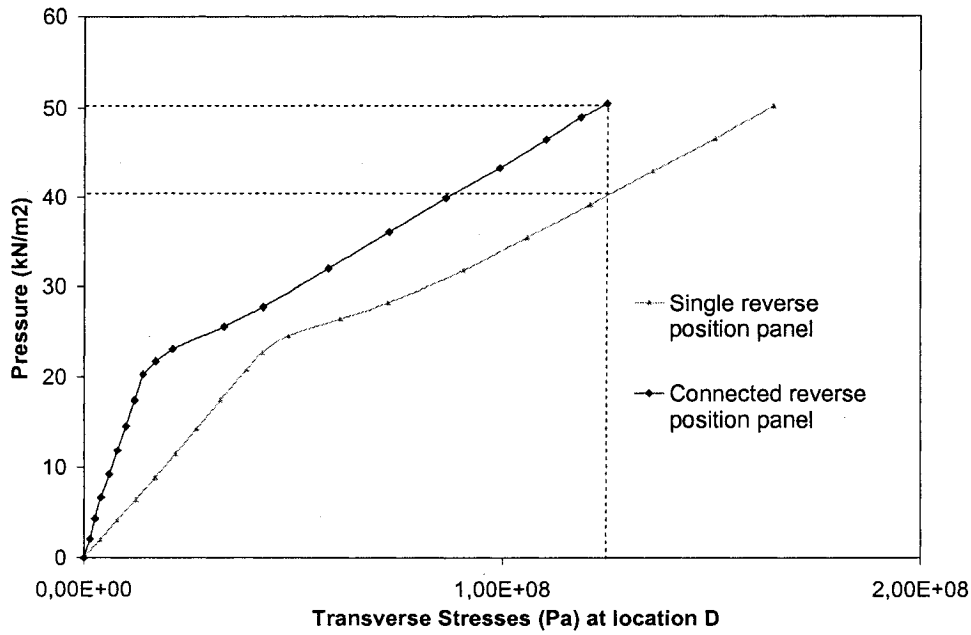

Fig 7.13 Comparative transverse stress at location D (Fig 7.7) of the single and connected reverse panel; comparative failure loads

As shown in Figure 7.13, the connected reverse FRP beam had a higher load capacity than the single panel. The connected reverse position panel failed of compressive junction tearing at 51 kPa, whereas the single panel failed in the same way but at 41 kPa. According to this numerical calculation, the load capacity obtained by using a single panel was 20% less than the capacity of the connected reverse panel in use conditions. Since the two single reverse panel tests yielded the maximum pressures of 44 kPa and 48 kPa, the experimental failure load was overestimated with the connected FEM reverse panel and underestimated with the single FEM reverse panel. This suggested that the effective experimental section boundary conditions were in between those of the FEM single panel (no lateral support of the section, Figure 4.6) and those of the FEM connected panel (full lateral support of the section, Figure 4.8).

Chapter 8: Performance of FRP Sheet Piles Exposed to Harsh Environments

The previous chapters take into account only the dry material properties in an ideal service conditions. This chapter studies the influence of the environmental exposures, such as freezing, freezing/thawing cycles and water immersion, on the buckling and failure loads of the standard position and reverse position sheet piles. The simplified connected model (shell-connection model with translational symmetry boundary conditions, Figure 4.8) was used for the calculation in both loading configurations.

8.1 Effect of the elastic constants variation on the buckling load

The buckling load is a function of the elastic constants and has nothing to do with the ultimate stress values. From the coupon tests shown in Table 3.4, it was seen that the elastic constants were not altered significantly by environmental conditions contrary to the ultimate stresses. Consequently, the buckling load would not change substantially by exposure to moisture and cold temperatures. However, the tests showed variations in a range of possible values for each material constant (E_{11}, E_{22} and G_{12} for each member of the section); the maximum variation was 10%. In order to measure the consequence of such uncertainties on the buckling load, four simulations were carried out to assess the influence:

(1) Worst case: all elastic constants were reduced by 5% and 10%.

(2) Best case: all elastic constants were increased by 5% and 10%.

To obtain the new buckling loads, the calculation procedures, described in Figure 5.2, were repeated with the new elastic properties. The results are displayed in Table 8.1. It is interesting to notice that the change of the buckling load was almost proportional to the change in elastic constants. The variations in material properties should always be considered in the worst case when designing the sheet pile: 10% reduction of all elastic constants would generate about 10% reduction of the buckling load.

Table 8.1: Effects of the elastic constants variation on the buckling pressure

Values variation	Standard position		Reverse Position	
	Buckling Pressure	Difference	Buckling pressure	Difference
+10%	47.5 kPa	+ 9.7%	27.7 kPa	+9.5%
+5%	45.3 kPa	+4.6%	26.6 kPa	+5.2%
Reference	43.3 kPa	0%	25.3 kPa	0%
-5%	40.9 kPa	-5.5%	24.0 kPa	-5.2%
-10%	38.9 kPa	-10.2%	22.8 kPa	-9.9%

8.2 Effect of the environment conditions on the load capacity of the sheet pile

Unlike the buckling load, the ultimate failure load is a function of the environmental conditions because it is closely related to the ultimate stresses. Consequently, the strength loss by environmental conditions reported in Table 3.4 would alter significantly the load capacity of the sheet pile. Section 8.2.1 studies the effect of the environmental conditions on the failure load of the standard position panel and section 8.2.2 studies the failure load of the exposed reverse position panel.

8.2.1 Standard configuration

In order to obtain the new failure loads of the standard position panels exposed to harsh environments, the entire FEM procedure presented in Chapter 6 was repeated for the six environmental conditions considered. Since the elastic constants were not altered significantly by environmental conditions, these constants were not changed as FEM inputs. In order to be able to apply the Maximum stress criterion and the Tsai Hill criterion, all the ultimate stresses (T_{11}, T_{22}, C_{11}, C_{22} and S_{12} for each member) were changed for each case according to Table 3.4 as FEM inputs: each environmental condition corresponded to a complete set of ultimate stresses. As in chapters 6 and 7, the program automatically calculated the criteria reduced stresses of Equations (5.5) and (5.6) in every element of the model (Output CFAILURE). The failure load was defined as the pressure to which the left-hand side of Equations (5.5) or (5.6) exceeded one by any elements in the model.

The results of the six complete simulations corresponding to the six environmental exposures of the standard position sheet piles are displayed in Table 8.2 along with the loss of the load bearing capacity in the different exposures with reference to the dry panel. As expected, because the six environments did not introduce significant stiffness reduction, the buckling load remained same as that of the dry reference sheet pile.

Table 8.2: Effects of the environmental exposures on buckling load and failure load of the standard position panel

Environment condition	Buckling load	Failure load			
		Tsai Hill criterion	Loss	Max Stress Criteria	Loss
Dry, Reference	43 kPa	40 kPa	0%	41 kPa	0%
Dry + Freezing conditions	43 kPa	39 kPa	-3%	40 kPa	-2%
Dry + Freezing/Thawing conditions	43 kPa	37 kPa	-8%	38 kPa	-7%
Saturated condition	43 kPa	34 kPa	-15%	34 kPa	-17%
Saturated + Freezing conditions	43 kPa	32 kPa	-20%	32 kPa	-22%
Saturated +Freezing/Thawing conditions	43 kPa	31 kPa	-23%	31 kPa	-24%

The following conclusions were drawn for the standard position panel at different service conditions:

(1) In each environmental condition, the two criteria predicted very similar failure pressures.

(2) The element leading to the localized failure of the standard position panel, i.e. the first element where the failure criteria reached one, was located in the web near the compressive junction (Location B in Figure 6.20) in the six cases. This corresponded to the location of high transverse compressive stress, therefore indicating that the failure was dominated by transverse compressive failure in web. Furthermore, the percent loss in failure loads was fairly close to the percent loss in transverse compressive strength of the

web material. The compressive strength loss in web was obtained in Figure 3.9; they were, in the same order of environmental conditions, 0%, 3%, 6%, 13%, 19%, and 22%. The similitude confirmed that the failure of the exposed standard position panel was dominated by compressive strength in web. Since failure occurred with the same mode and at the same location, it was possible to present the six failure pressures on the same graph; Figure 8.1 shows the pressure/transverse stress curve at location B and makes the correspondence between the different ultimate compressive stresses in the web and the failure pressures. Because the six environments did not introduce significant stiffness reduction, the same pressure-stress curve was found for the different environments. The buckling pressure is also shown in the graph.

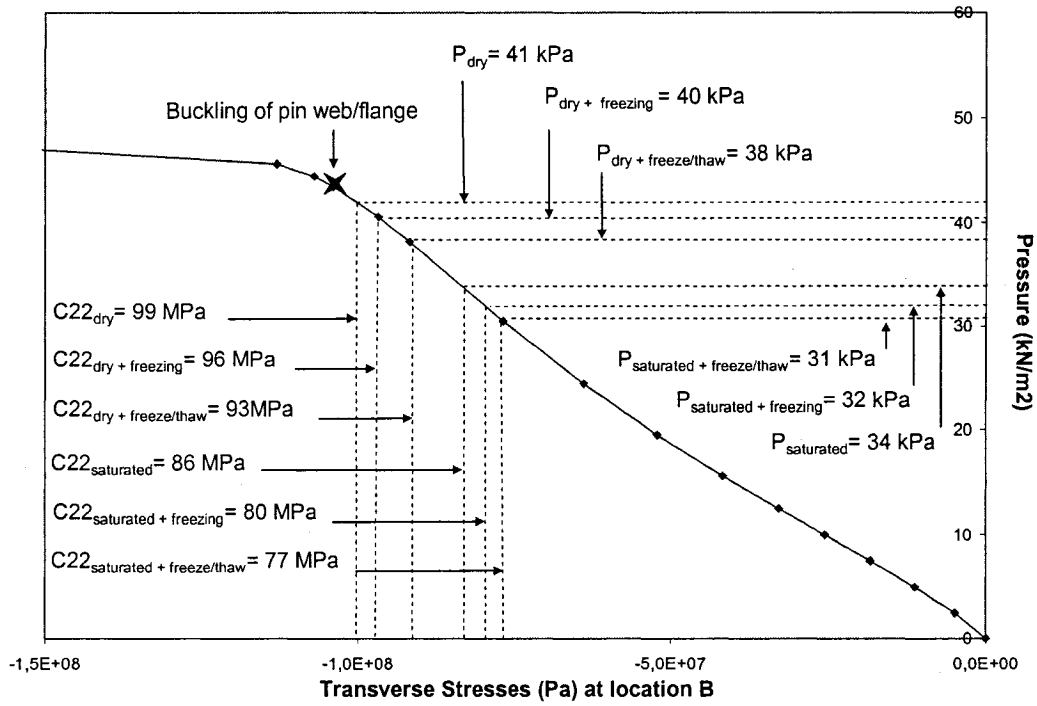

Figure 8.1: Compressive failure at location B of the exposed standard position panels

(3) It was seen that the loss in load capacity of the dry standard position panel was not considerable after freezing and freeze/thaw cycle exposures; the reduction was about 2% to 7%. The capacity loss was nevertheless considerable for the saturated panel: the remaining capacity was 83% after saturation in comparison with dry panel. The worst case was observed to be water saturation combined with freeze/thaw cycle conditions; the remaining load capacity was 76%.

(4) The environmental conditions changed the failure mode of the standard position sheet pile. As seen in Chapter 6, the failure pressure of the reference dry panel was found close to the buckling pressure with less than 5% difference, therefore suggesting that buckling and failure would occur simultaneously. Concerning the saturated panel exposed to freeze/thaw cycles, the failure load was 31 kPa which was about 28% less than the buckling load. This implied that the saturated freeze/thaw panel would never buckle; instead, it would fail in compressive crushing in transverse direction of web and no buckling wave would be visible as for the reference dry panel (Figures 6.22 to 6.24).

8.2.2 Reverse configuration

Similar FEM analysis as the one presented in Chapter 7 was repeated on the reverse position panel for the six environmental conditions considered. As assumed before, the elastic constants were not changed in the inputs, which resulted in a constant buckling load. The ultimate stresses were changed according to Table 3.4. Table 8.3 summarizes the results of the reverse position panel exposed to harsh environments.

Table 8.3: Effects of the environmental exposures on buckling load and failure load of the reverse position panel

Environment condition	Buckling load	Failure load			
		Tsai Hill criterion	Loss	Max Stress Criteria	Loss
Dry, Reference	24 kPa	51 kPa	0%	51 kPa	0%
Dry + Freezing conditions	24 kPa	51 kPa	0%	51 kPa	0%
Dry + Freezing/Thawing conditions	24 kPa	50 kPa	-2%	50 kPa	-2%
Saturated condition	24 kPa	44 kPa	-14%	44 kPa	-14%
Saturated + Freezing conditions	24 kPa	42 kPa	-18%	42 kPa	-18%
Saturated +Freezing/Thawing conditions	24 kPa	40 kPa	-22%	40 kPa	-22%

Parallel conclusions to the standard position panel were made:

(1) In each environmental condition, the two criteria predicted very similar failure pressures.

(2) The element leading to the localized failure of the reverse position panel was located in the web near the main flange junction (Location D in Figure 7.7) in the six cases. This corresponded to the location of high transverse tensile stress (T_{22}), therefore indicating that the failure was dominated by transverse tensile stress in web. The percent loss in failure loads was fairly close to the percent loss in transverse tensile strength of the web material. In the same order of environment conditions, the loss of transverse tensile stress in web (T_{22}) was found in Figure 3.8 to be 0%, 0%, 3%, 15%, 24%, and 29%. The similitude confirmed that the failure of the exposed reverse position panel was dominated by transverse strength T_{22}. Since the failure was always of the same mode and at the same location, the six failure pressures could also be determined from the pressure against transverse stress curve at location D in Figure 8.2. The correspondence between the different ultimate tensile ultimate stresses and failure pressures are highlighted.

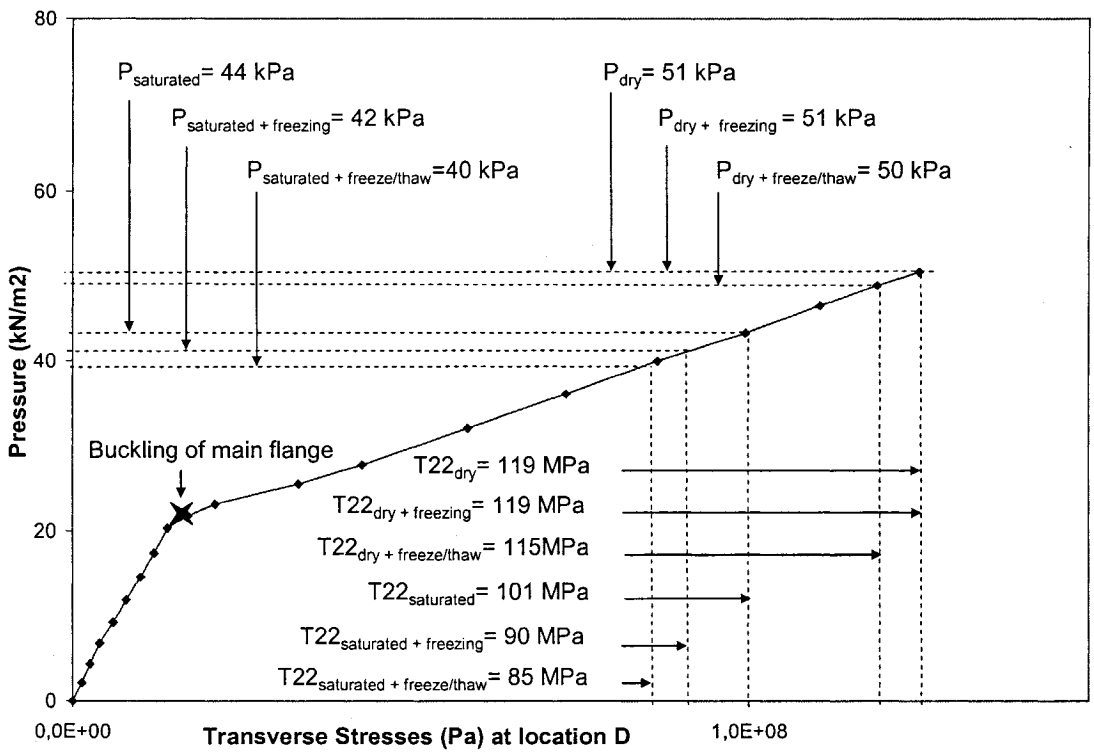

Figure 8.2: Tensile failure at location D of the exposed reverse position panels

(3) The dry reverse panel was not sensible to freezing or freezing/thawing conditions: the failure load remained almost the same. When the composite was saturated with water, the load bearing capacity was reduced by 14%. This loss in the load bearing capacity of the saturated panel was greater when exposed to subsequent freezing or freezing/thawing cycles: the loss was 18% and 22% respectively.

(4) Failure of the exposed reverse position panel always occurred after buckling of the main flange since all failure pressures were much greater than the buckling pressure.

8.2.3 General discussion

(1) The losses in load bearing capacity of the FRP sheet pile panels in the two installation positions analyzed by the two criteria were in the same order of magnitude.

(2) The reduction in load capacity of sheet pile panels exposed to harsh environments was dominated by the transverse compressive strength, C_{22}, in web in standard position, and by the transverse tensile strength, T_{22}, in web in reverse position.

(3) The dry panel in reverse or standard position was proven to be resistant to freezing and freezing/thawing cyclic temperature. The maximum capacity loss was only 2% in the reverse position panel and 7% in the standard position panel.

(4) Most of the damage was done by water absorption. After saturation, an average of 85% of the initial strength remained in both configurations.

(5) Freezing conditions and Freeze/Thaw cycles worsened the damage done by the water uptake: the remaining capacity was only 76% to 82% of initial strength after cold temperature exposure.

(6) It is difficult to perform full-scale panel tests to examine the effects of freezing and freezing/thawing on saturated sheet piles. Numerical simulation provided a powerful tool to complete the analysis and estimate the reduction in capacity due to the exposures.

Chapter 9: Modification of the Sheet Pile Profile Design

Chapters 6 and 7 explained in detail the mechanical behaviour of composite sheet pile panel loaded in its two installation configurations using finite element simulation. It was shown that the profile had limited load capacity. This chapter is to explore the possibility of finding ways to modify the design and improve the performance. The challenge was not to "revolutionise" the entire design but to incorporate small changes which would improve the performance. Therefore the same general geometry was used and only the thicknesses of the different members were modified.

9.1 Summary on the FRP Sheet Pile study

9.1.1 Standard configuration

From the ultimate limit state point of view, the standard configuration panel was predicted to fail at the web near the compressive junction at 41 kPa (Maximum stress criterion). In Chapter 6, buckling initiation of the compressive plates and local failure of the composite were found to occur simultaneously. Consequently, in order to increase the load bearing capacity of the standard position FRP sheet pile, it would be necessary to find design changes to increase the buckling pressure and to strengthen the transverse direction in the webs. From the serviceability limit state point of view, the pressure-deflection curves (Figures 6.2 and 6.5) of the standard position panel exhibited significant softening behaviour. Preventing the reduction of the flexural rigidity would certainly permit the standard position panel to have better resistance to deflection.

The following options provide means to modify the profile design:

(1) The first solution considered is to change entirely the geometry. Using a closed section (for example the box-section design) will prevent the section from opening. Because it is considered as a "revolutionary solution", this option will not used in the following calculation.

(2) The second solution considered is to increase the orthotropic coefficient of the section (E_{22}/E_{11}) to approach the homogenous plate. Strengthening the transverse direction will permit the webs to take more loads. However, for a given thickness, increasing E_{22} would mean increasing the thickness of the transverse fibre layers at the expense of the longitudinal roving layer. Consequently, the flexural rigidity would be reduced leading to an increased deflection, therefore this solution is not considered.

(3) The third solution is to increase the thickness of the compressive junctions. This option would permit the enhancement of the restraints between the compressive flanges and the compressive webs, thus increasing the buckling load of the FRP panel and preventing excessive rotation of the eye/pin flanges.

(4) The fourth solution is to increase the thickness of the compressive plates (eye/pin flanges and webs) in order to enhance their geometric coefficients (thickness over width), and thus the bifurcation load of the buckling plates. Increasing the thickness of the web will also permit to increase the transverse capacity of the web.

For the modification of the FRP panel in standard position, only approaches (3) and (4) are employed in the following calculations

9.1.2 Reverse configuration

Numerical results of chapters 6 and 7 indicated that the failure load of the reverse position panel was about 25% higher and the deflection 14% less at 40 kPa in comparison with the standard position panel. These figures suggested that, despite the fact the reverse position panel buckled at lower applied load than the standard position panel, the reverse position panel might have the potential to carry more ultimate loads with less deflection.

The deflections, the longitudinal strains and the longitudinal stresses in the reverse position panel were found quite different from the standard position panel. They exhibited hardening behaviour before buckling of the main flange. The non-linear deformation of the reverse position panel which led to stiffness increase was seen as an advantage for the performance of the reverse position panel. However, after buckling initiation, the

hardening behaviour in the main flange was significantly reduced, leading to an increased deflection (Figure 7.12).

Contrary to the standard configuration, the buckling load of the reverse position panel was low (almost twice as low as the standard position). Although the panel could perform satisfactory after this bifurcation load due to its post buckling behaviour, this buckling shape was unwanted: if the buckling load was taken as the design load (taking therefore minimum risks), then the reverse configuration would perform poorly compared to the standard position. The very low buckling load of the reverse position panel was possibly attributed to the following two factors:

(1) It was seen in Figures 6.16, 6.17 and 7.5, that the distributions of stresses in the compressive plates in the two positions were quite different. For the standard position, stress distributions in compressive flanges were found to be linear along the width of the buckling plates, whereas longitudinal compressive stresses were uniformly distributed in the main flange in the reverse position. For comparison, the buckling load of a steel plate with linearly distributed load is almost twice as large as if it is uniformly distributed (for the same average longitudinal stress). It was expected that the composite would behave in the same way.

(2) Because the main flange was thicker than the other two adjacent web plates, the restraint stiffness of the reverse position section on the compressive main flange was smaller than the restraint stiffness of the standard position section on the compressive eye/pin flanges.

In order to increase the performance of the reverse position panel, the problem of the buckling load should be tackled. So as to take full advantage of the stiffness increase of the section due to the non-linear deformation of the section, the buckling load should be increased. The solutions (3) and (4) (respectively increasing the thickness of the compressive junctions and of the main flange) are to be considered.

9.2 Proposition of High performance panels

Using all the previous observations and conclusions, calculations were performed on modified FRP profiles. This section presents the modified profiles and reports the results of the calculations.

9.2.1 Geometry of the proposed panels

Modifications were proposed for both standard position panel and reverse position panel. Two design strategies, according to solutions (3) and (4), were considered:

(1) Strategy 1: the improvement involved the material addition as stiffeners at the compressive junctions to enhance the restraints on the compressive plates.

(2) Strategy 2: the improvement involved the increase in thickness of all compressive plates to have better buckling resistance.

In order to be able to compare the efficiency of the two strategies, the same amount of material was added to the original profile with an increase of 10% of total area. In total, four different panels were proposed corresponding to two panel categories in two strategies. Figure 9.1 presents the original panel section and the four new profiles. The characteristic of the section is given in the right column; the bold characters are the design modifications. In the left column is the AutoCAD drawing of the section.

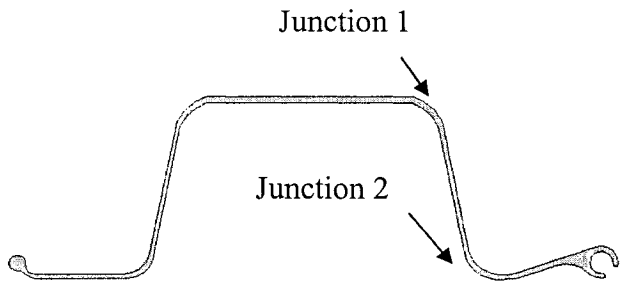

Area: 24.4cm^2
Thickness of main flange: 4.69 mm
Thickness of web: 3.17 mm
Thickness of eye/pin flanges: 3.18 mm
Thickness of junctions 1: 4.00 mm
Thickness of junctions 2: 3.30 mm

Profile A: Original design

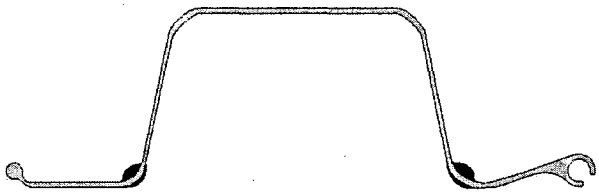

Area: 26.8cm^2 (+10%)
Thickness of main flange: 4.69 mm
Thickness of web: 3.17 mm
Thickness of eye/pin flanges: 3.18 mm
Thickness of junctions 1: 4.00 mm
Thickness of junctions 2: **15.0 mm**

Profile B: Standard design with junction stiffeners

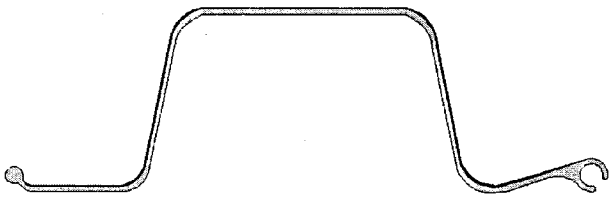

Area: 26.8cm^2 (+10%)
Thickness of main flange: 4.69 mm
Thickness of web: **3.90 mm**
Thickness of eye/pin flanges: **3.90 mm**
Thickness of junctions 1: 4.00 mm
Thickness of junctions 2: **4.00 mm**

Profile C: Standard design with increased compressive plate thickness

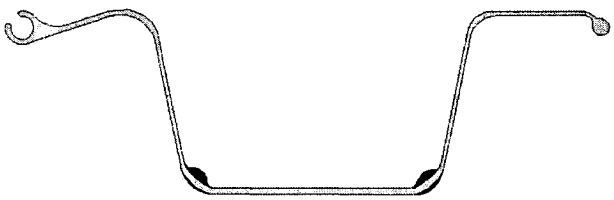

Area: 26.8cm^2 (+10%)
Thickness of main flange: 4.69 mm
Thickness of web: 3.17 mm
Thickness of eye/pin flanges: 3.18 mm
Thickness of junctions 1: **15.00 mm**
Thickness of junctions 2: 3.30 mm

Profile D: Reverse design with junction stiffeners

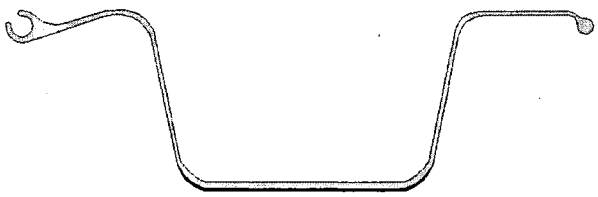

Area: 26.8cm^2 (+10%)
Thickness of main flange: **6.20 mm**
Thickness of web: 3.17 mm
Thickness of eye/pin flanges: 3.18 mm
Thickness of junctions 1: **4.70 mm**
Thickness of junctions 2: 3.30 mm

Profile E: Reverse design with increased compressive plate thickness

Figure 9.1: AutoCAD drawings of the proposed improvement in sheet pile profiles

9.2.2 Calculation performed on the high performance panels

The performances of the five different profiles presented in Figure 9.1 were calculated with the FEM program. The simplified shell-connection model was used. In order to study the pre-buckling, buckling and post-buckling behaviours, the calculations presented in Chapter 5 were repeated. To obtain the failure load, the Maximum Stress Criterion was used. In Chapter 6 and 7, it was found that the maximum stress criterion gave the same results as the Tsai-Hill criterion. The stress criterion was automatically applied with the FEM program.

The complete results of the simulations are summarized in Tables 9.1 to 9.4. Results of profiles A, B and C in standard configuration are discussed in Section 9.2.3 and results of profiles A, D and E in reverse configuration are discussed in Section 9.2.4. Two design considerations are used to compare the panels.

(1) The Ultimate Limit State is shown in Table 9.1 for the standard position and in Table 9.3 for the reverse position. The Tables show the buckling load, the failure load along with the failure description.

(2) The Serviceability Limit State is shown in Table 9.2 for the standard position and in Table 9.4 for the reverse position. The Tables show the deflection at 10 kPa and at 40 kPa along with the deflection at failure.

9.2.3 Results of the improved profiles in standard installation

Table 9.1: Ultimate limit state for improved panels in standard installation

Profile	Buckling load		Failure load		Failure description
(A) original panel	43 kPa	0%	41 kPa	**0%**	Transverse compressive failure in the web
(B) standard design with stiffeners	93 kPa	+116%	44 kPa	**+7%**	Transverse compressive failure in the web
(C) standard design with increased thickness	66 kPa	+53%	44 kPa	**+7%**	Transverse compressive failure in the web

For the standard design panels, identified as profiles B and C, in standard installation, the two strategies, stiffeners and increased thickness of the compression plates, were found efficient to increase the buckling load. It was possible to increase the buckling load by 116% by adding only 10% of composite at the two compressive junctions. When the same amount of material was added throughout the compressive plates, the increase was of 53% as seen in Table 9.1. However, the substantial increase in the buckling load did not lead to a significant increase of the failure load. Obtaining such high buckling loads was not beneficial since the panel failed during the pre-buckling stage at a pressure of 44 kPa due to transverse crushing in the web near the compressive junctions. This corresponded to an improvement by only 7% compared to the original panel. The low compressive strength of the web composite in the transverse direction did not permit to improve significantly the load-carrying capacity of the standard position panel.

Table 9.2: Serviceability limit state for improved panels in standard loading

Profile	Deflection at 10kPa		Deflection at 40kPa		Deflection at failure
(A) original panel	8.8 mm	0%	44.2 mm	**0%**	44.2 mm
(B) standard design with stiffeners	7.2 mm	-18%	31.4 mm	**-29%**	34.8 mm
(C) standard design with increased thickness	7.2 mm	-18%	35.3 mm	**-20%**	39.6 mm

As regarding the deflections in Table 9.2, the improvements in serviceability of profiles B and C showed far better than in the failure load. Additional material had two effects: increasing the initial flexural rigidity and reducing the non-linear deformation of the section. At 10 kPa, both strategies led to 18% reduction of the deflection. No further improvement was observed for profile C since about the same reduction was found at 40 kPa. For profile B, the reduction increased to 29% at 40 kPa, thus suggesting that introducing stiffeners in the compressive junctions was more efficient to reduce the non-linear deflection. In Chapter 6, it was seen that the softening behaviour was caused by the relative upward deflection of the pin/eye flanges about the junctions. The stiff junctions in profile B reduced significantly this movement.

9.2.4 Results of the improved profiles in reverse installation

Table 9.3: Ultimate limit state for improved panels in reverse loading

Profile	Buckling load		Failure load		Failure description
(A) original panel	24 kPa	0%	51 kPa	**0%**	Transverse tensile tearing failure in the web
(D) reverse design with stiffeners	110 kPa	+358%	78 kPa	**+53%**	Transverse compressive failure in the main flange
(E) reverse design with increased thickness	48 kPa	+100%	62 kPa	**+22%**	Transverse compressive failure in the main flange

For the reverse design panels, profiles D and E, in reverse installation, increasing the restraints of the buckling plate with the stiffeners strategy seemed to be more efficient than increasing the entire thickness of the compressive plates in order to enhance the buckling load. In Table 9.3, the buckling load of profile D was increased by 358%, whereas the buckling load of profile E was enhanced by 100%. Unlike the standard design panels in standard installation, the increase in the buckling load was associated with a significant increase in the failure load in reverse panels with modification. Profile E buckled at 48 kPa and failed at 62 kPa. The results of profile D were even better thanks to a higher buckling load: it failed before buckling at a pressure of 78 kPa (+53% with reference to the original profile). For those two profiles, the failure mode was changed: whereas failure occurred in tension at location D (web near junction with main flange, see exact location in Figure 7.7) for profile A, failures of profiles D and E occurred at location C (center of main flange) in the transverse direction and in compression.

Tab 9.4: Serviceability limit state for improved panels in reverse loading

Profile	Deflection at 10kPa		Deflection at 40kPa		Deflection at failure
(A) original panel	7.1 mm	0%	38.0 mm	**0%**	52.0 mm
(D) reverse design with stiffeners	6.2 mm	-13%	23.0 mm	**-40%**	48.3 mm
(E) reverse design with increased thickness	6.0 mm	-15%	22.5 mm	**-41%**	45.4 mm

The results of serviceability limit state are given in Table 9.4 for profiles D and E. In both cases, the deflection at 10 kPa was reduced by about 15%, which was attributed to the area increase of 10%. At 40 kPa, the deflection was further reduced by about 40%. The increase in the buckling load permitted to take full advantage of the non-linear hardening behaviour of the section caused by stiffness increase; this was not the case with the original profile design where the increase in section stiffness was set off by the reduced buckling load.

9.2.5 Summary

To compare the standard installation with reverse installation, failure pressures of the two installations are presented in Figure 9.2 and the maximum deflections at 40 kPa in Figure 9.3. Only the profiles with stiffeners are displayed for they showed better results than the strategy with increased thickness of the compressive plate.

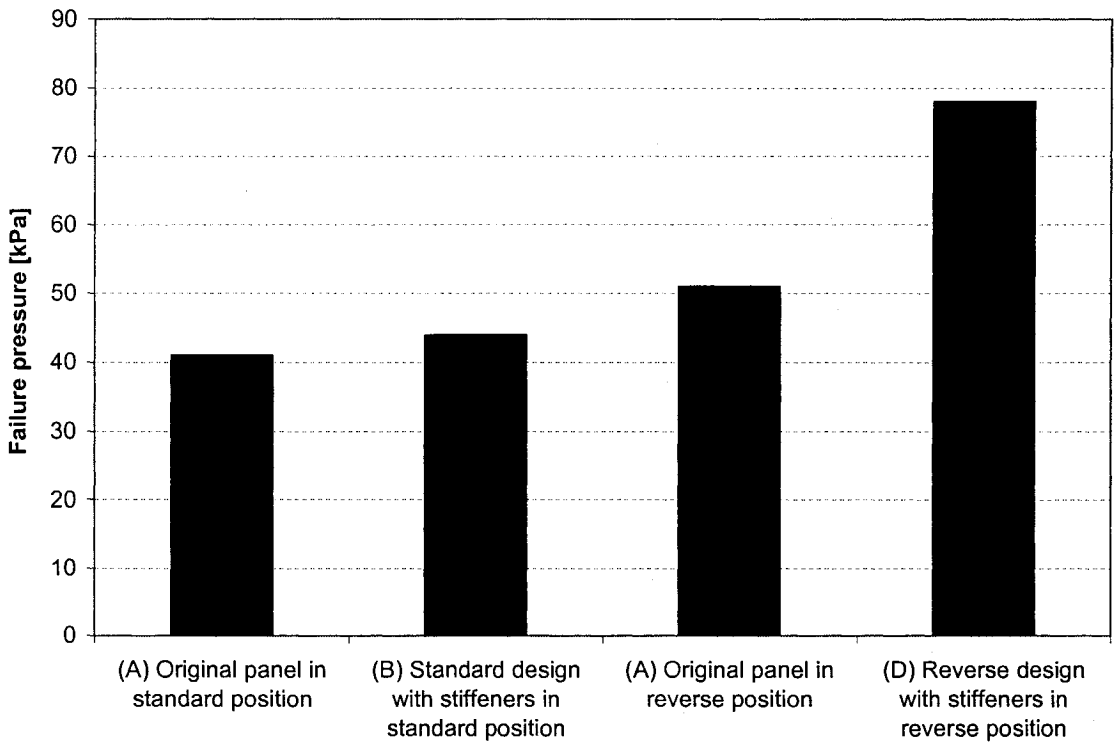

Figure 9.2: Ultimate limit state performance of the improved sheet piles

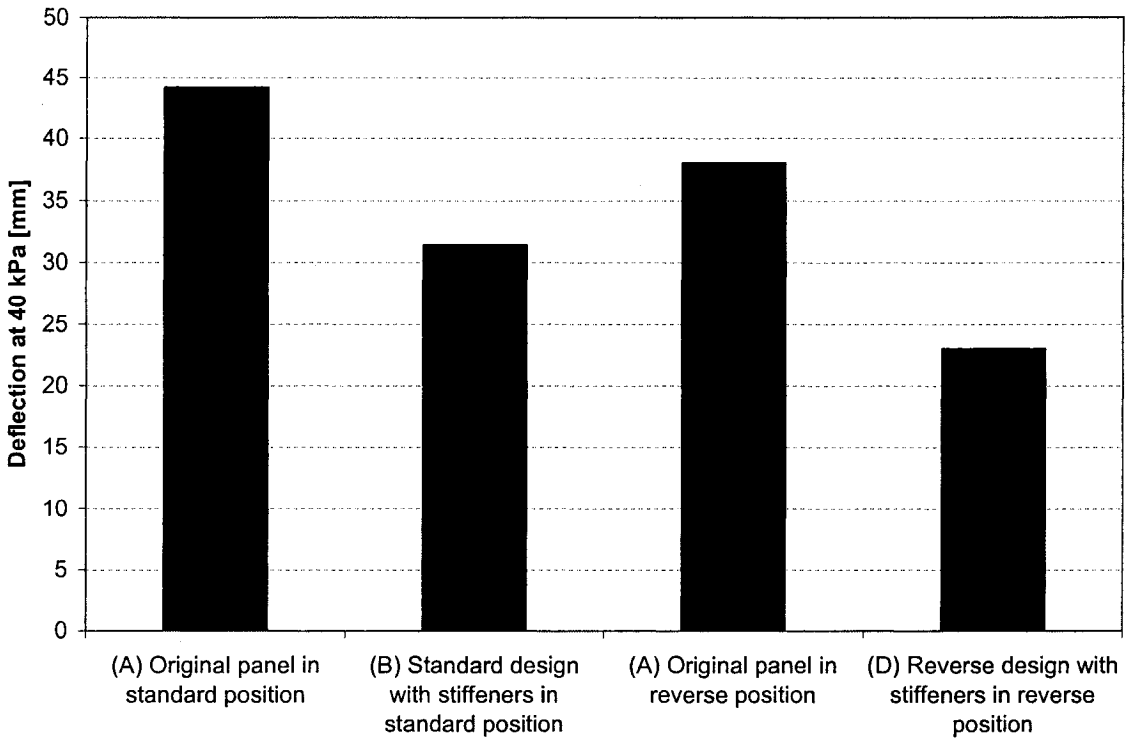

Figure 9.3: Serviceability limit state performance of the improved sheet piles

In Figure 9.2 and 9.3, the stiffened profile was found to have the potential to perform better in reverse than in standard position:

- Profile B failed at 44 kPa and presented a deflection of 31.4 mm at 40 kPa.
- Profile D failed at 79 kPa, an 80% increase compared to profile B, and presented a deflection of 23 mm at 40kPa, a reduction of 26% compared to profile B.

Consequently, as soon as the buckling problem was solved via stiffeners in the compressive junctions, the sheet pile is more efficient to be installed in reverse position. In this reverse configuration with two stiffeners at compressive junctions, the pin in eye connection is on tension side. This stiffened reverse position panel takes full advantage of the stiffness increase.

Chapter 10: Conclusions and Future Work

To understand the structural behaviour of pultruded sheet pile panels and to assist design with efficiency, this research was aimed in two directions:

(1) To obtain the mechanical properties of a pultruded FRP composite in longitudinal and transverse directions at six environmental exposures.

(2) To develop a numerical model using finite element program Abaqus/Standard to analyze the pre-buckling, buckling initiation and post-buckling behaviour of a composite sheet pile in order to examine the load capacity, deformation and failure mechanism of the panel. Environmental effects were simulated with the help of the materials tested at different exposure conditions.

10.1 Conclusions

(1) Effects of five different environmental conditions on the composite material properties were studied with coupon tests: freezing conditions, freezing/thawing conditions, wet environment, wet and freezing conditions and wet and freezing/thawing conditions. It was found that negligible stiffness reduction was not significant after the environmental exposures, but the strength losses were considerable. Most of the damage was done by water absorption: strength of saturated composite decreased to an average of 87% in transverse direction and 81% in longitudinal direction. Freezing conditions and freeze/thaw cycles worsened the damage done by the water uptake; the average remaining strength was 76% of initial capacity after freeze/thaw cycles of saturated material in both directions. On the other hand, dry composites demonstrated excellent resistances to freezing and freeze/thaw cycles.

(2) A finite element analysis was applied to a sheet pile wall subjected to uniform pressure to assess its moment capacity in two installation configurations. As regard to the standard connected position panel, it was found that buckling initiation and ultimate failure happened almost simultaneously at 41 kPa. The pressure-deflection was found to exhibit a significant softening behaviour due to the reduction of the section stiffness. In

the case of the reverse connected configuration, buckling occurred at 25 kPa which led to a post-buckling load bearing capacity of 51 kPa. Contrary to the standard position panel, the reverse deflection exhibited hardening behaviour due to increase of the section stiffness. Comparative results showed that the reverse position panel had the potential to carry more ultimate load with less deflection.

(3) Durability properties of sheet pile in service conditions were studied using reduced material properties to assess the effect of environmental exposures on the sheet pile with the FEM program. Since the five environmental conditions did not introduce significant stiffness reduction, the buckling behaviours of the exposed sheet piles were nearly identical to the reference dry no-exposure condition. The worst capacity reduction occurred to the saturated sheet pile with freeze/thaw exposure; the average ultimate pressure reduction was estimated to be about 23% for the two loading installations. The environment conditions could change the failure mode of the sheet pile. Whereas the dry standard position panel failed due to buckling initiation, the saturated and freeze/thaw exposed panel failed in direct stress failure. As regard to the reverse position panel, failure always happened in the post-buckling range.

(4) In order to increase the load bearing capacity and decrease the deflection of the original panel, stiffeners were added in the compressive junctions. For the standard position panel, it was found difficult to increase significantly the load bearing capacity of the panel, but considerable improvements were achieved in the resistance to deflection: the new "high performance" standard design profile deflected 29% less at 40kPa than the original profile. For the reverse position, the new "high performance" profile was able to bear 53% more load thanks to an enhanced buckling load and deflected 40% less than the original profile, whereas only 10% of material was added as stiffeners. Similar design approach could be applied to other types of FRP profiles. Box, I-, C-, T-, Z-, and L-sections would certainly perform better with similar stiffeners at the junctions.

10.2 Future work

Future work should be directed in two different directions:

(1) Experiments should be carried out on profiles with stiffeners in order to validate the FEM results. Confirming that introduction of stiffeners in compressive junctions would enhance significantly the buckling load could lead to generalized use of such design for FRP structural members.

(2) Most of the FEM calculation done in this thesis was carried out by replacing the ball in socket connection with a perfect pin connection. However, this assumption was found not exactly true when studying the connected standard position panel with the complete ball in socket connection: from a certain value of the relative rotation of the two ends, the rotation was found not entirely free. A 2D FEM model of the ball in socket connection should be developed to calculate the complete moment-rotation curve up to failure of the connection. By adding this non-linear moment-rotation curve to the previous FEM model instead of the perfect pin connection, the accuracy of the model would be improved. This correction was found unnecessary for the original profile, for the behaviour was already described with efficiency, however it could be critical in the case of the high performance profiles where high values of pressure were reached and where the 3D connections could fail before the buckling of the plate section. This 2D model would also permit to improve the current design of the ball in socket connection.

References

ASTM D695-96. "Standard test method for compressive properties of rigid plastics". American Society of Testing Materials.

ASTM D3039/D3039M-95a. "Standard test method for tensile properties of polymer matrix composite materials". American Society of Testing Materials.

ASTM D3518/D3518M-94. "Standard test method for in-plane shear response of polymer matrix composite materials by tensile test of ±45° laminate". American Society of Testing Materials.

Bank, L. C. and Yin, J. (1999). "Failure of Web-Flange Junction in Postbuckled pultruded I-Beams". *Journal of composites for construction*, 3(4).

Bank, L. C., Yin, J. and Nadipelli, M. (1995). "Local buckling of pultruded beams – nonlinearity, anisotropy and inhomogeneity". *Construction and Building Materials*, 9(6), pp. 325-331.

Barbero, E. J. and DeVivo, L. (1999). "Beam-Column Design Equations for Wide-Flange Pultruded Structural Shapes". *Journal of composites for construction*, (3)4.

Brooks, R. J. and Turvey, G. J. (1995). "Lateral Buckling of Pultruded GRP I-section Cantilevers". *Composite Structures*, 32, pp. 203-215.

Gellert, E. P. and Turley, D. M. (1999). "Seawater immersion ageing of glass-fiber reinforced polymer laminates for marine applications". *Composites*, 30, pp. 1259-1265.

Giroux, C. (2000). "Analysis of the Flexure Behaviour of A Fibreglass Composite" Seawall. M.Eng Thesis, Department of Civil Engineering and Applied Mechanics, McGill University, Montréal, Canada.

Haj-Ali RM, Kilic H. (2002). "Nonlinear behaviour of pultruded FRP composites". *Composites: Part B*, 33, pp. 173-191.

Karbhari, V. M. (2002). "Response of Fiber Reinforced Polymer Confined Concrete exposed to Freeze and Freeze-Thaw Regimes". *Journal of Composites for Construction* 6(1), pp 35-40.

Micelli, F. and Nanni, A. (2004). "Durability of FRP rods for concrete structures". *Construction and Building Materials*, 18, pp. 491-503.

Pecce, M. and Cosenza, E. (2000). "Local Buckling curves for the design of FRP profiles". *Thin Walled Structures*, 37, pp.207-222.

Qiao, P. and Shan, L. (2004). "Explicit Local Buckling Analysis and Design of Fibre-reinforced Plastic Composite Structural Shapes". *Composite Structures*, 70, pp. 468-483.

Qiao, P. and Shan, L. (2004). "Flexural-torsional buckling of fibre-reinforced plastic composite open channel beams". *Composite Structures*, 68, pp. 211-224.

Shanmugam, J. (2004). "Moment Capacity and Deflection Behaviour of Pultruded FRP Composite Sheet Piles". M.Eng, Department of Civil Engineering and Applied Mechanics, McGill University, Montréal, Canada.

Shao, Y. and Kouadio, S. (2002). "Durability of Fibreglass Composite Sheet Piles in Water". Journal of Composites for Construction, 6(4), pp. 280-287.

Wang, Z. and Zureick, A. (1994). "Characterization of the longitudinal tensile behaviour of pultruded I-shape structural members using coupon specimens". *Composite Structures*, 29(4), pp. 463-472.